Sandia
National
Laboratories

SAND 89-7028

DESIGN AND DEMONSTRATION OF AN IMPROVED STRETCHED-MEMBRANE HELIOSTAT

Issued by Sandia National Laboratories, operated for the United States Department of Energy by Sandia Corporation.

Available to DOE and DOE contractors from
Office of Scientific and Technical Information
PO Box 62
Oak Ridge, TN 37831

Prices available from (615) 576-8401, FTS 626-8401

Available to the public from
National Technical Information Service
US Department of Commerce
5285 Port Royal Rd
Springfield, VA 22161

NTIS price codes
Printed copy: A06
Microfiche copy: A01

Cover design: Gene Clardy, Sandia National Laboratories

Cover photo: Daniel J. Alpert, Sandia National Laboratories

Distribution
Category UC-235

SAND89-7028
Unlimited Release
Printed December 1989

DESIGN AND DEMONSTRATION OF AN IMPROVED STRETCHED-MEMBRANE HELIOSTAT

Solar Kinetics, Inc.
10635 King William Drive
Dallas, Texas

Sandia Contract #33-1227

ABSTRACT

Improvements to a stretched-membrane heliostat have been designed and implemented under contract with Sandia National Laboratories. Specific improvements were made to the mirror module to improve performance and reduce costs. The performance of the heliostat in windy conditions was improved by adding a restraint to the rear membrane. An open-section ring was used to increase structural efficiency. The rear structure was redesigned to take advantage of common manufacturing techniques and lower cost materials. The control system was improved, and a means of achieving passive defocus was achieved. Finally, membrane preload was applied with nonconsumable tooling. An 8% reduction in mirror-module cost was realized. The improved design was successfully demonstrated with a 50-m^2 prototype. This prototype had improved optical stability in fluctuating winds. Its slope error in calm winds was measured to be 1.3 mrad.

CONTENTS

 vi Blank

List of Figures

List of Tables

1.0 Introduction

The stretched-membrane mirror module makes efficient use of material to provide an accurate optical platform for a heliostat in response to a variable wind load environment. The heliostat departs from conventional glass-mirror designs by providing stiffness through preload and tension of coupled elements rather than with flexural rigidity. The mirror module is defined by two thin membranes stretched over a circular ring frame. These membranes and ring form a plenum that is evacuated to provide a concave, focused optical surface. Conversely, the plenum can be pressurized to defocus the heliostat.

The feasibility and cost of the stretched-membrane design was investigated and successfully demonstrated with a 50-square-meter prototype installed in 1986 at the Central Receiver Test Facility (CRTF) of Sandia National Laboratories in Albuquerque. The initial design and fabrication effort was used to establish a baseline for further improvements in the mirror-module design. This development relied heavily on the analysis and results presented in the final report for the Mark I stretched-membrane mirror module [1]. The development presented in this report represents only the changes and improvements made to the design, combined with the experience gained from the fabrication of a second prototype.

Design improvements were selected that offered the greatest potential impact on the performance and cost of the Mark I design. These changes in the commercial design are presented in five major sections.

2.0 REAR MEMBRANE RESTRAINT. The rear membrane of the heliostat was attached to the support structure at the center. This restraint reduced normal and radial loads on the ring frame. The attachment also improved dynamic accuracy by reducing the amplitude of and response time to transient errors caused by wind.

3.0 DESIGN OF THE OPEN SECTION RING-FRAME. A double-membrane mirror module eliminates torsional load on the ring. The cross-sectional area of the frame was designed based upon compressive load; the area was distributed to achieve the lowest practical error within stability limits.

4.0 MIRROR-MODULE SUPPORT SYSTEM. The hub and trussed support was designed to respond to wind load distributions developed in wind tunnel testing. The conventional support structure made use of common materials and manufacturing processes to reduce direct and indirect costs.

5.0 CONTROL SYSTEM MODIFICATIONS. The fan was moved to the front of the heliostat and the membrane position sensor was moved to the center to reduce the transient and static error in the heliostat. The ability to defocus on power loss was also provided.

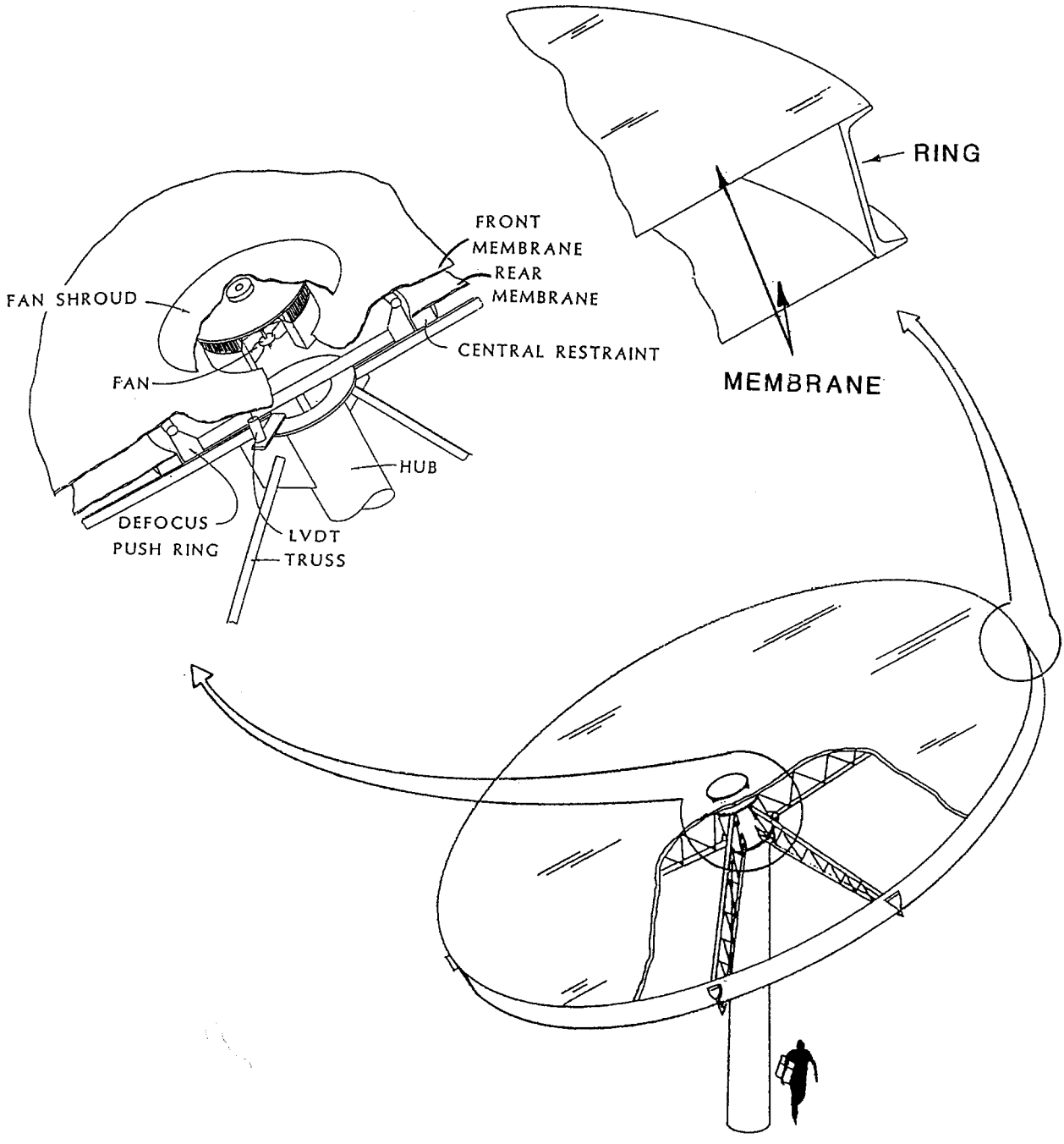

Figure 1.1 Schematic Representation of the Improved Stretched-Membrane Heliostat.

6.0 MEMBRANE ATTACHMENT AND PRELOAD. The initial tension for the Mark II heliostat was applied by tooling during assembly. The inflated tubes and mechanical crimps used in the Mark I ring frame were eliminated in the design improvement.

Figure 1.1 illustrates the improvements made in the mirror module. The reduction in cost associated with these improvements is presented in Section 7.0.

The changes in design proposed for the commercial scale heliostat were subsequently implemented in a prototype mirror module. The module was fabricated and installed at the CRTF for testing. The experience gained during fabrication and preliminary test results are introduced in Section 8.0 of this report, and presented in three major sections.

9.0 INITIAL TESTING. Material processing associated with base membrane stock flatness was investigated along with the quality control procedures required for resistance welding. Initial failures in the tooling, along with solutions for the tooling design, are reported.

10.0 PROTOTYPE FABRICATION. Component manufacturing and site assembly procedures are described.

11.0 TEST AND EVALUATION. The beam quality, dynamic response, and focus control of the prototype are described based upon preliminary testing of the prototype mirror module at the CRTF.

The conclusions of the entire effort, along with recommendations for future work, are provided in Section 12.0.

This contract culminated with the installation of a stretched-membrane prototype that successfully demonstrated the improvements in the commercial design. The optical accuracy is equal to or exceeds the Mark I prototype and glass/metal heliostat designs. The stability of the focus, and response to transient error, has been improved.

2.0 Rear Membrane Restraint

A primary concern in the design of the Mark I stretched-membrane heliostat was the dynamic accuracy of the mirror module. The front, or optical, membrane focus was maintained with a small pressure differential that was the same order of magnitude as the dynamic pressure of the wind. Although membrane deflection was a reaction to pressure changes, a small change in membrane position caused a large change in plenum volume. The front membrane position was held constant, or nearly constant, by an active control system. The rear membrane was free to respond to the varying pressures created by the control system and wind. Consequently, the active control system was actually regulating the plenum volume in response to changes in the rear membrane position. Restraint of the rear membrane in the Mark II design was, subsequently, considered to improve performance under windy conditions by reducing this rear membrane deflection. The concept was originally proposed by Clay Mavis of Sandia National Laboratories, Livermore.

A hard attachment between the rear membrane and support structure of the heliostat was provided for the improved commercial design developed in this contract. This attachment decreased the loads on the ring frame and reduced the volumetric response to wind. The control fan was also relocated to the front of the heliostat to maintain the load reduction and improve the controlled response. The development of the rear membrane restraint, and the associated fan relocation, is presented in two major sections:

2.1 Load Reduction, and
2.2 Volumetric Response.

The restraint of the rear membrane reduced the normal[1] ring loads by 13%, and radial loads by 5%. The change in plenum volume was decreased by 38% over the free rear membrane used in the Mark I design. Relocation of the fan port allowed the load reductions to be maintained while the fan was inoperative. The front referenced fan also decreased the time required for defocus under windy conditions.

---

[1]Normal forces refer to loads that are perpendicular to the plane defined by the ring frame. Radial and circumferential loads are directed within the ring plane.

2.1 Load Reduction

A rear membrane restraint reduces normal and radial load reaction in the ring frame. Normal loads imposed on the stretched-membrane mirror module by the wind are transferred through the membrane to the ring frame, trusses, and, ultimately, to the drive. Rear membrane restraint provides an additional load path for direct transfer of a fraction of the normal load. Radial loads imposed by diaphragm tension, a reaction to the membrane deformation itself, are also reduced by the decrease in rear membrane deflection.

A direct transfer of a portion of the normal load, combined with the reduction in radial load, decreases the stress and deflection of the ring frame. Maximum stress is the determinant in ring frame weight; slope error is proportional to ring deflection. Consequently, the weight and error are reduced with the provision of a rear restraint.

The objective of this analysis was direct comparison of loads for the baseline free rear membrane, attached at the perimeter only, and the restrained membrane, attached at the perimeter and center. The nonlinear response of the membrane, in reaction to normal loads, was defined with ANSYS [2]. The analysis was limited to a center restraint of the rear membrane only. Restraint of the front membrane was not considered to avoid adverse impact upon the optical shape. A single center restraint, as opposed to multiple restraints over the rear membrane surface, was selected to limit the required membrane reinforcement while maximizing the reduction in loads and volumetric response.

The comparison of free and restrained membranes was typically made through presentation of load ratios; restrained loads were normalized to the free load. This approach was adopted because the ratios were relatively independent of other load variables. The restraint was defined, the normal and radial load reduction was established, and the model was examined to ensure that loading conditions and results were similar to those anticipated in the heliostat.

The first step in the analysis was to establish the radius of restraint. The load used in the model was 0.040 psi (90 Pa), equivalent to the dynamic pressure of a 50 mph (22 m/s) wind. Primary cases were run with an initial tension of 60 lbs/in. (10.5 kN/m), although secondary cases run at 30 and 45 lbs/in. (5.2 and 7.9 kN/m) indicated that the initial tension was not a major factor in the definition of peak stress. The maximum stress predicted with finite element analysis in the rear membrane is plotted as a function of restraint radius in Figure 2.1. Rear membrane stress is not uniform with a central restraint, but peaks near the load transfer point.

A 24-in. (0.6-m) radius was selected for the rear membrane restraint, based upon membrane stress alone. The stress distribution in the radial and circumferential direction for this restraint radius and loading condition is plotted in Figure 2.2. The stress concentration was confined to a small region at the edge of the restraint. Consequently, a reinforcement pad was selected as an expedient and inexpensive method to locally increase membrane cross-sectional area and thereby reduce the stress concentration.

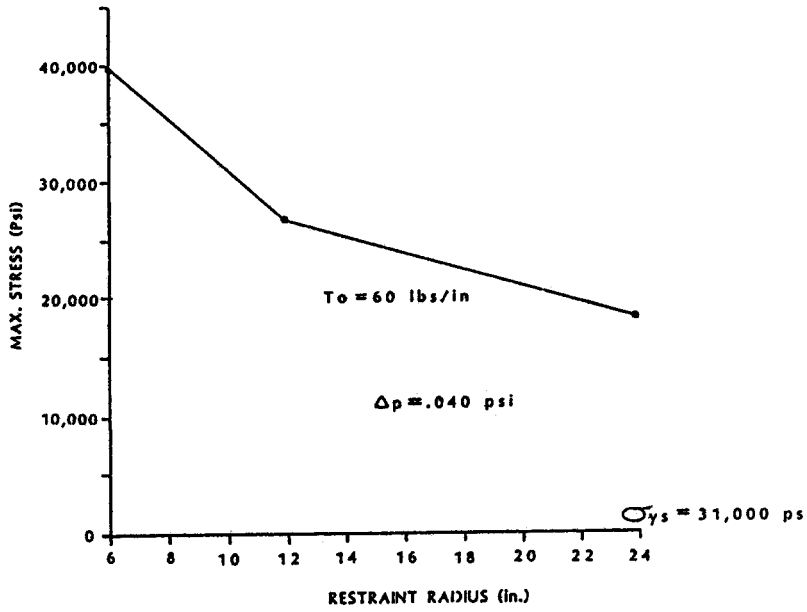

Figure 2.1 Peak Membrane Stress as a Function of Restraint Radius.

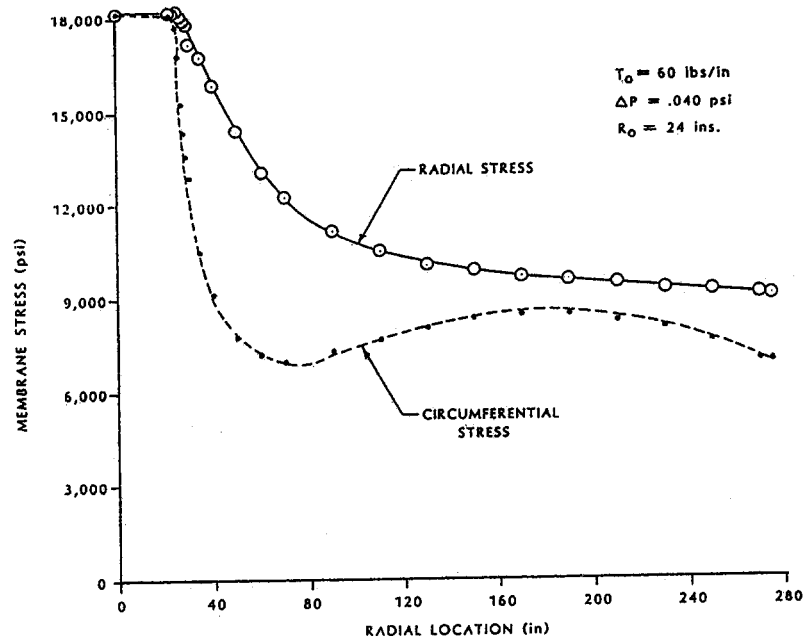

Figure 2.2 Radial and Circumferential Stress Distribution in a Restrained Membrane.

The second step in the restraint analysis was the consideration of the normal load reduction at the mirror-module perimeter. The normal load reduction was established based on initial tension and pressure loads, although the load ratio proved to be relatively independent of both variables. Figures 2.3 and 2.4 illustrate these relationships. For a restraint radius of 24 in. (0.6 m), the fixed membrane transferred approximately 25% of the load directly to the drive. The transfer occurred in the restrained membrane only. The front membrane was not restrained. The total load reduction associated with the rear restraint was, therefore, approximately half of that predicted for the rear membrane only.

A reduction of normal load transferred to the perimeter also decreased the forces applied at the end of the cantilever trusses, which formed the mirror-module support structure. The maximum tip load at 50 and 90 mph (22 and 40 m/s) for the free and fixed rear membrane is shown in Figure 2.5. Truss design was based upon load. Consequently, the total normal load reduction of 12 to 13% achieved with the rear restraint reduced the truss weight.

The third step in the restraint analysis was to establish the reduction in radial load on the ring frame. The radial load was divided into two components: initial membrane tension and diaphragm tension. Pre-tension is applied to a membrane to lend stability

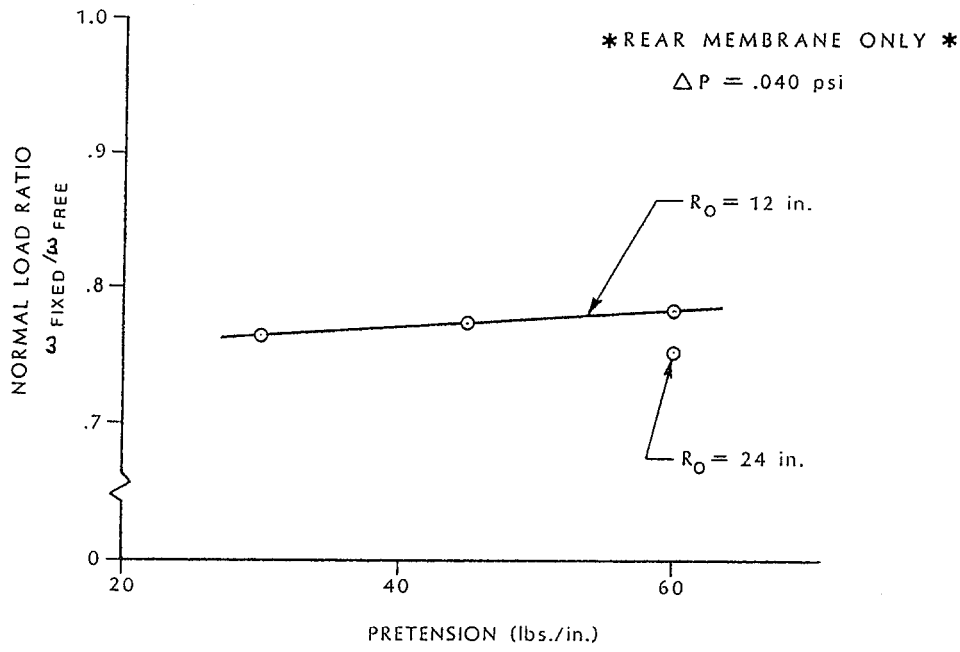

Figure 2.3 Normal Load Ratio as a Function of Membrane Tension.

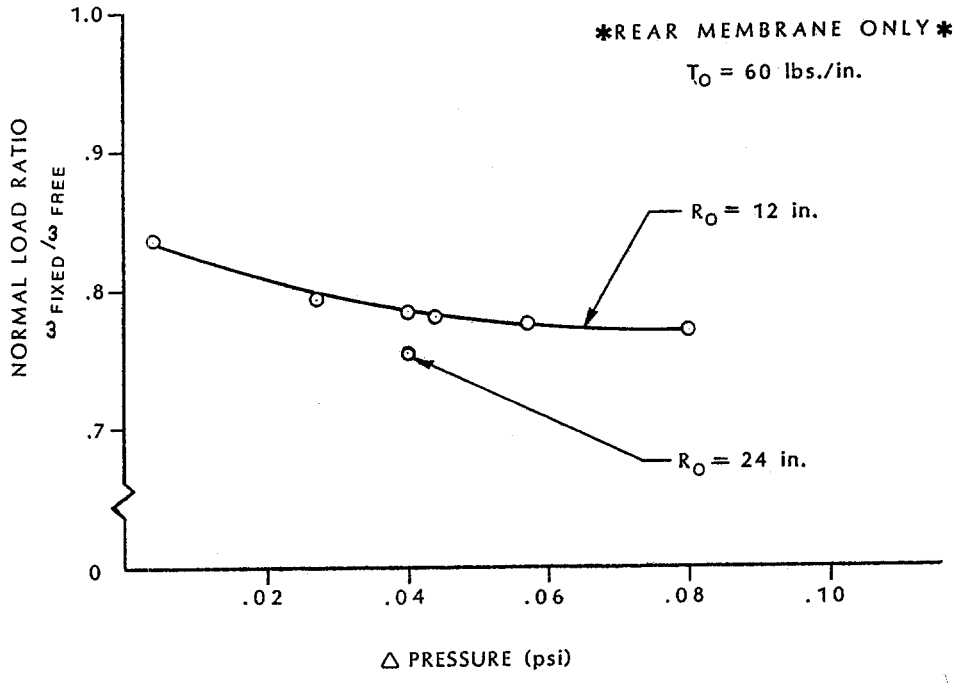

Figure 2.4 Normal Load Ratio as a Function of Pressure.

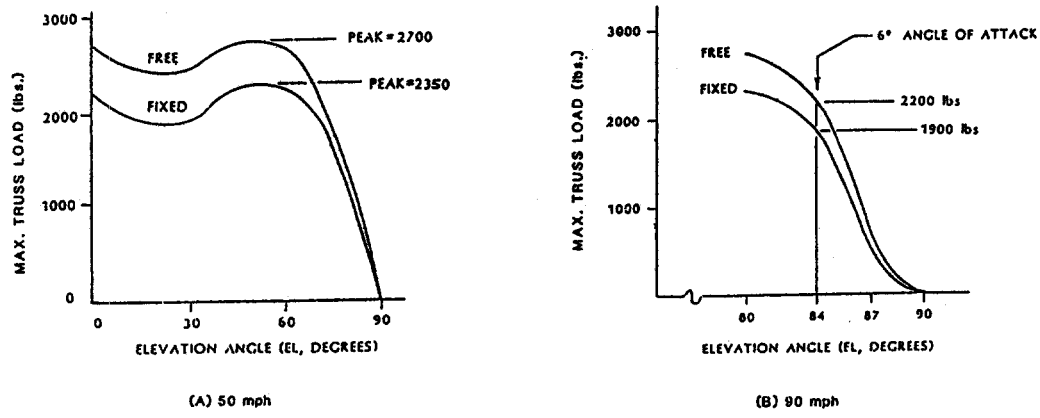

Figure 2.5 Truss Loads at Maximum Wind Conditions for the Free and Restrained Rear Membrane [Load coefficients were taken from Ref. 3].

to the heliostat. This term was constant and equal in both the fixed and free rear membrane designs. Diaphragm tension, on the other hand, was not equal and varied as a function of membrane deflection. The differential element length, in both the radial and circumferential directions, increases as the membrane assumes a deformed shape. This strain is dependent upon the actual shape of the membrane under pressure load.

The diaphragm tension ratio (restrained to free membrane) is shown in Figures 2.6 and 2.7 as a function of pre-tension and pressure. The ratio was relatively independent of both variables. This secondary tension component was reduced by approximately 33% in the rear membrane only for an attachment radius of 24 in. (0.6 m). Radial loads on the ring frame are directly proportional to the sum of primary (i.e., initial) and secondary membrane tension components in both membranes. Consequently, the net reduction in the radial frame load associated with a rear restraint was only 5%.

The final step in the load reduction analysis was consideration of the model applied to the actual heliostat. The finite element model was constructed with the rear membrane only; the results presented in Figures 2.3 through 2.7 were for that membrane only. Analysis of the double membrane design, particularly for the steady-state, passive (fan inoperative) condition suggested that all of the load could be applied to the front membrane if the fan was ported to the rear.

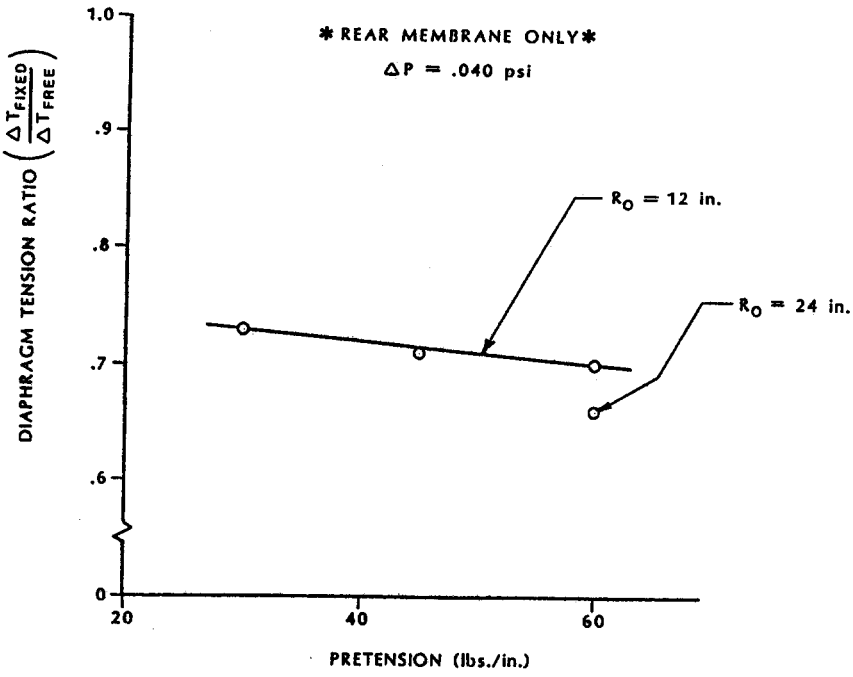

Figure 2.6 Diaphragm Tension Ratio as a Function of Membrane Tension.

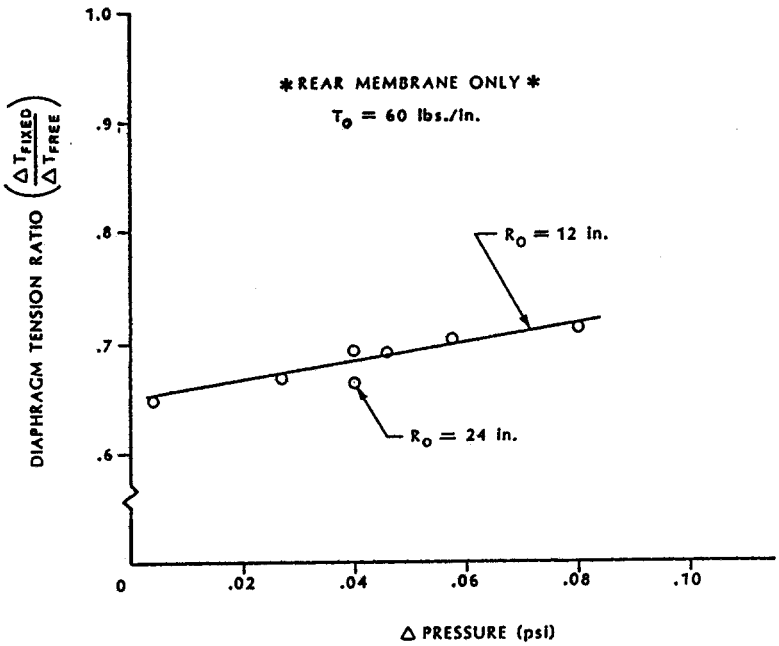

Figure 2.7 Diaphragm Tension Ratio as a Function of Pressure.

The pressure will equalize across the fan port under steady-state conditions. If the fan port were located in the rear membrane, all dynamic pressure differential could occur across the front membrane. This loading condition would negate the reduction gained through the use of a central restraint in the rear membrane. If, on the other hand, the port were located in the front membrane, there would be no conditions in which all of the load was sustained by the front membrane. Consequently, the fan port was moved to the front membrane.

This load condition was tested qualitatively with a 49-in. (1.2 m) diameter, double-membrane heliostat model. The wind was simulated with a large diameter fan. For both windward and leeward locations, the ported membrane did not carry the load. Instead, the load was transferred from the membrane to the ring frame by the non-ported membrane.

The volumetric efficiency of an axial fan, selected for the prime mover in the active control system, decreases as the pressure across the fan increases. The position of the front membrane only was controlled. Consequently, a front reference allows the fan to operate at design pressure and flow conditions without regard to wind direction. The volumetric improvement associated with fan reference was not investigated in this contract. The improvement in dynamic accuracy that resulted from the central restraint is presented in the following section.

2.2 Volumetric Response

A central restraint reduces the change in plenum volume under transient wind conditions. Slope error, caused by changes in the dynamic pressure, is corrected with active control of plenum pressure. The correction rate is dependent upon the volume of air that is moved. The membrane defocus rate has the same volumetric dependency.

Volumetric response for the fixed membrane was established with deflection results from the same finite element models used to define load reduction. Deflection results were combined with codes that modelled the conservation of mass and flow in the plenum. The initial membrane shape was flat. Consequently, the results of the model applied to both positive or negative pressure differentials. The primary case was modelled with a differential pressure that represented operation in calm conditions; the initial tension was 60 lbs/in. (10.5 kN/m). The displacement of the membrane, for the fixed and free shape, is shown in Figure 2.8 as a function of the radial position.

The ratio of fixed to free volume was also established as a function of pre-tension and pressure, but the actual reduction in volume was relatively independent of both variables over the investigated range. These volume ratios are shown in Figures 2.9 and 2.10. The displaced volume of the fixed membrane was 62% of the free membrane case at a restraint radius of 24 in. (0.6 m). In other words, 38% less air needed to be moved in response to transient winds with a central restraint.

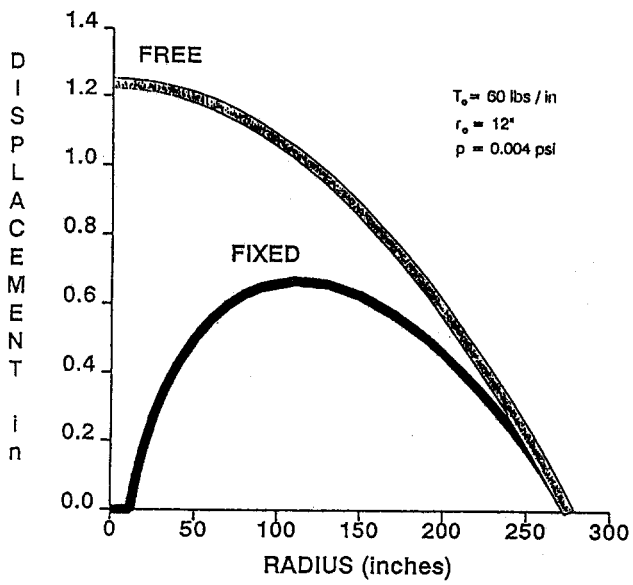

Figure 2.8 Rear Membrane Displacement for 1280 ft. (390 m) Focal Length.

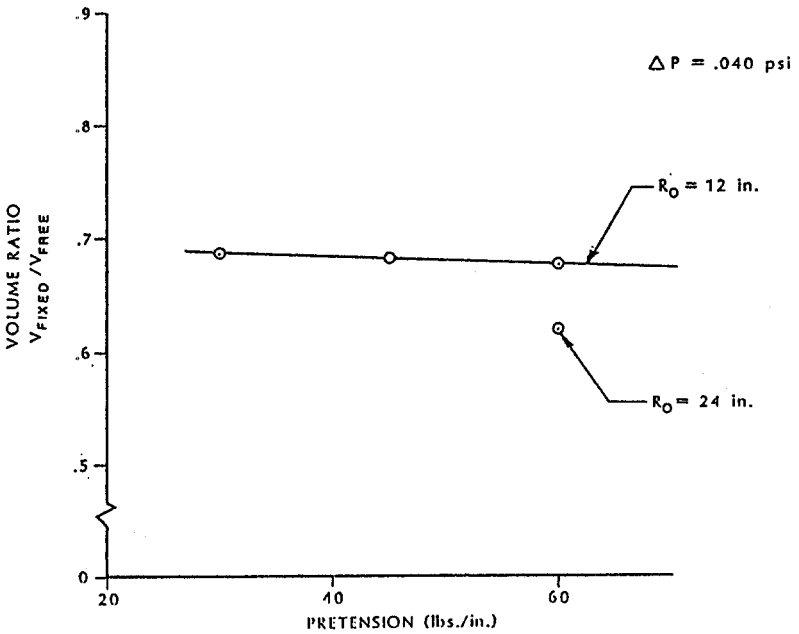

Figure 2.9 Volume Ratio as a Function of Pre-tension.

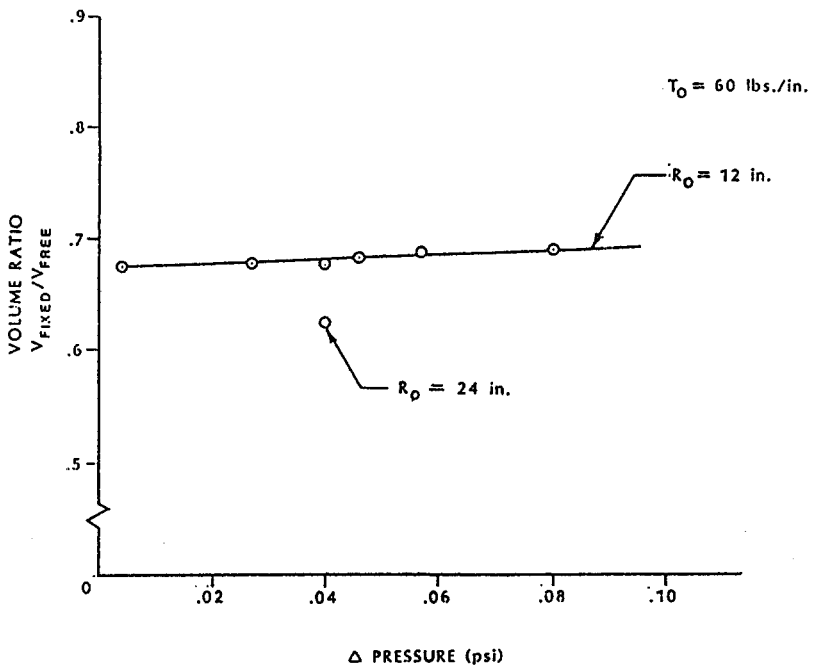

Figure 2.10 Volume Ratio as a Function of Pressure.

The analysis of volumetric response indicated that the amplitude of error, as well as the response rate, was reduced for the central restraint. In transient wind conditions, the membranes deflect and, consequently, alter the plenum pressure. The stiffness of the rear membrane is increased by the restraint; deflection in response to windward or leeward gusts is reduced. Conservation of mass dictates that the front membrane reach equilibrium with less deflection for an equivalent dynamic pressure change. These primary transient errors associated with volumetric response are axisymmetric, and independent of the support structure.

A secondary source of error from pumping action occurs with a restrained membrane only. Relative motion between the support structure and restrained membrane affect the volumetric response of the heliostat. This secondary error term is also axisymmetric, but is dependent on the stiffness of the support structure. Axial symmetry implies that the error is independent of the number of supports. The pumping action increases the error for the fixed membrane in a front wind; the error is reduced in a rear wind. Primary and secondary transient error response is shown in Figure 2.11. The net reduction in the transient error associated with the central restraint was 20%.

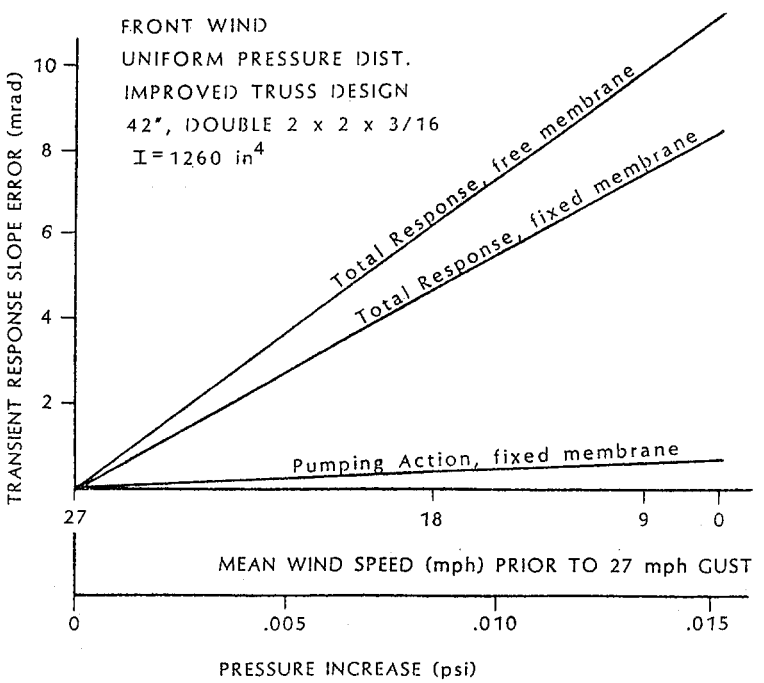

Figure 2.11 Transient Slope Error in Response to Wind Gusts.

The combination of the rear restraint and front fan reference also reduces the time required for defocus, as is shown in Figure 2.12. A 2400 ft. (730 m) convex radius was selected for defocus to allow direct comparison with the Mark I analysis. The restraint reduced the defocus time because a smaller volume of air was required to increase the plenum pressure. The front referenced fan, particularly for the leeward fan port case, also substantially reduced the defocus time. The pressure differentials across the fan and front membrane are equal for a front reference. The pressure across the fan can be substantially higher than the front membrane pressure differential during head winds; the higher pressure differential would reduce the volumetric flow rate of the fan.

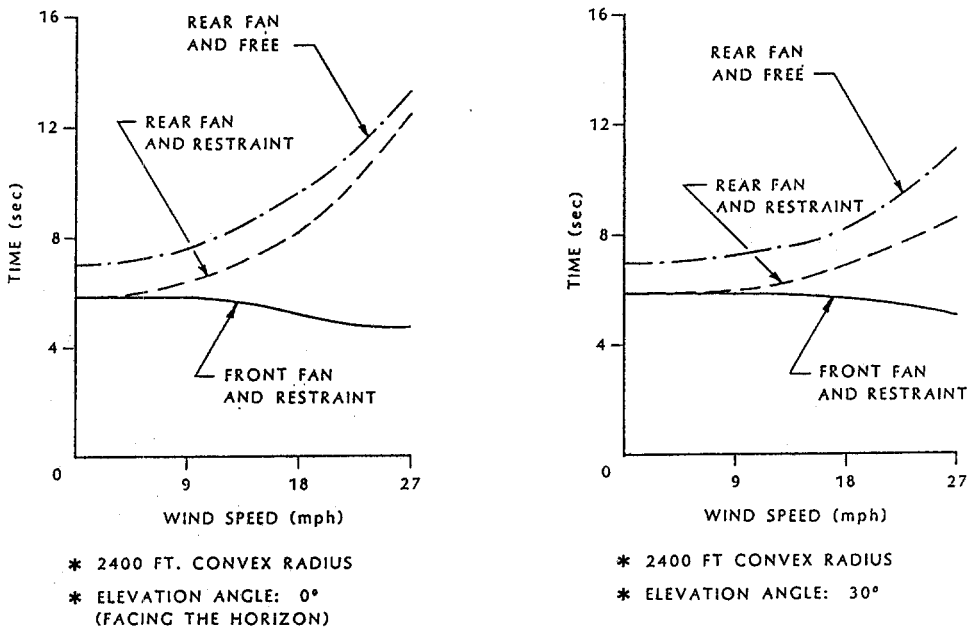

Figure 2.12 Defocus Times Based Upon Membrane Boundaries and Fan Reference.

The central restraint of the rear membrane, combined with proper fan reference, was a key element in the design improvement. The magnitude of transient slope error and the rate to correct transient error were independently reduced by the restraint. The reduction in normal and radial load on the ring, also inherent with a central restraint, was applied to the structural design of the frame and is described in the following section.

3.0 Design of the Open-Section Ring Frame

The ring frame design of the Mark I stretched-membrane heliostat resulted in a closed, rectangular tube. The ring cross-sectional area was determined by the compressive reaction to membrane tension. A closed section was selected to provide torsional rigidity. The rectangular tube allowed the flexural rigidity in the normal and radial directions to be optimized separately. Torsional rigidity was originally provided in anticipation of torque loads imposed by normal forces on a circular beam; flexural rigidity in the radial direction was initially thought to be required to prevent buckling.

During the Mark I development, analysis by Murphy et al. [4] indicated that ring frames for double-membrane mirror-module designs are not subject to significant torsional loads. The planar stiffness of the membranes relieves the torque in the ring. This work also showed that the membrane forces the critical radial buckling mode to a high order. Consequently, the planar flexural rigidity is not an important design criterion for the ring frame.

The ring frame in the development of the Mark II mirror module was redesigned as an open section. The cross-sectional area was defined by the compressive load, but the area was redistributed to maximize the out-of-plane flexural rigidity. The open section also simplified fabrication with the elimination of a welding step and reduced two nesting high-tolerance parts to a single component.

The structural development for the ring frame was limited to analysis of an aluminum channel of constant thickness. The flexural rigidity was optimized based upon the area moment only. A channel was selected to maximize the out-of-plane moment of inertia within the constraints of providing a welding platform for the attachment of the membrane to ring while keeping the inactive aperture to a minimum. A constant thickness was selected to allow the channel to be roll-formed from strip, as shown in the previous report [1].

The ring frame design is presented in three subsections:

3.1 Compressive Reaction to Membrane Tension,
3.2 Bending and Cross-Sectional Distortion, and
3.3 Stability.

The prototype design followed an identical design procedure; the results are provided at the end of this section.

The membrane tension selected for the commercial design was 45 lbs/in. (7.9 kN/m). The ring frame cross-section was a channel, 8.25 x 1.25 x 0.29 in. thick (210 x 32 x 7 mm). The prototype ring frame was an American Standard channel with a nominal size of 6 in. x 1.92 lb/ft. (150 mm x 2.86 Kg/m).

3.1 Compressive Reaction to Membrane Tension

The ring of a stretched-membrane mirror module prevents collapse about the optical axis with a compressive reaction to the membrane tension. The frame design was primarily based upon stress; definition of the compressive load was a key element in this design. The reaction was determined by verifying the assumptions used in the analysis and determining the tensile load in the membrane. The initial tension selected for the commercial mirror-module design was 45 lbs/in. (7.9 kN/m). The compressive load in the ring was established based upon hoop stress.

The ring frame was not concentrically loaded by the membrane because the attachment point was not coincident with the centroid. The compressive stress was calculated for an eccentrically loaded cylinder and compared to the hoop stress for the "thin-walled" assumption. The difference in tangential stress for the two approaches was less than 1.1 percent. Consequently, the simpler thin walled assumption was adopted. The hoop stress was expressed as:

$S = T_t a / A$ where S = Compressive stress,
T_t = Total membrane tension,
a = Radius of ring, and
A = Cross-sectional area of ring.

The radius of the ring was defined by the desired aperture of the collector. A direct relationship between the ring compressive stress and cross-sectional area could be established if the membrane tension were known.

The membrane load was composed of both initial and diaphragm tension. Initial tension was the preload applied to the membranes which established the pressure-to-deflection relationship. The diaphragm tension was a result of membrane deformation; the differential element length in the radial and circumferential directions increased as the membrane assumed a deformed shape. The diaphragm tension increased as initial tension decreased. Consequently, the minimum ring cross-sectional area was not zero, even in the absence of preload. This relationship is shown in Figure 3.1. The area required for the initial tension alone is shown with a broken line. The area required for the total membrane tension is shown with a solid line. The difference between the two lines is the effect of diaphragm tension.

The axisymmetric slope error, induced by transient wind conditions, is inversely proportional to the initial tension. The minimum ring cross-sectional area occurred at zero preload, but the transient error was maximum at this point. Consequently, the selection of initial tension was a compromise between the weight associated with area and slope error. The asymmetric error, induced by steady or transient pressure, was small by comparison to the axisymmetric term and was not considered in the selection of membrane tension.

The error terms are plotted as a function of initial tension in Figure 3.1 as well. The transient error is for a wind gust that exerts a dynamic pressure of 0.003 psi (21 Pa)

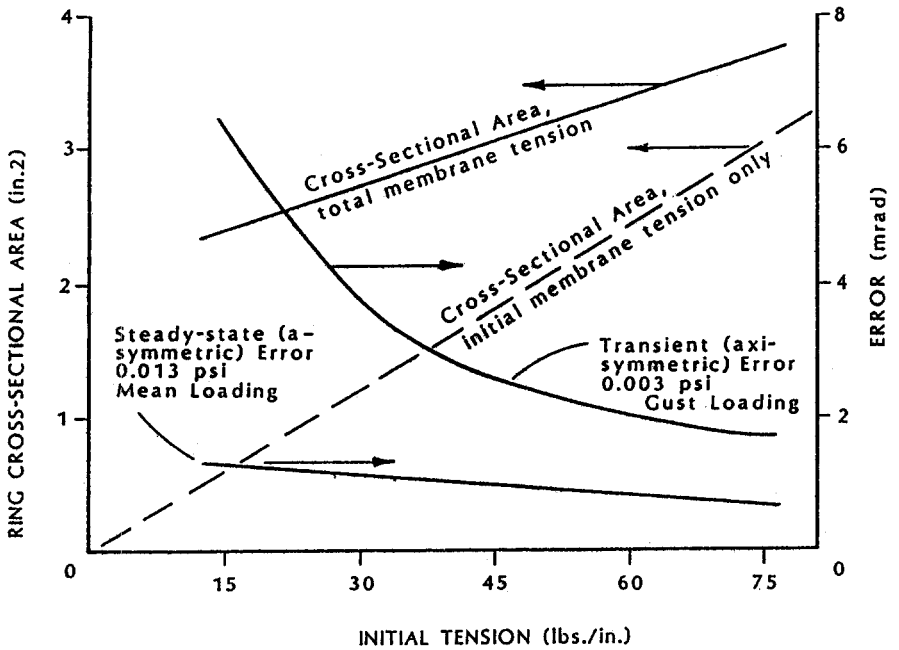

Figure 3.1 Minimum Ring Cross-Sectional Area and Slope Error as a Function of the Initial Membrane Tension.

above the mean pressure; the steady case for a mean of 0.013 psi (90 Pa).[1] The axisymmetric error is transient because the active control system compensates for membrane displacement. The error was also directly proportional to the dynamic pressure. Consequently, the transient error curve would demonstrate a sharper knee with higher pressure changes, and a flatter response with smaller pressure changes. The asymmetric term was a result of ring deflection between six trusses.

A membrane tension of 45 lbs/in. (7.9 kN/m) was selected to keep the transient error low. This selection of membrane tension was somewhat arbitrary. A lower tension would have increased the transient error and control system response time with a slight reduction in ring frame weight. A higher tension would have had the opposite effect. The final selection was, ultimately, made to keep the assembly tension, discussed in the section on tooling, substantially below the membrane yield strength. The response of the prototype in gusty winds should demonstrate the adequacy of the selection.

---

[1]This transient pressure corresponds to a wind gust, the magnitude of which is dependent upon the mean wind speed. For example, a gust to 13 mph from a mean of 0 mph, to 15 mph from 8 mph, or to 27 mph from 24 mph (5.8 from 0, 6.9 from 3.6, or 12 from 10.6 m/s) all apply a dynamic pressure of 0.003 psi (21 Pa). A mean, steady-state pressure of 0.013 psi (90 Pa) corresponds to a 27 mph (12 m/s) wind.

3.2 Bending and Cross-Sectional Distortion

The ring of a stretched-membrane mirror module provides the flat plane necessary for optical accuracy while transferring the normal loads to the support system. Bending loads distort the planar surface and are the second major source of stress in ring frame design. Normal loads induced by wind, gravity, and unequal membrane tensions are the components of the bending moment. Stress and deflection decrease with an increase in the the ring area moment. Cross-sectional distortion is the mechanism that limits the area moment that can be achieved with the distribution of the material defined by the compressive load.

The normal loads of wind and weight impose a bending moment on the ring because the frame is attached at discrete points to the truss support structure. The reaction to these normal loads is similar to a conventional, simple supported beam under a distributed load. Normal loads applied to a circular frame typically create a bending moment and torque on the beam. The double-membrane mirror module is not conventional in this respect; the ring torque load is relieved by the planar stiffness of the membranes. The bending moment that results from the normal load was defined in this analysis with the two-term approximation developed by Murphy [5].

The centroid and shear center of a channel section are not coincident. A centroidal attachment of the support structure to the ring would have imposed a torque of 830 in.-lb (94 N-m). Consequently, the normal load reaction in the support was taken at the shear center of the beam. This location for the attachment, combined with the double-membrane design, virtually eliminated all torsional load from the circular ring frame.

A bending moment was also imposed by an inequality in the front and rear membrane tension. The moment arm was equal to half the ring height. The load was simply the difference in membrane tension. In a straight section, this type of load resulted in torque. In a circular beam, the diameter of the beam surface attached to the highly tensioned membrane was decreased; the opposite beam surface increased in diameter. This change in diameter loaded the opposed flanges in tension and compression. The result was essentially a bending moment similar to the load imposed by the normal forces.

The major difficulty in establishing this bending component was the relationship between ring height and tension in each membrane under different load conditions and boundaries. Murphy et al. [4] described the diaphragm tension based upon membrane and ring spring constants for single membrane designs. A static model of ring compression and roll spring constants, along with the coupled double-membrane spring constant, was developed within the scope of this contract. This static model was combined with the finite element results for the restrained rear membrane model to establish the disparity in membrane tension as a function of the ring stiffness.

The out-of-plane moment of inertia reduced both the stress and asymmetric error associated with the bending moment. The objective was to distribute the mass defined by the minimum cross-sectional area to maximize this area moment. The minimum flange width required for the welded membrane attachment was approximately 0.75 inches (19 mm) plus twice the thickness to allow for the web and bend

radius. Optimization of the area moment became a function of height alone, given the constant ring thickness assumption and definition of the minimum flange width.

Cross-sectional distortion was established as one limit to the ring height. The equal membrane component in the front and rear membranes decreased the diameter of the flanges while increasing the diameter of the web. This distortion of the channel-shape resulted in secondary bending stresses across the section.

The distortion was estimated with iterative definition of the strain energy for the structure. Strain energy in the mirror module was defined as the sum of the membrane tension, flange compression, web compression, and web bending components. Flange bending was neglected. The sectional deflection reduced the membrane tension strain energy component while increasing the flange and web distortion components.

This approach was adequate to demonstrate the trend in radial deflection and secondary bending stress in the channel web. Finite element analysis of the channel selected

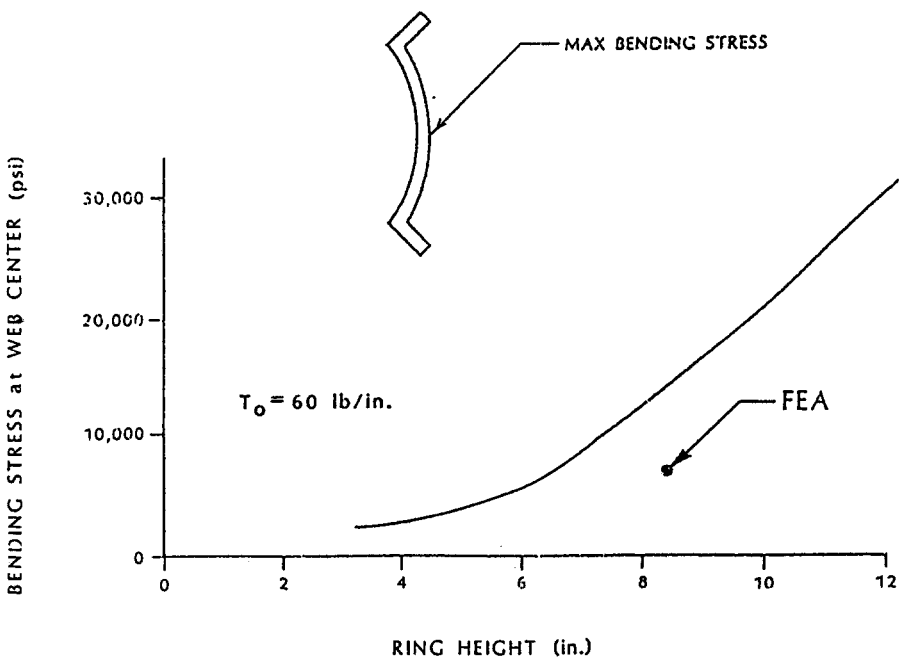

Figure 3.2 Secondary Bending Stress in the Ring Web from Cross-Sectional Distortion.

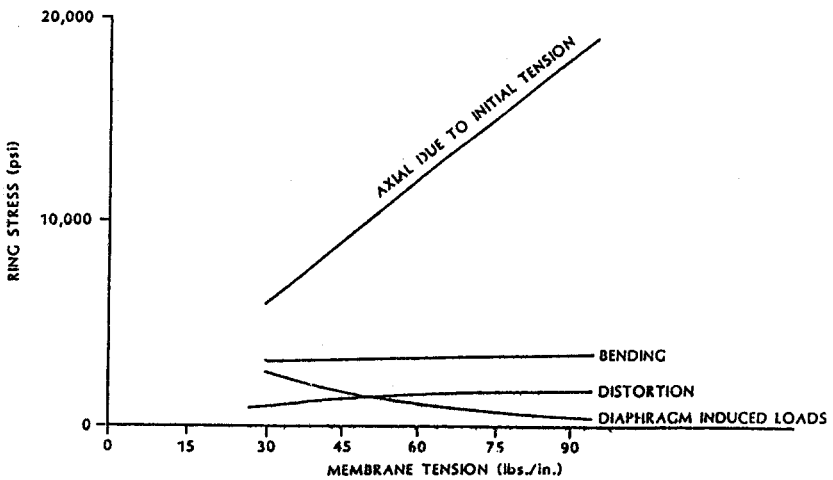

Figure 3.3 Relative Magnitude of Stresses in the Ring Frame.

for the final design provided an exact solution for the single case. The results of the analysis are shown in Figure 3.2. The secondary web bending stress did not sum to the primary out-of-plane bending stress. Primary bending stresses were at a maximum in the flange rather than in the web and oriented in the orthogonal direction. The stress due to distortion did not limit the ring height in the final design. The analysis did indicate that the reduction in membrane tension caused by cross-sectional distortion was less than 5%.

The relative magnitude of each stress component, at the point where the stresses combine to a maximum, is plotted in Figure 3.3. This diagram is based upon an intermediate channel design; the channel ultimately selected for the commercial design did not significantly alter the relative magnitude of loads. Ring design based upon stress was clearly most sensitive to the selection of initial tension. The asymmetric error term associated with ring deflection was not the major basis for ring design because the error component was small (see Figure 3.1).

The design based on stress was also adequate for gross ring stability, as is shown in the following section. The local web stability ultimately provided the limit on ring height.

3.3 Stability

Localized buckling defined the limit to ring height. This stability mechanism is associated with the crippling of a beam web; the criterion is often applied to establish a "compact" section. The procedure used to define ring height was to establish a factor of safety on buckling, and determine the optimum ratio of height to thickness. This ring section was, subsequently, used to define the gross frame buckling limit in the normal and radial directions.

The web was assumed to act as a simple, laterally supported beam under compression. The formula used to establish the critical stress was developed by Timoshenko [6]. The safety factor applied to yield for stress design was 1.5. In other words, the principal stress from compression, bending, and distortion was 18700 psi (130 MPa) by design. Buckling, as a stability failure, requires a somewhat larger margin of safety to accommodate the effects of localized loads and initial imperfections. Consequently, a factor of safety of 2.5 was selected, yielding a critical stress of 46700 psi (320 MPa). The maximum height-to-thickness ratio was 28.2.

The stress for all components is plotted as a function of ring height in Figure 3.4. This figure is based upon three assumptions: the ratio of web height to thickness is 28.2,

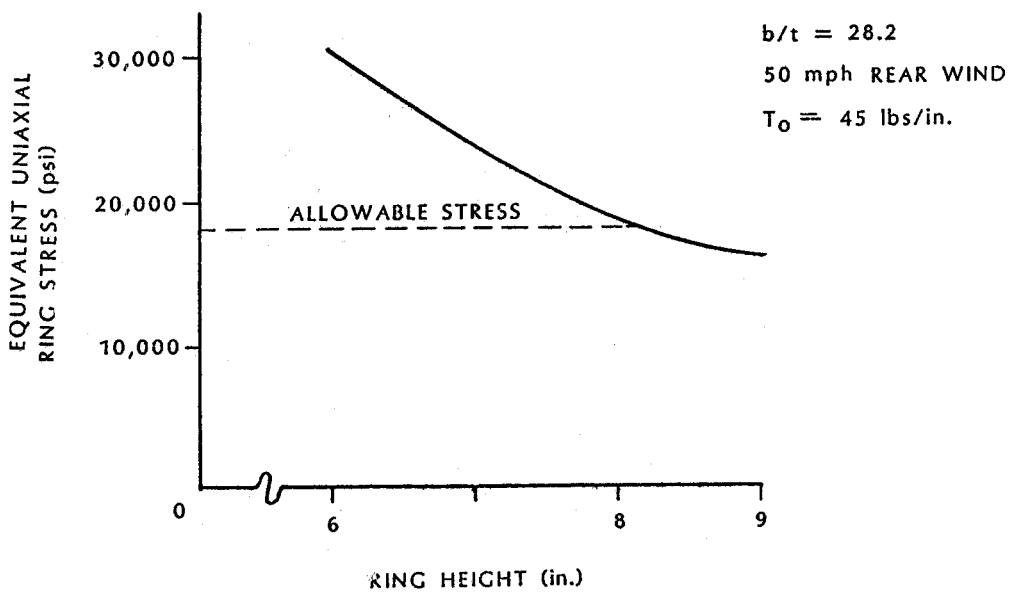

Figure 3.4 Equivalent Uniaxial Stress in the Ring Frame as a Function of Ring Height.

the flange width is equal to 0.75 in. (19 mm) plus twice the thickness, and the thickness is constant. These three assumptions, combined with the allowable stress, provided a unique and optimum ring design. The ring height at the allowable stress was 8.25 in. (210 mm). The thickness was 0.29 in. (7 mm). The flange width was approximately 1.25 in. (32 mm).

The gross stability of this ring design was subsequently considered. Radial buckling, normally a key design criterion in circular beams loaded in compression, was not a major consideration in the design. The planar stiffness of the membranes forced the critical radial buckling mode to a very high order as indicated by the work of Murphy et al. [4]. The compressive load in the ring induced by the initial tension was actually thirty times greater than the critical radial stress for the ring frame alone.

The bifurcation limit in the out-of-plane direction was defined based upon ring attachment to six rigid supports. The combined membrane tension, which forced the ring stiffness matrix [5] to zero, was determined. The safety factor on normal buckling was approximately four.

The ring frame of a stretched-membrane mirror module is effectively a long, slender column loaded in compression. The coupled membranes allows this column design to be based upon yield stress rather than gross buckling.

A similar design procedure was used to define the ring frame for the 50 m^2 prototype. The membrane tension was defined to correspond to the commercial design at 45 lbs/in. (7.9 kN/m). Channel selection was limited to American Standard shapes to avoid tooling cost. The height-to-thickness ratio was defined based upon local web crippling, and a channel was selected that kept the operating stress slightly less than the allowable stress. The ratio of actual load to the load at failure is provided in Table 3.1 for the prototype and commercial design.

Table 3.1
Factors of Safety for Commercial and Prototype Ring Frames

Failure Mechanism	Factor of Safety	
	Commercial	Prototype
Yield[1]	1.5	1.5
Web Buckling[1]	2.5	2.5
Flange Buckling	---	6
Normal Buckling	4	16
Radial Buckling	13	32

[1]These factors control frame design.

Both the prototype and commercial ring designs were based upon stress and localized stability. The out-of-plane moment of inertia was maximized to limit bending stresses and asymmetric error without adding additional weight. The asymmetric error term for the commercial design was estimated at 0.5 mrad; identical analysis of the prototype design established asymmetric error at 0.35 mrad. The difference in the commercial and prototype error values is the result of the difference in channel sizes and spans between supports.

4.0 Mirror-Module Support System

A support system transfers the loads from the ring frame of the stretched-membrane mirror module to ground. The design improvements to the support structure developed under the initial stretched-membrane effort [1] were limited to analysis of the components required for transfer of the loads between the mirror module and drive only. The drive and drive support were defined in the design of second-generation glass/metal heliostats [8], and specifically excluded from the initial stretched-membrane design or additional development within this contract. This development is presented in two subsections:

4.1 Truss Design, and
4.2 Drive and Ring Attachments.

The design improvement focused on additional definition of the load distribution and the elimination of unnecessary restraints in the structure. The truss was redesigned with hot-rolled structural steel to lower material cost rather than assembly weight. A small diameter hub was selected to simplify fabrication. Rotational restraints in the ring connection were eliminated to avoid concentrated moments at the support attachment.

4.1 Truss Design

Six trusses were selected for support of the Mark I mirror module. The greatest uncertainty in the design was the load distribution. Safety factors were, consequently, applied to the load distribution, rather than to the allowable stress. The most severe loading condition for the trusses was established as 150% of the dynamic pressure distributed over 50% of the area. The design focused on strength and stiffness at minimum weight. The truss was fabricated from sheet steel for both the primary and doubled secondary members to achieve stiffness and weight objectives.

The truss design for the Mark II stretched-membrane mirror-module support was based on recent force and moment coefficients established during wind tunnel testing [3], applied to a conventional truss configuration. The objective in the design was to minimize the support cost rather than weight, while maintaining adequate stiffness. The optimum number of trusses required for support was not reevaluated in this design development. The normal loads imposed upon the ring were transferred to the drive through six discrete supports. The development was based upon definition of the loads and design of the truss based upon stress. Conventional hot-rolled structural shapes were used for low material cost. The shapes were distributed to provide the maximum stiffness with the minimum material required for stress design.

The primary load in the cantilevered support was applied at the tip of the truss, normal to the ring plane. The loads applied by wind were defined as normal forces, lateral forces, and moments about the elevation axis based upon the aerodynamic coefficients developed by Peterka [3]. The mirror module was assumed to act as a rigid-body.This assumption allowed the normal force and moment to be resolved into a maximum truss

tip load. The maximum loads exerted on the truss by the normal force and elevation moment are shown in Figure 4.1 for all elevation angles. The peak normal truss tip load was 2350 lbs (10.5 kN) for the fixed rear membrane design at 50 mph (22 m/s) wind velocity for the most severe mirror-module position.

The specifications for a field heliostat associated with this contract [7] also required design at 90 mph (40 m/s) in the stowed position. The truss tip load for the narrow range of elevation angles that correspond to stow are shown in Figure 4.2 for the high wind speed. A peak truss tip load of 2350 lbs (10.5 kN) was reached at an elevation angle of 80° for the 90 mph (40 m/s) case. Based upon a 6° angle of attack for the wind (i.e., the wind direction may vary 6° with respect to the horizontal), the stow angle could be 4° off of the horizontal. This slightly canted position was selected for the heliostat to enhance water runoff during rain without any load penalty.

A two-dimensional Warren truss was selected for the open web cantilever beam design. The design was optimized by selecting a truss height and applying the load induced by

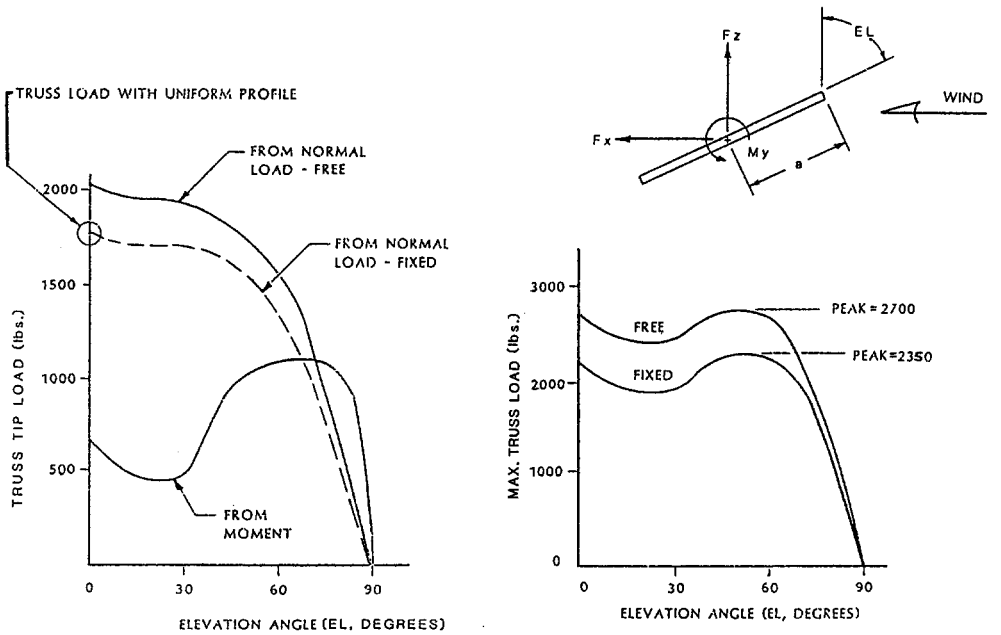

Figure 4.1 Truss Tip Loads at 50 mph (22 m/s) Wind Speeds for All Heliostat Elevations.

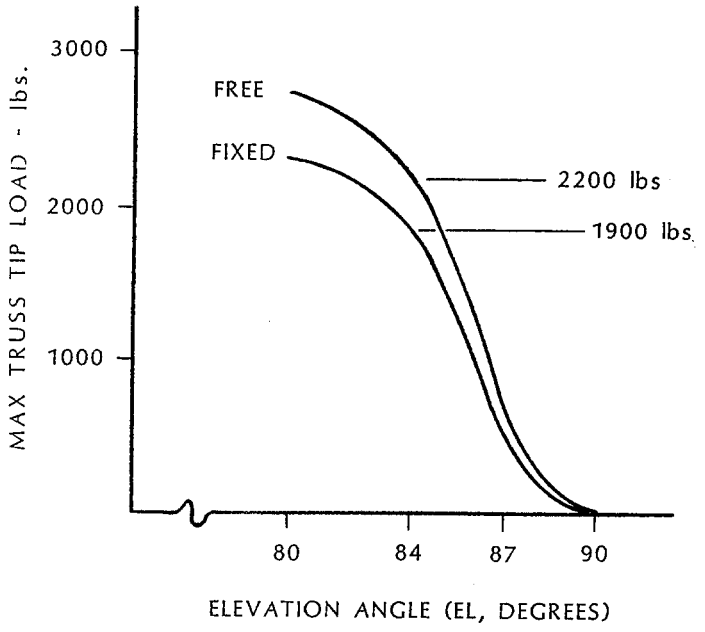

Figure 4.2 Truss Tip Loads at 90 mph (40 m/s) Wind Speeds for Stow Elevations.

wind. Both the primary and secondary members of the truss were sized to prevent buckling and keep the stress within allowable limits. The height was subsequently varied until the members sustained buckling at the allowable stress.

This procedure indicated that lateral buckling in the primary member was a major determinant in truss design. Tension straps were added to the trussed support structure to alleviate this failure mechanism; the strapping pattern is shown in Figure 4.3. The nonuniform load profile, which generated elevation moments in the mirror module, caused greater deflection at some trusses. The nonuniformity in truss deflection increased the compressive loads in some primaries. The stress from strapping loads was an order of magnitude smaller than the bending stresses imposed by wind. These secondary loads were not a major source of stress, but were included in the design.

The straps also effectively transferred lateral forces and roll moments to trusses that were oriented more favorably to react to these loads. The straps prevented these secondary forces and moments from having any significant impact upon the design. The star pattern also prevented any "windup" in the support system. Moments about the optical axis were small in the heliostat mirror module.

The design of the truss was based entirely upon open-section, hot-rolled structural shapes to use the lowest cost steel available for the structure. The conventional truss fabrication also eliminated much of the equipment cost associated with manufacture of the Mark I design. The two-dimensional truss allowed the support structure to be

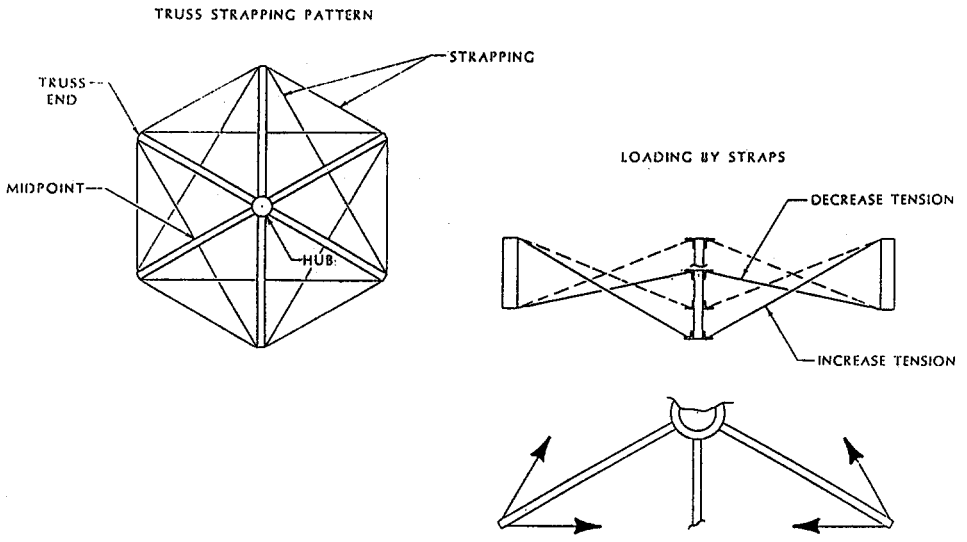

Figure 4.3 Lateral Tension Straps in the Trussed Support System.

fabricated at the central manufacturing facility and shipped to the field without significant transportation bulk.

4.2 Drive and Ring Attachments

The support system attachments were also evaluated in the design improvement of the stretched-membrane heliostat. The hub, which transferred loads to the drive, was a large diameter, trussed ring in the Mark I design. The large diameter ring was selected to allow transfer of the normal loads to the drive structure at three widely separated points. The large diameter also facilitated the rear-ported focus control system. The hub was expensive to fabricate and represented a substantial fraction of the bulk that had to be transported between the central and field manufacturing facilities.

The attachment between the mirror module and trussed beams was hinged to allow for the difference in thermal expansion between the aluminum ring frame and steel support structure. A single degree of rotational freedom was provided at each end of the hinged attachment in the Mark I design.

The size and cost of the Mark II hub were substantially reduced by decreasing the diameter of this support element. Load transfer at three separate points was maintained by passing the load to the drive through the trussed beams rather than through the hub (see Figure 4.4). The use of more substantial hot-rolled structural shapes for the truss primary allowed this transfer without substantial doublers in the support

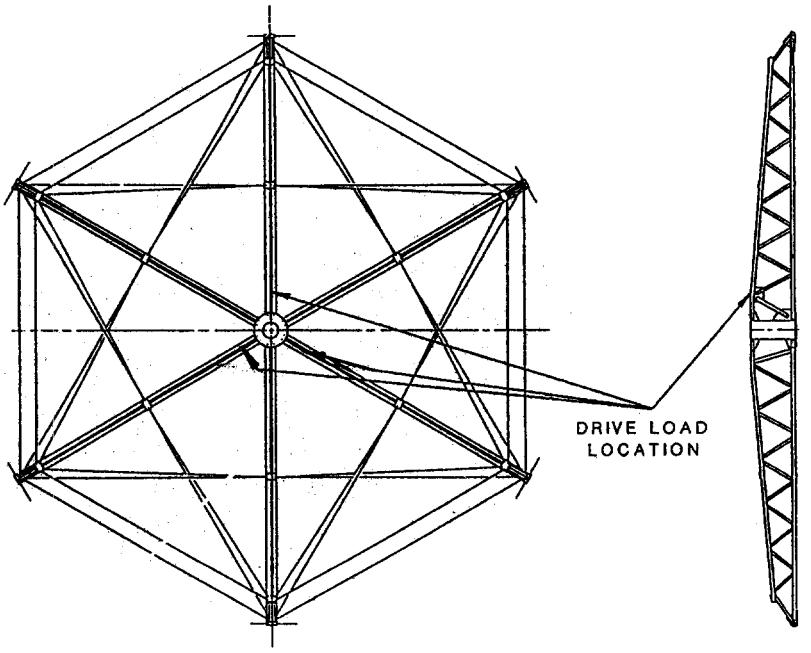

Figure 4.4 Prototype Rear Structure Showing Points of Interface with Drive.

system. The hub primarily served to transfer the root truss load from the three free trusses to the trusses connected to the drive.

The secondary dimensional constraints associated with the truss and control system connections were also alleviated in the Mark II design. The width of the two-dimensional truss was decreased with a single set of secondary elements. This allowed the truss root to attach to a small diameter hub without dimensional interference. The front referenced fan left only the defocus mechanism at the rear of the heliostat.

The hinged connection between the ring and support structure was modified in the Mark II design. Two additional rotational degrees of freedom were provided at the ring. The ring connection was effectively a ball joint. This joint, combined with the attachment near the shear center of the ring, virtually eliminated all concentrated moments in the mirror module. The size of the doubler at the connection point was reduced because of the smaller concentrated loads.

Relatively small rotational deflection was required at the ring connection because of the stiffness of the coupled mirror module. The ball joint was actually implemented by providing a layer of vulcanized silicone between two concentric tubes, as is shown in Figure 4.5. The silicone was effective at transferring normal forces, while allowing

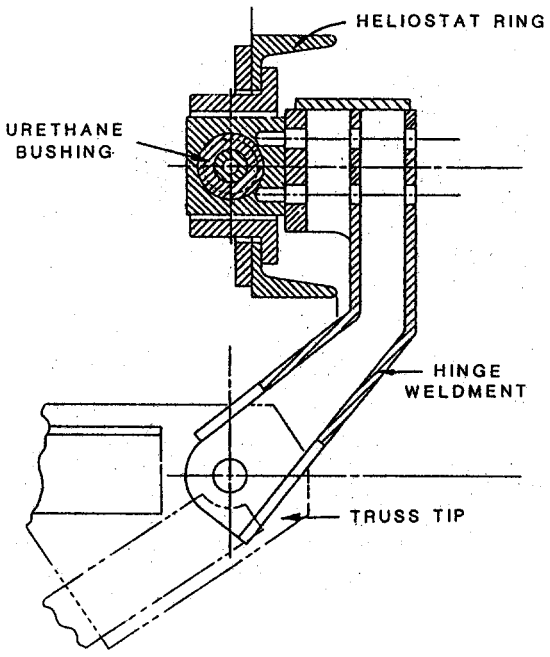

Figure 4.5 Hinge Assembly.

rotation about the radial and normal directions, because of the amount of elastomer that was compressed in each mode. Rotation about the circumferential axis was provided with a direct, hinged joint. This direct hinge was complemented by a hinge at the truss connection as well. The single degree of rotational freedom at the truss connection was required to accommodate the difference in thermal expansion between the steel support structure and aluminum mirror module.

5.0 Control System Modifications

A stretched-membrane mirror module requires active control of the optical surface in response to dynamic pressure variations caused by wind. This active control system was implemented with a closed feedback loop in the Mark I design. A linear variable differential transformer (LVDT) was used to sense membrane position; an axial fan was used for pressure actuation. The LVDT was attached to the ring frame. The rear-ported fan provided both focus and defocus actuation. The control system that was implemented on the Mark I prototype was reasonably successful. No failures in the transducer or actuator have occurred after nearly three years of operation, but an inadvertent sensitivity to elevation was noted in the transducer response because of the mounting approach. Defocus on power failure was not provided in the Mark I design.

The Mark II design improvement concentrated on the location of the transducer and actuator; defocus on power failure was also provided. Control element location was reviewed to improve response and eliminate spurious sensitivities. The ability to defocus without power completed this important receiver protection feature available only with stretched-membrane mirror modules. Alternate actuators and transducers were not considered because of the success in the Mark I prototype. The analysis is presented in two major sections:

5.1 Transducer Location, and
5.2 Defocus Mechanism.

The change from a rear to a front-ported fan is discussed in an earlier section on rear membrane restraint.

The LVDT position was shifted from the edge of the mirror module to the center. The transducer was referenced to the support structure rather than the ring frame to reduce error. A compound linkage was added to the mirror module to provide defocus in the event of power failure. The potential energy was supplied by two compression springs. The fan was also relocated, as discussed in Section 2.

5.1 Transducer Location

The optimum location of the LVDT transducer was determined with an error analysis. Three major sources of error were identified: tracking error, asymmetric error, and axisymmetric error. These three sources of error are illustrated in Figure 5.1. Tracking error was defined as the deviation between the desired and actual direction vector of the mirror-module optical axis. Asymmetric error was the variance between surface normals of a perfect parabola and the actual optical shape that resulted from ring frame deformation. Axisymmetric error was also a difference in ideal and actual surface normal vectors; the cause of the error was a uniform deformation of the membrane surface that deviated from the ideal position. The regular and defined response allowed this error to be described in terms of the center membrane deflection alone. All errors were

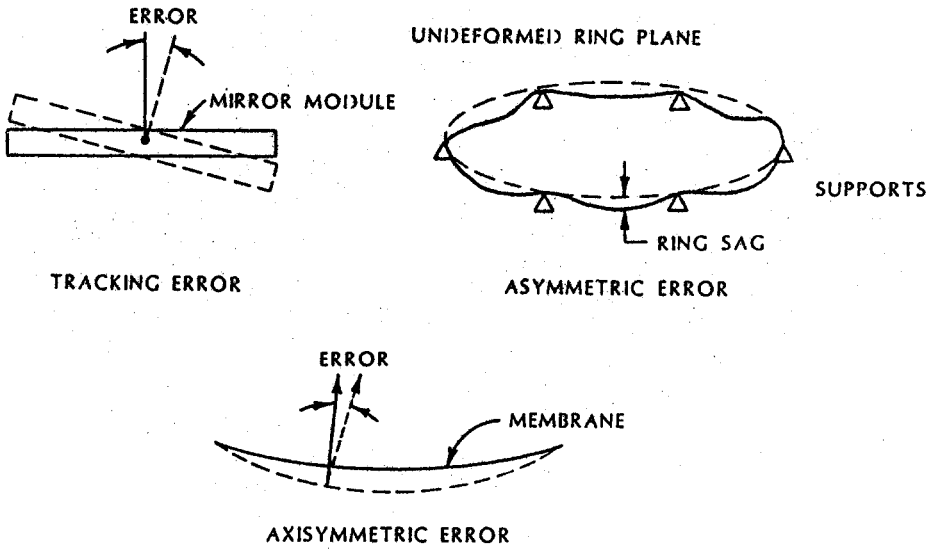

Figure 5.1 The Sources of Optical Error Considered in Transducer Location.

described at the maximum operating wind condition (27 mph, 12 m/s). Errors at lower wind speeds would be substantially reduced. All of the error terms were dependent upon elevation angle.

The tracking error of the membrane was defined based upon deflection of the support structure in response to wind loads defined in the previous section. Rigid-body motion only was assumed for the mirror module. The moments imposed by wind were applied to the support structure to determine the angular error. The tracking error also described the lower bound of optical accuracy that could be achieved without regard to transducer location.

The asymmetric error was established based upon the commercial ring design. The relationship between asymmetric error and ring deflection was provided by Murphy [9]:

$$E_a = (V / 2a)\, N^{1/2}$$

where E_a = RMS Asymmetric Error,
V = Maximum Ring Deflection,
a = Ring Radius,
and N = Number of Supports.

The ring deflection was established with the two-term design approximation [5]. The maximum deflection occurred halfway between supports. The best approximation of the ideal ring plane under any wind conditions was at the quarter point; in other words, at a point one-quarter of the circumferential distance between supports. Roll and ver-

tical displacement are inherently coupled deformations in response to a normal load for a circular ring. The ring roll was also minimum at the quarter point.

The asymmetric error associated with surface normal deviation in response to ring sag cannot be eliminated or even reduced by transducer location. The asymmetric error can be magnified, however. The ideal, average membrane position was described in terms of the center membrane deflection. The axisymmetric error, also defined by Murphy [9] was

$$E_r = 2^{.5} (w_o / a)$$

where E_r = RMS Axisymmetric Error,
w_o = Membrane Deflection Error,
and a = Ring Radius.

The membrane shape was approximated as a sphere. The transducer location amplified the asymmetric error by adding an axisymmetric term associated with position alone:

$$A = [a^2 / (a^2 - r^2)]$$

where A = Amplification Factor,
and r = Transducer Radial Position.

The ring quarter point was selected for the transducer attachment point in the Mark I commercial stretched-membrane design. The mirror-module radius was 7 m; the radial position of the transducer was 6 m; consequently, the amplification factor for any transducer displacement error was 3.7.

The quarter point represents the average membrane plane and does not roll in response to normal loads. This theory was applied in the selection of the transducer attachment point in the Mark I design without consideration of other secondary loads. In practice, the ring did roll at the quarter point in response to the radial load. A difference in membrane tension induced by the diaphragm response to wind created a uniform roll in the ring. Analysis indicated that the roll will increase with the addition of the rear membrane restraint. Ring roll alters the distance between the ring reference point and the membrane without a change in focal length. This error is amplified by the transducer position. Consequently, the ring attachment for the transducer actually caused a significant axisymmetric error, while eliminating any amplification of the asymmetric term.

The transducer attachment point was reconsidered in the Mark II design. The optical error for connection to the truss at the center and edge of the mirror module was determined. The edge location compensated for rigid body motion between the mirror module and support system in a uniform wind. The error associated with differences in individual truss deflections was amplified by the edge position, however. The center location did not amplify the differential deflection, but did suffer from the error associated with the rigid body motion. Both truss locations incurred a greater asymmetric error term because no reference was made to the ring quarter point.

The comparison for transducer locations is shown in Figure 5.2. In contrast to earlier assumptions made with regard to ring reference to eliminate asymmetric error, the error was actually lower for a support system attachment. The amplification of differential truss deflection error was offset by the rigid body motion of the mirror

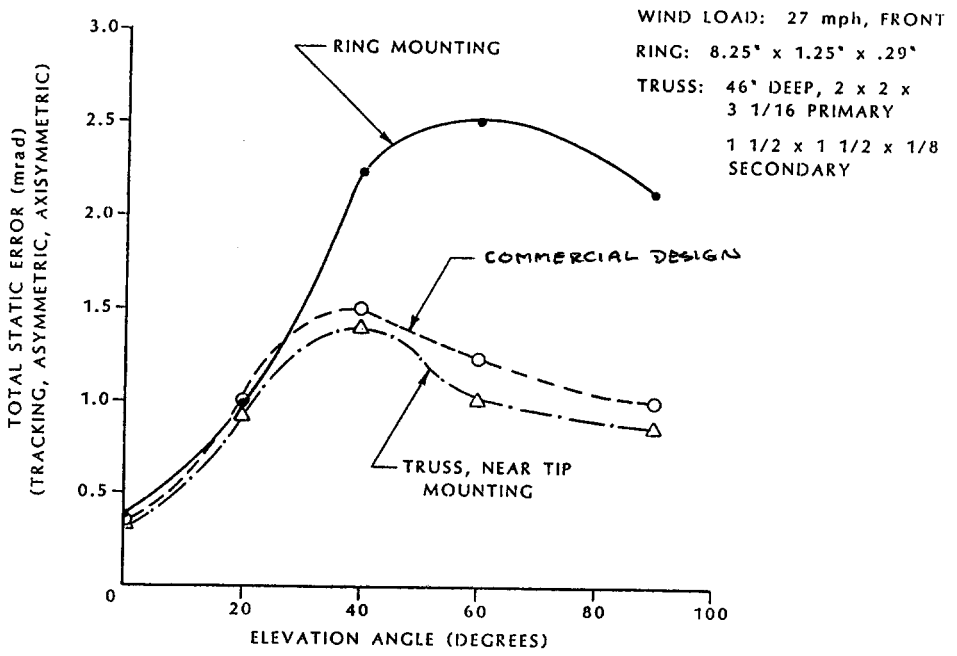

Figure 5.2 Static System Error for Different Transducer Mounting Positions.

module. Consequently, the error associated with support system reference was virtually independent of location. A center mount was selected for the Mark II design.

5.2 Defocus Mechanism

The receiver flux from a stretched-membrane heliostat can be substantially reduced by forcing the optical surface to assume a convex shape. This defocused position was achieved in the Mark I mirror module by reversing the fan direction and pressurizing the plenum. The Mark II commercial design provided the same defocus feature, with the addition of being able to initiate and maintain a defocused shape without power through a secondary mechanism. Based on analysis, the Mark II commercial design should achieve a convex radius of approximately 2400 ft. (730 m) in five seconds with fan power only. The combined use of the fan and secondary defocus mechanism should substantially increase the convex radius within the allotted time, although this analysis did not define the ability of the combined system to meet the contract objectives. Fan power was not reevaluated in the Mark II design. The fan size was based on dynamic operating requirements in the Mark I design [1].

The major objective in the design of the secondary defocus mechanism was to provide passive defocus without the addition of batteries or additional actuators. Battery banks at each heliostat were considered expensive and inefficient in supplying potential energy. Additional actuators would add to the cost and decrease the reliability of the heliostat.

The basic approach used to implement the passive defocus was to provide a force to push the optical surface forward. Potential energy was supplied by a set of compression springs. The spring was subsequently retracted on return of power by the fan used for focus control. This approach eliminated the need for batteries or actuators. The only additional active component in the system was a latch solenoid that released on power loss.

The shape of the defocused membrane resulting from an applied mechanical force will not be the same as that resulting from the uniform pressure applied by the active defocus. A membrane center displacement and a frontal wind gust would combine to create an annulus of active membrane area as is illustrated in Figure 5.3. Therefore, using a center displacement corresponding to a particular convex radius is not a sufficient indicator of when defocus is achieved.

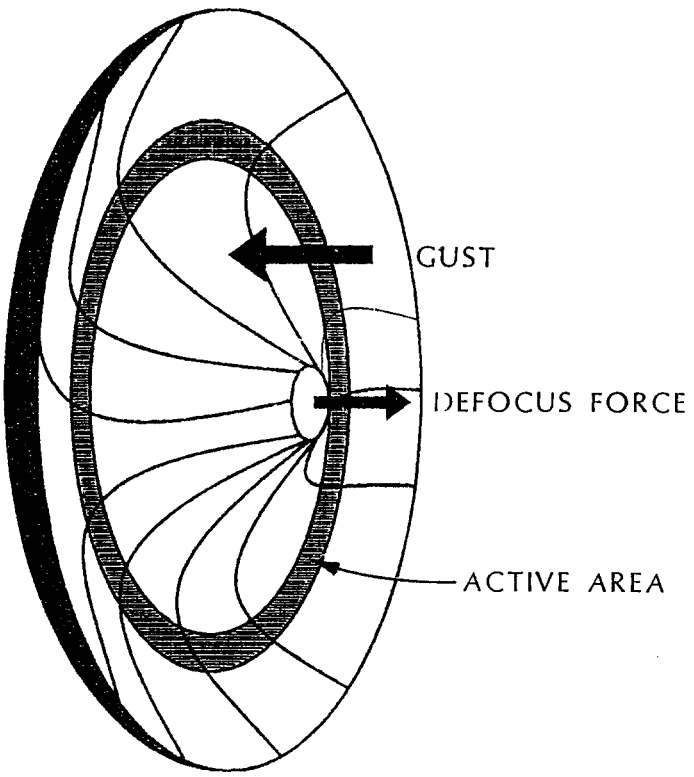

Figure 5.3 Active Area in a Defocused Mirror Module During a Wind Gust.

The first step in analysis of the secondary defocus system was to define what surface error constitutes focused, and apply that to the shape of the mechanically deflected membrane. The maximum allowable standard deviation of surface error from all sources was 1.7 mrad, as defined in contract specifications [7]. The defocused region of the mirror module was somewhat arbitrarily defined as the aperture area with a surface normal slope error greater than three standard deviations: $\pm$ 5 mrad. The region with less than $\pm$ 5 mrad of error, or the active area, reduced to zero with a center displacement of 2 in. (51 mm). Increased center deflections decreased the active area. The deflection was ultimately limited to 4 in. (102 mm) for defocus based on stress. Some active aperture area remained at large pressure differentials. This active area was considered acceptable since it was a transient phenomenon associated with a high wind gust occurring simultaneously with a power failure and adverse elevation and azimuth of the heliostat. The number of heliostats in an entire field at unfavorable orientations would be limited in any case.

The second stage in the defocus analysis was to compare the force required to achieve defocus in windy conditions with the force that could be imposed by the fan to latch the defocus mechanism on return of power. The analysis was based upon a mirror module at prototype (4 m radius) rather than commercial scale (7 m radius) because of limited funds. The force required to achieve various center deflections at different differential pressures is shown in Figure 5.4. Negative deflections again corresponded to the distance between the ring plane and a concave membrane; positive deflections were center displacements in front of the ring plane. The fan selected for the commercial design is capable of delivering 0.036 psi (250 Pa) of differential pressure.

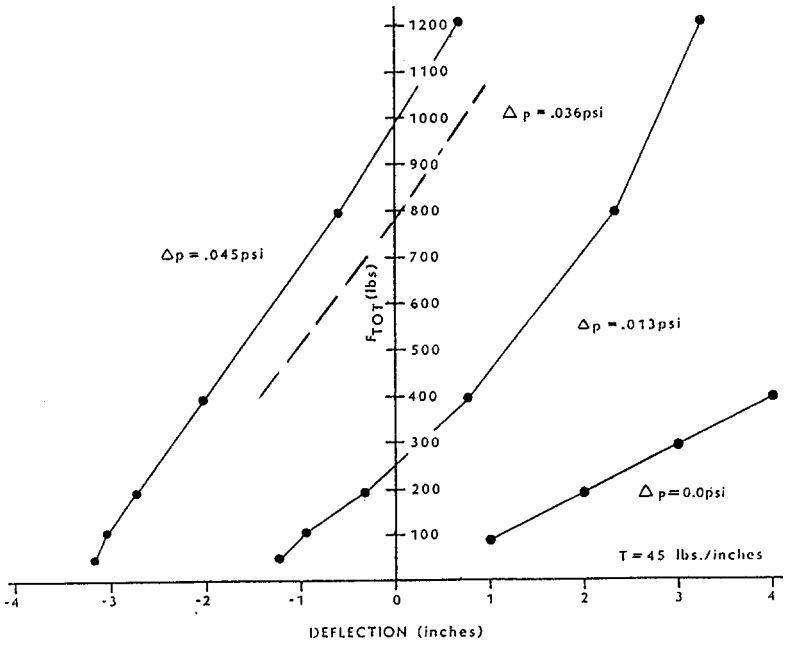

Figure 5.4 Defocus Force Required at Various Membrane Deflections and Pressure Differentials.

The figure illustrates two key points to be applied to the design of the defocus mechanism. First, the required force to defocus the membrane increased with membrane deflection, and correspondingly, with spring extension. The latching force available decreased with spring compression. This situation suggested that the defocus mechanism should exhibit a reversed spring constant: the least force should be required at full retraction, the greatest at full extension. Second, the fan was capable of providing the force required for retraction. Retraction even in severe rearward winds was possible by changing the elevation of the heliostat to reduce the dynamic pressure.

The final step in the definition of the parameters required for defocus design was to consider the stress induced in the membrane by the defocus mechanism. Figure 5.5 shows the peak membrane stress as a function of the total defocus force applied. The stress imposed by the passive defocus mechanism was within acceptable limits for the design force.

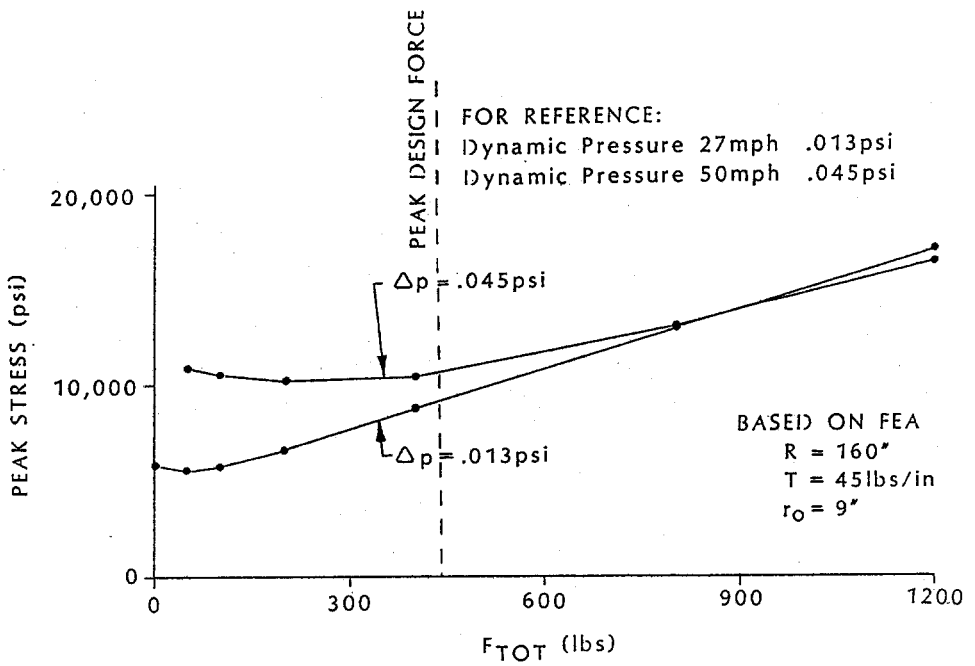

Figure 5.5 Peak Membrane Stress as a Function of the Defocus Force.

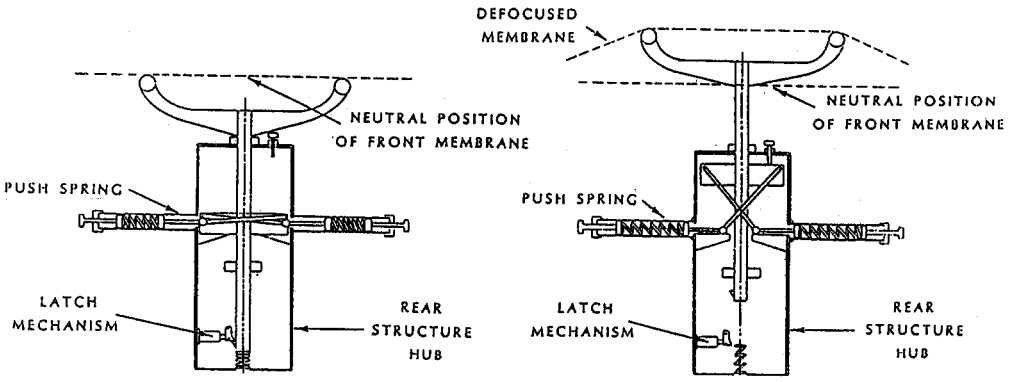

Figure 5.6 Schematic Representation of the Passive Defocus Mechanism.

The actual mechanism designed to accomplish defocus within the parameters dictated by the analysis is shown in Figure 5.6. A pair of orthogonally mounted compression springs connected to a compound linkage was used to apply force with a reversed spring constant. The springs were opposed to apply the greatest force at full extension; the minimum force was applied at retraction. The displacement was limited to 4 in. (102 mm) to keep membrane stress within acceptable limits at low or negative differential pressures. The defocus force was exerted on power loss to the latch solenoid; the latch was automatically engaged on retraction. A shock absorber was also attached to the push rod to reduce the speed of actuation and impact against the front membrane. The entire defocus mechanism slipped into the support assembly hub. All components were designed to be removed and replaced without major disassembly.

The defocus mechanism was slightly altered for implementation in the prototype. Adjustments were provided to control the preload on the compression springs. These adjustments allowed the retracted and extended force applied to the membrane to be varied. A set of capacitors was also added to the control system to allow a few seconds of fan power. This capacitor bank was provided to allow the fan to reverse and begin the defocus before the springs were released. Prototype testing should indicate whether this provision is necessary in the commercial design to achieve defocus in less than five seconds.

6.0 Membrane Attachment and Preload

The Mark I stretched-membrane heliostat relied upon a mechanical crimp and an inflated tube that applied the mirror-module preload after the membrane and ring frame were attached. The mechanical crimp was adequate to avoid membrane compression and buckling; approximately 25% of the initial tension was imposed by the ring deformation. The inflated tube provided the balance of the preload. Tube failure would not result in heliostat structural failure, but would reduce the optical performance of the heliostat in windy conditions. Tube failure was addressed in the heliostat cost through the selection of an appropriate, although expensive, material (silicone), combined with a relatively costly manufacturing process (single-piece, glass-reinforced, controlled-temperature cure). The inflated tube was still perceived as a reliability problem.

Elimination of the tension tube was a major objective in the Mark II design improvement. The majority of the effort was directed toward the selection and development of a method to achieve the initial membrane load with a non-consumable component. The development was not broken into subsections, but did follow a specific organization. First, the joint between the ring frame and membrane was reviewed to consider any advantages that might be gained with an alternate attachment procedure. Two basic methods of loading the membrane, thermal and mechanical strain, were subsequently considered to apply the initial tension. Resistance welding remained the preferred method of attachment between the ring and membrane, although the welds were made after the preload was applied. The tension tube was eliminated from the Mark II design. Mechanical strain, applied to the membrane only, was the tensioning method chosen for the commercial design.

The attachment between the ring frame and membrane was accomplished with resistance welds in the Mark I stretched-membrane mirror-module design. Discrete shear fasteners and continuous clamps were considered for the Mark II design, but no advantage in the application of preload was identified with alternate attachments. Fasteners and clamps were ultimately abandoned because of cost and fabrication problems.

Shear fasteners were initially considered for the membrane attachment. Approximately 10,000 fasteners were required based upon the limited bearing stress that could be applied to the thin membrane (0.010 in., 0.25 mm). The fastener holes reduced the effective area available to resist the tensile preload. There was also some concern over local distortion and instability in the membrane at the connection.

A doubler ring, welded to the membrane at the central manufacturing facility, was considered to reduce the number of fasteners and membrane distortion. The extra ring would have increased the shear area and provided limited bending resistance at the membrane perimeter. The doubler added a substantial amount of material to the heliostat without any significant structural benefit. The welding step was not eliminated, only shifted from the field to the central manufacturing facility. The additional cost of the doubler ring and fasteners did not justify the more conventional mechanical field attachment.

A continuous clamp was also considered for ring-to-membrane attachment. The clamp would have simplified the field assembly without the additional weld step at the manufacturing facility. The membrane would also have been replaceable. A clamp was designed with adequate frictional force to restrain the membrane. Because the required force was large, the thickness and size of the clamp were substantial. The cost for a clamped membrane was estimated at $2.50 per square meter of aperture. This cost was considered excessive compared to the resistance welding process. No specific advantage for the clamp in the preload process was established.

Resistance welding remained the preferred attachment procedure between the ring and membrane. This weld process required no consumables or additional material. The attachment was permanent. Direct resistance welding requires less process control and is more reliable than indirect processes [10]. The direct process did require access to both sides of the ring frame weld flange, however, for the opposed electrodes. The direct resistance weld was implemented in the design wherever possible.

The resistance welds used for ring frame and membrane attachment in the Mark I mirror module were completed prior to application of the initial tension. An objective in the Mark II design was to incorporate the tensioning into tooling rather than consumable components. The membrane preload would be applied prior to the resistance welded attachment. Consequently, resistance welds were made on membranes under tension. No difference in weld strength was associated with the initial state of the membrane during preliminary testing.

The first method considered for application of the initial tension was a differential temperature between the ring and membrane at assembly. The temperature difference required to apply an initial tension of 45 lbs/in. (7.9 kN/m) and compensate for ring shrinkage under load was 90 °F (50 °C). The thermal approach was divided into three basic approaches: a chilled ring and ambient membrane, heated membranes with an ambient ring, and some combination of the two approaches.

The force required to mechanically reduce the ring diameter sufficient to impose all of the membrane tension exceeded both the radial and normal buckling limit of the ring. The use of thermal strain in the ring was initially considered attractive because this ring shrinkage could be achieved without significant compressive stress. The temperature of a chilled ring, however, would have been substantially below the freezing point of water. The inevitable condensation and ice buildup on the ring would have interfered with the welding process.

The vacuum transfer platen was considered for membrane heating, but the platen would have had to cycle in temperature with each membrane. This additional thermal mass, combined with the large area available for heat loss to the air, would have increased the energy requirements and imposed a more severe time limitation for assembly than was desired. A heated clamp at the membrane perimeter was considered to reduce the thermal mass that was to be cycled. The edge clamp temperature differential would have had to be higher to compensate for the unaffected membrane area. This higher temperature (150 °F, 84 °C) approached the limit that could have been sustained by the reflective film. The clamp would also have had to sustain a very high tension without buckling or yielding. Load reaction would have increased the thermal mass of the edge clamp.

The use of thermal strain through ring chilling and membrane heating was also considered. Ring condensation would remain as a welding problem. The mass of the edge clamp was decreased. Ultimately, the thermal approach was simply abandoned because of the energy requirement and time limitations in the fabrication process. The maximum fabrication time allowed for any discrete mirror-module assembly procedure at the field manufacturing facility was less than twenty minutes [1]. This time limitation would have required rapid temperature changes and a significant amount of energy in the fabrication process.

The choices for application of mechanical strain fell into the same grouping: ring compression, membrane tension, or some combination of the two tooling loads. The operating compression of the ring substantially exceeded the buckling limit of the frame without the coupled membrane. Compression of the ring alone imposed even larger forces to provide adequate membrane tension. Controlled deflection of the ring in both the radial and normal directions was required to prevent buckling under the additional compression.

The membrane was not initially flat. A small initial tension was required to flatten the membrane as a preparation for welding. This weld requirement led to the consideration of an approach that compressed the ring and tensioned the membrane simultaneously. The objective in combined tooling design was to use the ring frame itself as the strong-back for membrane tension. Buckling was to be prevented by coupling the membrane and frame deformation during the preload process.

Previous experimentation with membrane tension clamps indicated that highly localized loads resulted in membrane failure at relatively low loads. A wider segmented clamp was considered to reduce this tearing failure. Analysis indicated that radial expansion of a segmented clamp resulted in excessive circumferential strain between clamp segments. In other words, circumferential strain did not occur under the clamp itself, but was forced to occur entirely between the clamps. This tensioning method caused circumferential membrane failure before an adequate preload was imposed.

An example of tooling design that was considered to alleviate the local failures at or between the clamps, while simultaneously compressing the ring, is shown in Figure 6.1. The clamp would have been displaced in the vertical direction to impose membrane tension. This vertical displacement would have imposed radial tension without a circumferential component at the clamp. Consequently, a segmented clamp could have been used without circumferential failure at the gaps. The radial component of the reaction at the tooling plate would then have simultaneously compressed the mirror-module ring frame. The membrane and ring would have been coupled to prevent buckling.

Analysis of this tooling configuration indicated that the compressive component of the load would not significantly compress the ring. Virtually all of the load would be applied as membrane tension. Alternate tooling designs had similar flaws, or suffered from excessive radial and normal area moments to prevent buckling and hence prevented compression, as well.

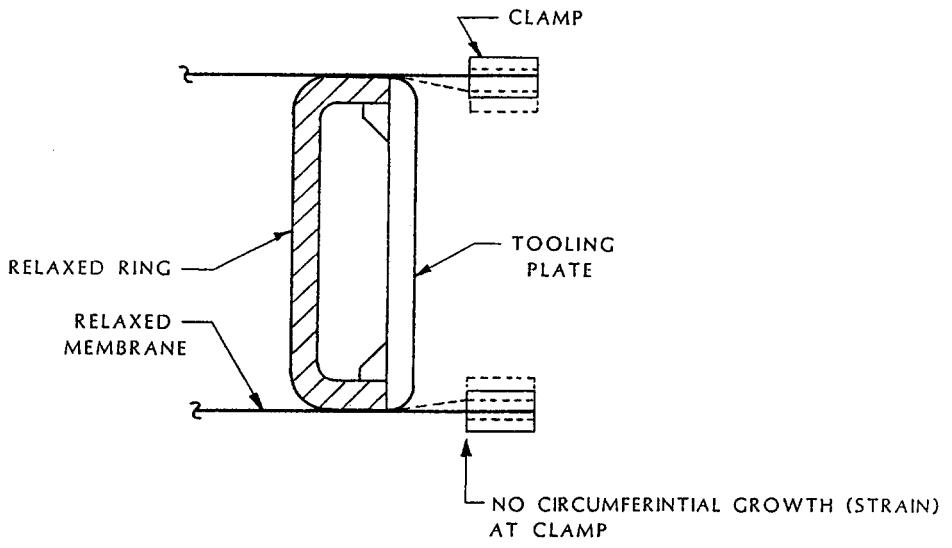

Figure 6.1 Preliminary Tooling Design for Simultaneous Ring Compression and Membrane Tension.

The final technique that was considered was application of the mechanical load to the membrane alone. This technique offered the advantages of flattening the membrane for welding without applying compressive buckling loads to the ring. The circumferential growth in the membrane was uniformly distributed by using a continuous, or continuous-acting, clamp. The area moment of the clamp in the radial direction was minimized to allow small changes in membrane diameter to be compensated with distortion of the clamp. Access to both sides of the membrane welding flange was provided in this design to allow direct resistance welding as shown in Figure 6.2. The strong-back was provided in an entirely separate tooling ring.

A double-acting clamp was selected to allow easy insertion and withdrawal of the membrane. A linkage extended the clamps to grip the membrane during tensioning. Retraction was possible because the wedge clamps were discrete. The friction between the wedge and continuous ring required circumferential growth along the edge, rather than between the clamps. Consequently, excessive strain between the discrete clamps did not occur. The use of tooling, such as that shown in Figure 6.2, eliminated components from the mirror module by transferring their function from the mirror module to the tooling.

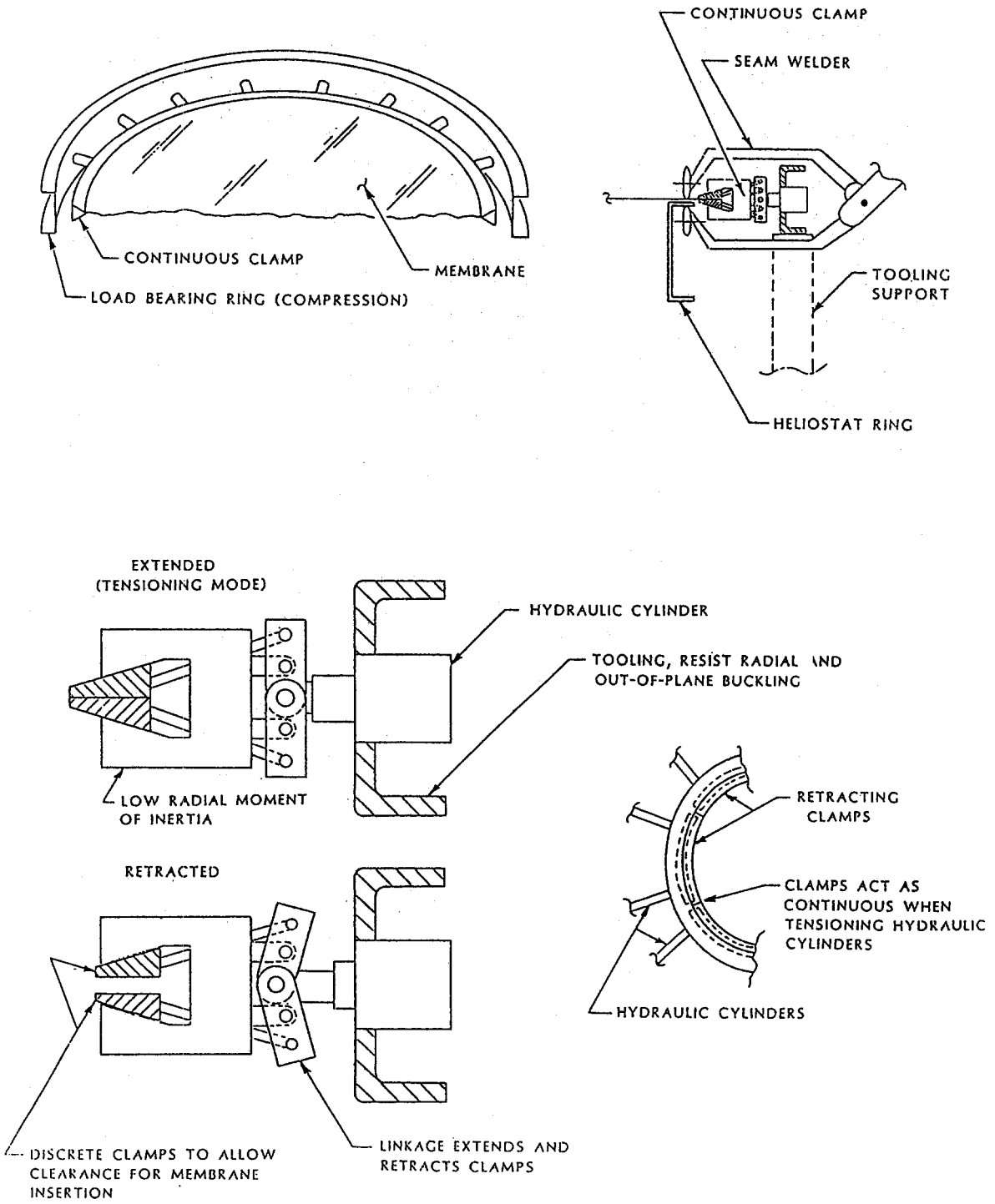

Figure 6.2 Final Tooling Design for Application of All Preload to the Membrane.

7.0 Costs for the Improved Commercial Design

The design of the commercial Mark I stretched-membrane heliostat provided the baseline for analysis of improvements to the mirror module considered under this contract. The objective was to improve performance while reducing cost. Five major design changes were investigated. The associated cost reductions are presented in this section. The mirror-module cost was reduced by approximately 8%; a net difference of $2.31 per square meter of aperture in 1985 dollars. Performance improvements were demonstrated by the prototype discussed in the following sections.

Table 7.1
Direct Material Cost Comparison

Description	Cost, 1985 Dollars per Heliostat Mark II	Mark I	Difference
Membrane	380.14	380.14	0.00
Film	475.31	475.31	0.00
Ring	418.50	403.20	+15.11
Ring/MembraneDoublers	64.80	54.00	+10.80
Cantilever Truss	372.00	453.42	-81.42
Strapping	59.40	59.40	0.00
Hub and Brackets	48.00	177.75	-129.75
Drive Brackets	26.25	26.25	0.00
Hinge Assembly	36.00	51.80	-15.80
Tension Tube	0.00	73.60	-73.60
Paint	9.00	9.00	0.00
Misc. Hardware, Brackets	30.00	30.00	0.00
Subtotal	1919.40	2193.87	-274.66
Controls	285.00	250.00	+ 35.00
Total $/Heliostat	2204.40	2443.87	-239.66
Total $/m^2	14.69	16.29	

7.1 Cost Reduction

The design improvements and associated cost reductions for the stretched-membrane heliostat were based upon the net change in cost from the baseline design presented in an earlier report [1]. All costs were developed with identical assumptions outlined in the previous report and 1985 dollars. This approach allowed direct comparison between the two designs. Several key assumptions were made for both cost developments. The cost of the reflective film was projected to be, assuming multiple suppliers, $0.30/ft^2 (current costs are approximately $2.00/ft^2). Membrane material cost was $0.83/lb, and ring material cost was $0.90/lb. (See [1] for development of these costs.)

The design improvements and cost reductions were limited by contract to analysis of the mirror module only. Drives, pedestals, foundations, field wiring, and installation of those components that were not a direct part of the reflector assembly or support structure were classified as "Balance of Heliostat" (BOH) components. The assumed production rate remained the same for both developments (50,000 units per year).

The direct material cost comparison is provided in Table 7.1. The increase in ring cost was associated with the identification of additional failure modes that were identified in the frame structural analysis and were not investigated in the previous contract. The decrease in truss cost was primarily associated with the change in material. Cold-rolled sheet was used for the Mark I fabricated, primary and secondary members; hot-rolled material was substituted for these truss elements in the more conventional Warren truss design used in the Mark II mirror-module. Hot-rolled steel is approximately 35% less costly than cold rolled. Vendor quotes of $0.21/lb were used. The truss reductions also reflect the change in coefficients used to establish the nonuniform loads. The hub was substantially simplified in the improved design. A large-diameter trussed hub was identified in the Mark I design; this component was reduced to a short section of pipe in the current design. This change also reduced the number and complexity of drive brackets. The tension tube was eliminated from the design entirely.

Control increases associated with the additional passive defocus mechanism were separated. This cost increase represented the addition of a new operational feature to the stretched-membrane heliostat: defocus on power failure.

Table 7.2
Change in Equipment Cost

Description	Cost Difference (Thousands of Dollars)	
Central Manufacturing Facility		
Membrane	None	
Truss	-1010	
Hub	- 500	
Tube	-1994	
General Plant Equipment	None	
CMF Subtotal		-3504
Site Manufacturing Facility		
Ring Fabrication	- 210	
Ring/Membrane Attachment	+ 50	
Hub Placement	None	
Final Assembly	None	
General	None	
Installation	None	
SMF Subtotal	- 160/site @ 9 sites	-1440
Total change in equipment cost		-4944

Equipment cost changes are shown in Table 7.2; labor changes are summarized in Table 7.3. The simplification of the rear structure, combined with the elimination of the tension tube, accounted for the majority of the central manufacturing facility (CMF) cost reduction.

Table 7.3
Change in Labor Time

Description	Labor Difference (Minutes per Heliostat)	
Central Manufacturing Facility		
Membrane	None	
Truss	+0.5	
Hub	-1.5	
Tube	-2.0	
Hinge	-0.2	
Control	+0.5	
Straps	None	
CMF Subtotal		-2.7
Site Manufacturing Facility		None
Total Labor Change		-2.7

Table 7.4
Cost by Components of Required Revenue

Description	Cost, Dollars per square meter Mark II	Mark I	Difference
Direct Material	14.69	16.29	-1.60
Direct Labor	1.24	1.28	-0.04
Consumables	1.04	1.12	-0.08
Indirects	1.05	1.09	-0.04
G&A	2.16	2.37	-0.21
Capital Replacement and Capitalization	2.05	2.11	-0.06
Property Tax and Insurance	0.08	0.09	-0.01
Other	1.20	1.32	-0.12
Transportation	1.00	1.00	0.00
Gross Profit	1.48	1.63	-0.15
Mirror-Module Total	25.99	28.30	- 2.31

The reduction at the site manufacturing facility was the result of using the open section ring. One roll-and-slit operation was eliminated, along with the welding step required to fabricate a closed section. The additional equipment for the central restraint was included in the ring-to-membrane attachment category.

The cost by components of required revenue for the design improvements is shown in Table 7.4. All mirror-module costs not summarized in previous tables were calculated based upon a percentage of direct material, capital cost, labor cost, or some combination of these three costs. The assumptions for these components were outlined in a previous report [1].

The cost for the BOH was not affected by the mirror-module design. Previous work was used to define its cost. Development of the low-cost heliostat drive has shown that a drive cost of $\$14.05/m^2$ (adjusted per CPI to 1985 dollars) is reasonable [12]. This represents a $\$3.05/m^2$ increase in drive cost over that used for the Mark I study. Other BOH cost components were taken directly from the SKI report [1]. The resulting BOH cost was $\$30.01/m^2$. This increase in BOH cost, which is independent of mirror module cost, essentially offset the cost improvements of the mirror module. The total installed cost for the improved heliostat was $\$56.00/m^2$.

No attempt was made to predict cost in current dollars. Applying one arbitrary inflation figure to these 1985 values would not give completely accurate values for current costs. Sources of cost have been affected differently by inflation. For instance, the price of aluminum sheet has increased 26 percent, while the price of steel has increased only 10 percent. This is based on the Producer's Price Index from August 1985 to December 1988. The Consumer Price Index rose 12 percent during the same period. For reference, the direct material costs such as aluminum, steel, film, controls, and hardware represent 56 percent of the installed cost.

8.0 Introduction to Prototype

Sections 8 through 12 document the initial process testing and prototype construction. The prototype is 27 feet in diameter with an active area of 530 sq. ft. after the fan cover, seams, and unlaminated outside edge are deducted. Total weight of the mirror module, trusses, and hub is 2200 pounds. Focus control is supplied by a small, standard industrial programmable logic controller. A passive defocus mechanism is included, which can be activated both by active control and automatically upon loss of power. Complete prototype specifications are shown in Table 8.1. The prototype is as representative as possible of the commercial design. A discussion of specific differences between the prototype and the commercial design and related issues of scale-up are located in Section 11.0.

The prototype design included only the mirror module itself and not the drive or pylon to which it was mounted. An existing pylon at Sandia National Laboratories at Albuquerque's (SNLA) Central Receiver Test Facility (CRTF) and a pre-owned (Winsmith) torque tube drive were utilized. The prototype heliostat design was not varied from that of the commercial design to utilize this drive. Rather an adapter weldment was used to interface the heliostat to the torque tube drive. This adapter is shown in Figure 8.1.

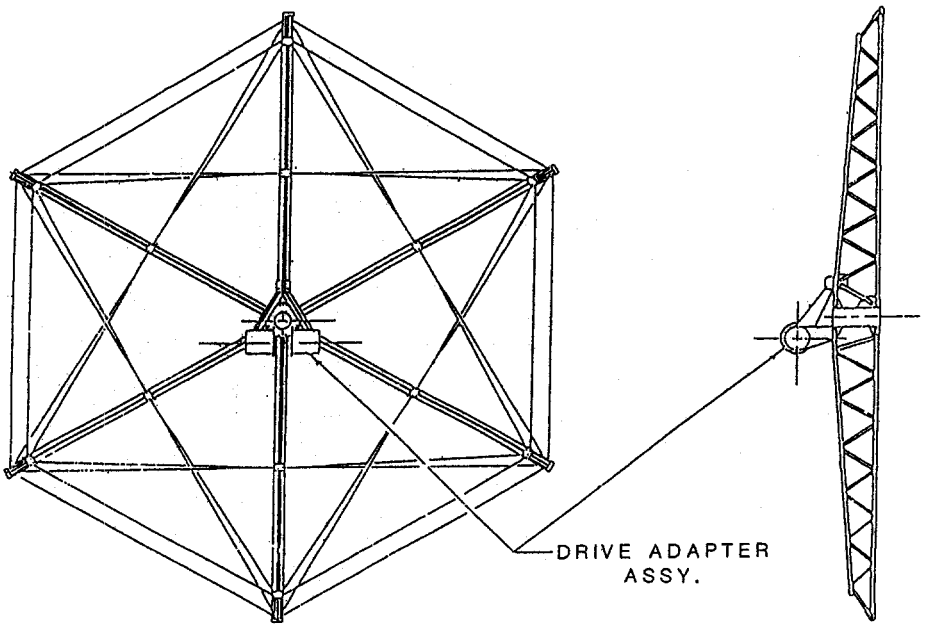

Figure 8.1 Rear Structure and Drive Adapter of the Prototype Heliostat.

Many tests were performed on the material, welds, and membrane tensioning techniques used on the prototype. These tests were made to determine the required membrane material properties, optimum welding procedures, and suitable tensioning techniques to be used for mirror module fabrication. Methods and results of these tests were qualitative in some cases and quantitative in others.

After prototype design and initial material and weld testing were completed, the heliostat fabrication was initiated. As many components as possible were prefabricated at SKI's facility in Dallas to minimize field expenses. All tooling components were prefabricated and most assembly operations were implemented experimentally in Dallas before field operations were begun.

Two membrane tensioning techniques were implemented at the full prototype scale. Four tension measuring systems were implemented at full-scale. After the tension tooling was erected at SNLA, some difficulties were encountered in successfully tensioning the membranes. Two membrane failures and an insufficiently tensioned final mirror-module assembly led to further improvements in membrane fabrication and assembly techniques and refinements to the tension measuring methods. After these improvements were implemented, the entire front membrane was replaced, and a successful heliostat was erected at the CRTF.

Preliminary measurements by Sandia indicated a beam dispersion error of 1.3 mr mirror-normal in calm wind. Active control in windy conditions is satisfactory and within Sandia's heliostat specification of 3.6 mr.

TABLE 8.1
PROTOTYPE HELIOSTAT SPECIFICATIONS

Heliostat diameter	324 in.	8.2 m
Total area	573 sq. ft.	53.2 m^2
Effective area	530 sq. ft.	49.2 m^2
Membrane		
Material	5052-H34 Aluminum	
Thickness	.010 in.	.25 mm
Panel width	36 in.	91.4 cm
Reflective material	ECP-300A by 3M Co.	
Reflective film width	24 in.	61 cm
Front membrane hole	17 in.	43.2 cm
Rear membrane hole	44 in.	111.8 cm
Weight	87 lbs ea.	39.5 kg ea.
Ring		
Material	6061-T6 Aluminum	
Shape	6 in. x 1.92 in. Am. Std. channel	
3 #/ft.	4.5 kg/m	
Cross sectional area	2.403 sq. in.	15.5 cm^2
In-plane area moment	0.72 $in.^4$	30 cm^4
Out-of-plane area moment	13.0 $in.^4$	541.1 cm^4
Weight	251 lbs	113.9 kg
Reinforcing elements		
Shape	1.5 x 2 x .25 Am. Std. angle	
Material	6061-T6 Aluminum	
Position	Rolled 1.5 in. leg in	
Qty.	2	
Weight	84 lbs ea.	38.1 kg ea.
Trusses		
Quantity	6	
Primary material	ASTM A36 Steel	
Secondary material	ASTM A36 Steel	
Height	24 in. at root	61 cm
	13 in. at tip	33 cm
Weight	205 lbs ea.	93 kg ea.
Hub		
Body material	AISI type 1026 steel	
	12 in. schd. 40 pipe	30.5 cm
Flanges	3/8 in. ASTM A36 steel	1 cm
Diameter	24 in.	61 cm
Weight of hub assembly	126 lbs	57.2 kg
Controls		
Fan motor	1/4hp 90VDC PM	.2 kw
Fan diameter	14 in.	35.6 cm
Position sensor	2 in. stroke LVDT	5.1 cm
Logic controller	Siemans S5-102 U	
Filter	pleated paper	

9.0 Testing

Physical testing of materials and processes planned for use in the prototype was performed to verify feasibility of critical items. These tests are also applicable to the commercial design. Standard material and weld testing was conducted on test coupons. Full-scale testing was conducted to evaluate membrane tensioning techniques and tension measuring methods.

9.1 Material Processing

The production plan for the commercial heliostat included stretcher leveling of the coil stock prior to laminating and membrane fabrication. Only standard as-rolled coil stock was used in the first prototype heliostat. Experience in fabricating the unit, shown in Figure 9.1, suggested that inconsistencies in the coil stock were producing areas in the final membrane that were unevenly tensioned. It appeared that the coil stock had waves in it so that there was excess material along the center of the panels compared to the edge length, as shown in Figure 9.2.

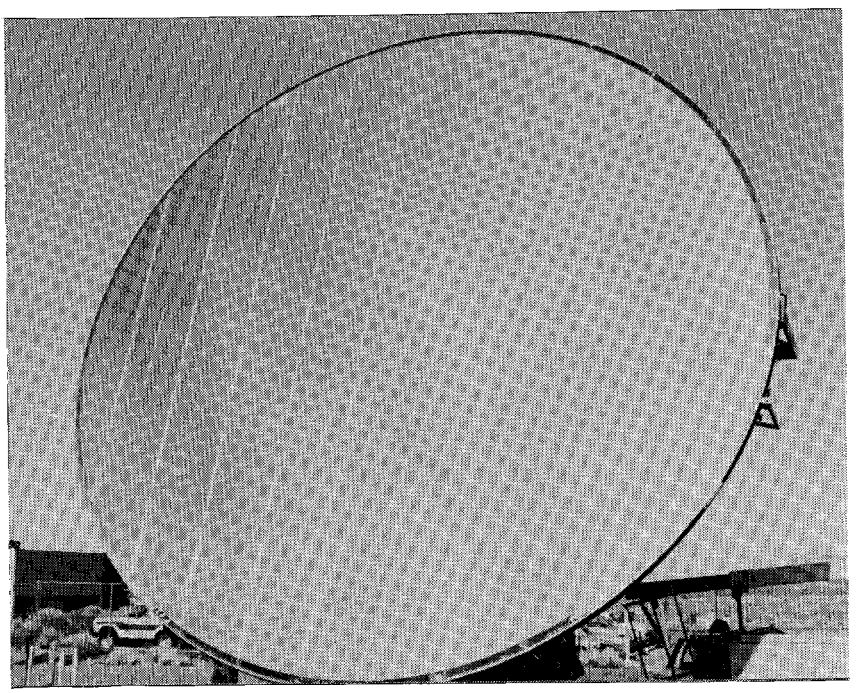

Figure 9.1 Mark I Heliostat Prototype. Areas of uneven membrane tension are visible on left side.

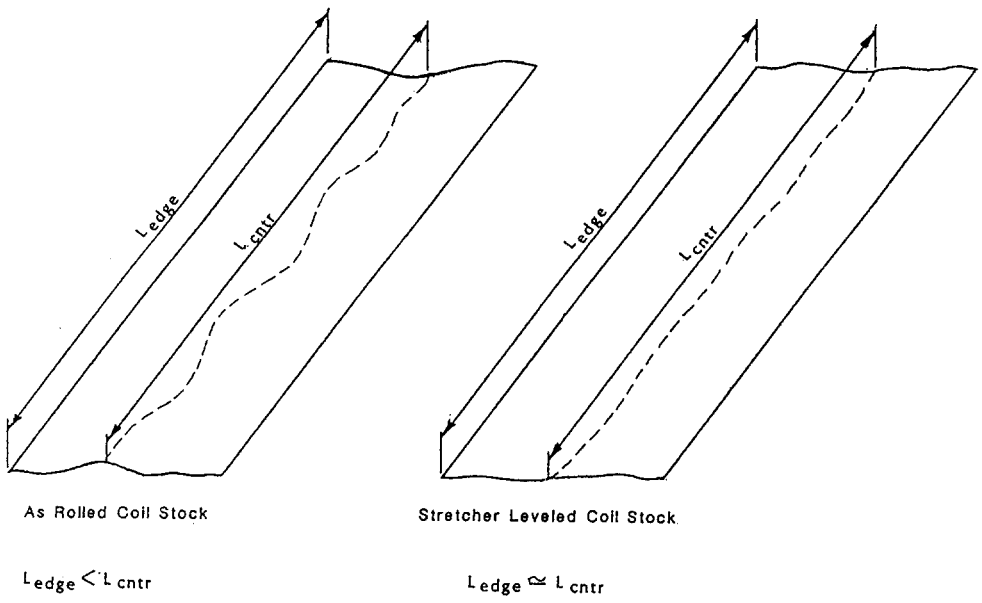

Figure 9.2 Effects of Leveling on Coil Stock.

Material for the second prototype was ordered that had been stretcher leveled. The specification given to the rolling mill was a table of values showing maximum wave height for a series of different wave periods, as shown in Appendix A.

No leveling specification existed for the first prototype coil stock. Direct comparison of material from the first and second prototype coil stock clearly showed that the leveled material was significantly flatter.

While comparing long strips of coil stock (30 ft.) rolled out on a very flat surface, it was apparent that some camber existed in the material, also. That is the material was not straight within the plane of the sheet. The manner in which coil stock was overlapped and welded to form the membranes must allow for this camber. Since the welder travels in a straight line, a variable weld seam-to-edge distance may occur, as shown in Figure 9.3.

In fabricating membranes for the second Mark II mirror-module assembly, particular attention was paid to allowing the strips of coil stock to lie in their natural shape during fit-up. This avoids locking stress into some areas of the completed membrane's panels, which would cause the final membrane shape not to be flat. The welding table hold-down vacuum was activated in zones, starting at the strip center, to avoid straining the coil stock prior to welding.

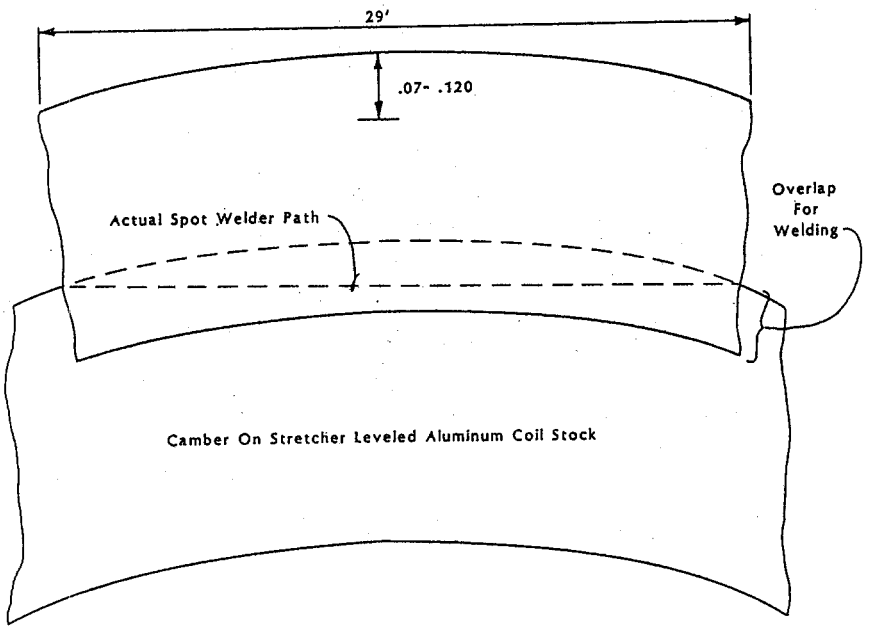

Figure 9.3 Effects of Coil Stock Camber on Membrane Fabricating.

Laminated Membrane Properties

After the aluminum is laminated with the acrylic reflective film there is an interaction between the film and the metal. Because the materials have dissimilar coefficients of thermal and hygroscopic expansion, stresses can develop in the membrane that affect its natural shape.

Strip coupons of laminated aluminum were exposed to varying environments to explore this relationship. These tests were only qualitative but showed that the tendency of the acrylic to shrink at low humidities could cause a change in a 6 in. x 1 in. strip of laminated 0.010 in. thick aluminum. An 18 in. diameter disk of laminated aluminum showed no visible change under the same environmental changes. In high humidity conditions the expansion of the acrylic would cause it to go into a compressive stress state. However, no observable changes occurred in the strip tests or disk tests. Variations in temperature of +/- 35 °F showed no changes.

The potential apparently exists for a laminated membrane to change shape when going from a moist state of equilibrium to a dry one. This could affect the fit up of the membrane to the tensioning tooling. Use of a vacuum layout table would eliminate this concern.

9.2 Weld Testing

Weld testing was performed in three areas:

1. Steel weld qualifying for rear structure fabrication,
2. Aluminum weld qualifying for heliostat ring fabrication,
3. Aluminum coil stock welding for membrane manufacture, and aluminum coil stock to structural shape welding for heliostat assembly.

The purpose of the weld testing was to verify correct welding procedures, to assure sound assembly, and to check weld process control during fabrication to assure the integrity of the final heliostat.

Structural Weld Qualifying

Steel weld testing and welder qualification were performed per requirements of the AWS Structural Welding Code for Steel ANSI/AWS D1.1-86, Sections 5.15-5.31. This applied to all welding on the truss assemblies, drive adapters, and central hub.

Aluminum weld testing and welder qualification were performed per requirements of the AWS Structural Welding Code for Aluminum ANSI/AWS D1.2-83, Sections 5.13-5.27. This applied to welding the four sections of extruded channel to form the heliostat ring.

Membrane Welding

Membranes for the prototype were fabricated from strips of coil stock welded to one another with overlapping edges. The process used was rolling spot electrical resistance welding. The membrane panels were laid out on a long (30 ft.) vacuum hold-down table. Membrane panels were positioned prior to vacuum clamping and welding to achieve the proper edge overlap. The welding machine traveled along the table with two arms reaching around the table to hold the rolling welding wheels against the coil stock.

Structural integrity of the fabricated membranes was a critical element to successful completion of the prototype. All significant welding parameters were identified and optimized as much as practical by performing a matrix of test welds with varying parameters and performing tensile pull tests on the coupons. The welding parameters controlled include:

1. Weld current
   a. transformer tap
   b. % current on controller
   c. squeeze pressure
   e. electrode configuration
   f. surface preparation

2. Weld time
   a. cycles of weld current

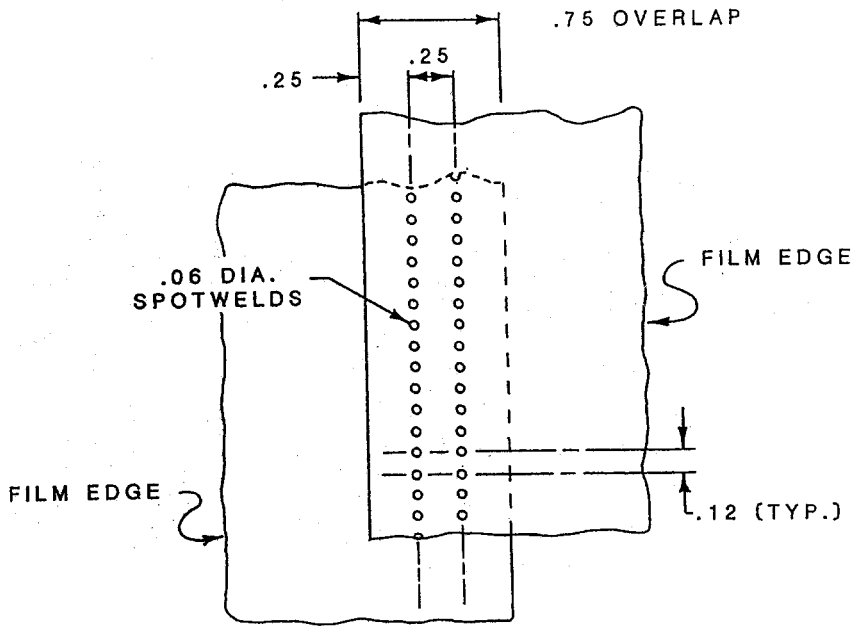

Figure 9.4 Detail of Membrane Weld Seam.

3. Cool time
   a. travel speed
   b. electrode configuration

4. Weld joint design
   a. rolling spot weld configuration
   b. row-to-row spacing

One major welding parameter was the joint design itself, including overlap dimension, rolling spot weld spacing and number of rows, and their spacing. The seam configuration used for the Mark II prototype uses a double row weld seam as shown in Figure 9.4. On the Mark I prototype only one row of spot welds was required. Comparison testing showed significantly higher strength with the double row seam. Because of the high membrane tooling tension used during mirror-module assembly for the Mark II, the higher strength seam was selected. This would also be used for the commercial design where all final membrane tension is provided by pretensioning during assembly with no ring compression.

In addition to the initial testing to establish optimum welding parameters, test coupons were cut from the beginning and end of each actual weld seam on the membranes during fabrication. Results from tensile testing these samples provided data for controlling the quality of the completed membranes. Due to errors in cutting, there were a few seams that were not monitored in this manner. This omission could have allowed the one membrane failure experienced due to weld quality. Tensile test coupons with no weld seam in them generally failed at 32,800 psi. Weld seams generally failed at 30,500 psi. The minimum allowable weld seam stress chosen was 28,000 psi because it was equivalent to two times the tooling tension stress.

Membrane-to-Heliostat Ring Welding

Welding the 0.010-in. membrane to the approximately 0.25-in. heliostat ring presented a special challenge. Correct welding parameters had to be found empirically as the handbooks did not extend to this range. The task was further complicated by the presence of the tooling ring, which the jaws of the welder had to reach around. This large steel element in the secondary area of the welder's high-current circuit absorbed energy, influencing the welder settings. All weld qualifying had to wait until all tooling was in place. In Figure 9.5, a custom tensile tester was built to pull-test actual membrane material welded to a section of the heliostat ring while it was fixtured in the tooling. Once all welding parameters were controlled, the welding process was demonstrated to be reliable and repeatable.

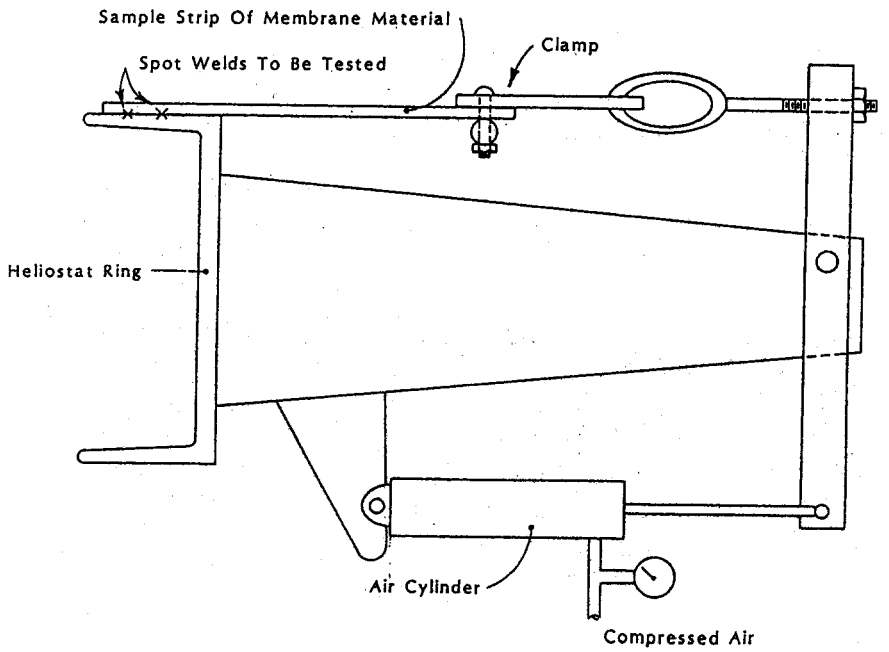

Figure 9.5 Apparatus to Test Membrane-to-Heliostat Ring Weld.

9.3 Method of Membrane Tensioning

The membranes had to be tensioned to a level greater than the required final tension, as described in Section 6. The final membrane tensioning technique described in Section 6 is intended for use on commercial scale heliostat production. To implement this specialized tooling for a single prototype was prohibitively expensive. A lower cost membrane tensioning technique was developed that would permit membrane-to-ring welding to be done under the same conditions as proposed for commercial assembly operations. No compression of the ring was provided. The membranes were welded to the ring while under a high pretension. Membrane tension was then transferred to the ring by reducing the tension imposed by the tooling on the outer edge of the membranes.

Two tension tooling rings were utilized as reaction rings to separately tension the front and rear membranes. Two variations of a tensioning concept were tried, both using a pneumatically inflatable bladder to supply the tensioning force.

The first technique implemented used the bladder on the outside diameter of the reaction ring. The outer edge of the membrane was wrapped around the bladder and fixtured to the ring with epoxy adhesive. To do this, the outer edge of the membrane was slit to form multiple tabs to ease the lay of the material when it wrapped around the curved takeoff bar and deflated bladder, as shown in Figure 9.6.

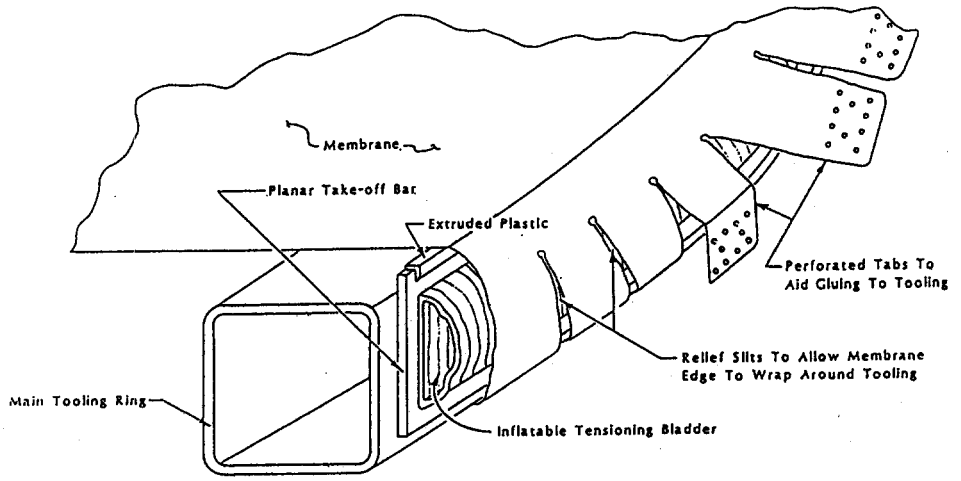

Figure 9.6 Membrane Tensioning Technique Using Bladder on Outside Circumference of Tooling Ring.

The second technique used the bladder on the surface of the ring, as shown in Figure 9.7. A clamp bar was added to the outside diameter of the ring to fixture the membrane edge to the tooling. As the bladder was inflated, an out-of-plane force was exerted on the membrane that was translated to tension by the geometry of the membrane and reaction ring.

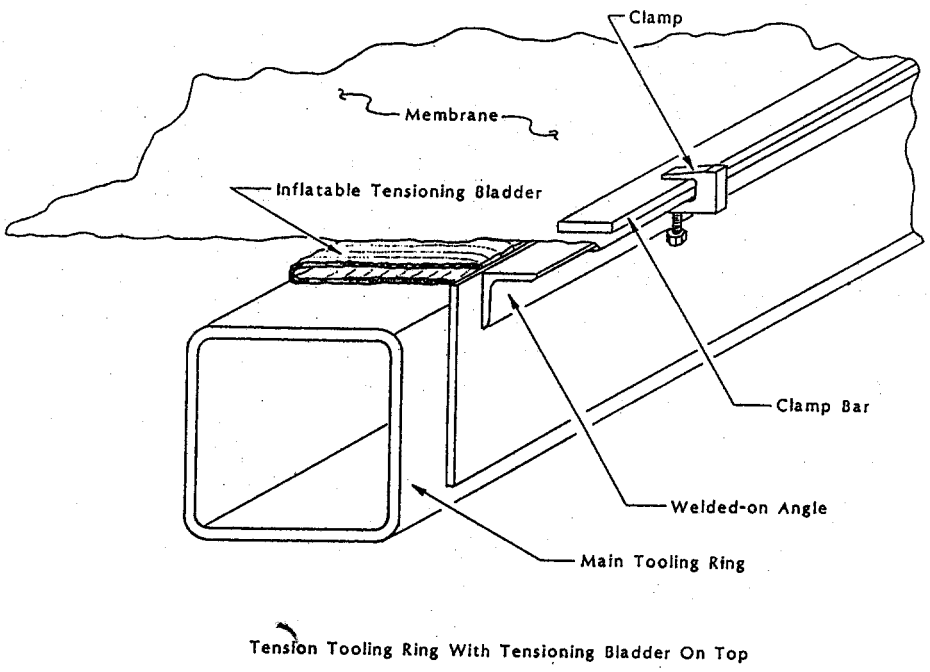

Figure 9.7 Membrane Tensioning Technique Using Bladder on Top Surface of Tooling Ring.

The first technique, although straightforward in theory, had problems resulting from many stress risers and concentrations in the individual tabs around the membrane periphery. Getting a sufficiently even fit-up between the individual tabs and the ring and getting even slack removal on all diameters of the membrane proved impractical, as shown in Figures 9.8 and 9.9. If a failure occurred in a single tab, as shown in Figure 9.10, the bladder would tend to extend out through the space where a tab no longer restrained it. This bulge in the bladder would, in turn, put a tearing moment on the adjacent tabs. This failure mode was exacerbated by the small ductility range of 5052-H34 aluminum. This led to sudden tear propagation and membrane failure.

Figure 9.8 Effects of Unequal "Slack" in Membrane After Fit Up to Tooling

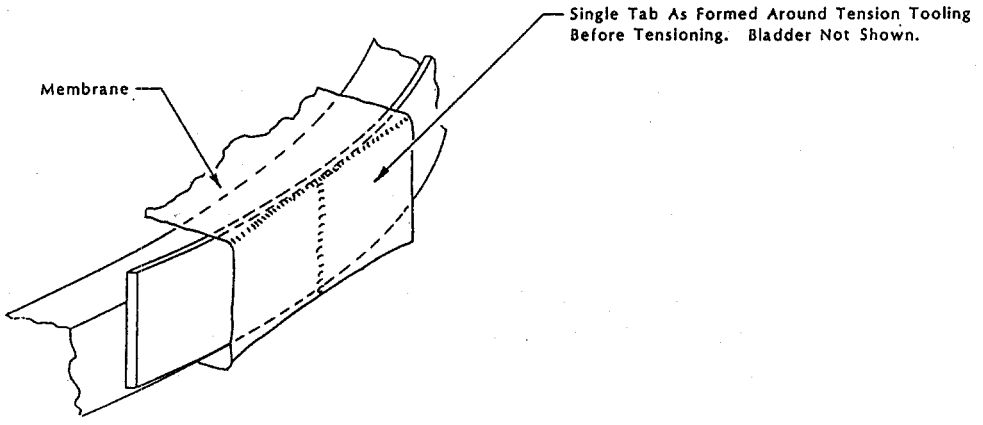

Figure 9.9 Effect of Membrane Tabs Wrapping Around Circumference of Tooling Ring. NOTE: The tab cannot bend in a compound curve so there is an uneven fit between the tab and the bladder.

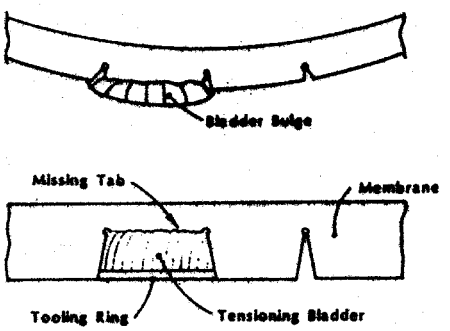

Figure 9.10 Effect of a Failed Membrane Tab During Tensioning. NOTE: The bladder bulges where the tab has failed and imposes a tearing force on the adjacent tabs.

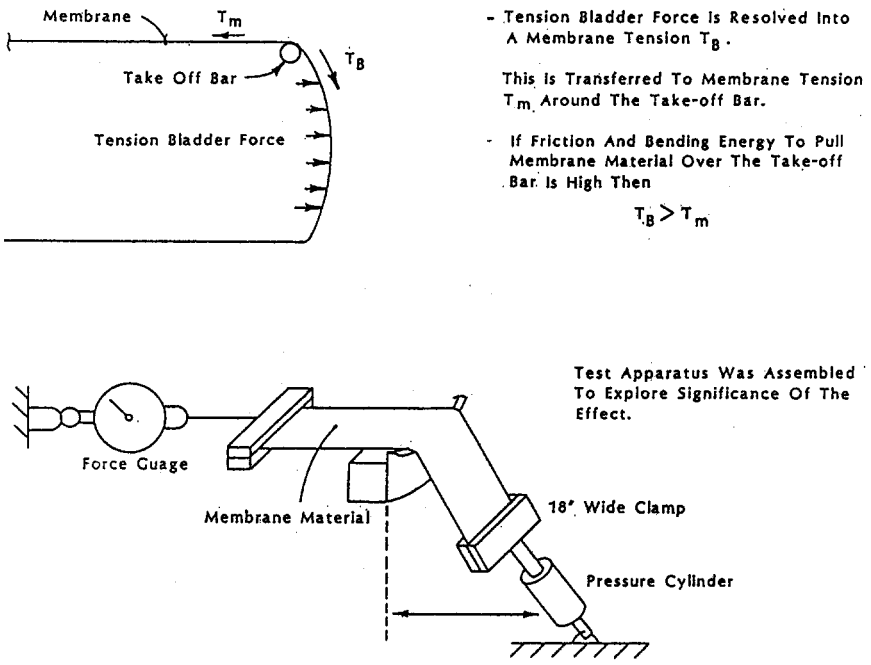

Figure 9.11 Apparatus to Investigate the Effect of Friction Where the Membrane is Drawn Over the Tooling Take-Off Bar.

The friction of the membrane as it was pulled over the take-off bar was tested to determine if it could cause significantly higher tension in the tab than in the plane of the membrane. A fixture shown in Figure 9.11 was built to test this theory for an 18-in. wide strip. The results indicated an 18% tension difference. This increase by itself was not a major problem, but it further increased the sensitivity of the tabs to failure initiation, which could then propagate.

The selected tensioning method utilized the bladder on the face of the ring (Figure 9.7). The clamping method proved reliable and well suited to prototypical operations.

One shortcoming of this method was identified. When the bladder was inflated, it expanded axially. If the membrane, as fixtured to the tension tooling ring, had more slack material along one diameter than another, the bladder would expand further at some points. This would cause the surface of the membrane to become slightly saddle-shaped rather than staying completely planar, as shown in Figure 9.12. The better the original flatness of the fabricated membrane is controlled and the more evenly it is fitted to the tooling ring, the less effect this uneven bladder displacement will have.

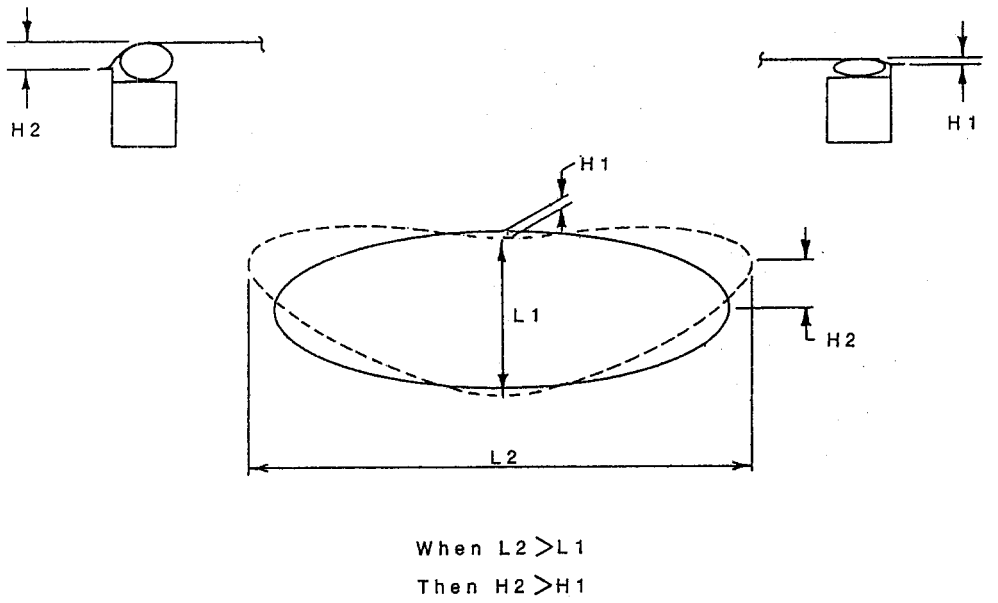

Figure 9.12 Effects of Uneven Membrane Fit on Membrane Planarity. NOTE: This is applicable to the bladder-on-top-of-tooling ring tensioning technique.

With the improvements made to the membrane fabricating and membrane layout techniques, this was not a significant problem for prototype fabrication. The commercial production plan uses a different tensioning technique, which will not have this sensitivity at all.

9.4 Techniques of Membrane Tension Measuring

The tension level in the membrane must be accurately determined to assemble reproducible, high quality mirror modules. A heliostat's operating performance is a function of final membrane tension. Therefore, the tooling tension must be known in order to insure proper tension in the final assembled membrane. The former must also be known to prevent overstressing the membrane during assembly.

Several methods for measuring membrane tension were evaluated. These were

1. Bladder pressure,
2. Direct membrane strain as an indicator of tension, and
3. Membrane center deflection
   a. unweighted
   b. weighted.

Bladder pressure, when the bladder is on top of the tension tooling ring, is not an adequate indicator of membrane tension. The bladder expands axially until its force is balanced by the tension in the membrane. If the membrane, as discussed in the previous section, has varying slack in it, or if it is fitted with different slack than a previous membrane, it will expand differently at different locations for the same bladder pressure. The out-of-plane force from the bladder is resolved into membrane tension by the displacement out-of-plane of the membrane. The geometry is such that a small change in displacement causes a large change in tension. Therefore, if some unknown geometry change is a result of fit-up variations, there is a large unquantified effect on the bladder pressure/tension relationship.

As the membrane is tensioned, the material strains. A direct linear measurement of this strain could indicate the actual tension because of the following relationship:

stress = strain x modulus/(1 - Poisson's ratio).

The use of this technique requires an accurate measurement both of the original length of the membrane material and the change in length so that the strain factor can be known. For the 140 lb/in. tooling tension used and 310 in. membrane diameter, the change in length measured was about 0.3 in.

Because a tape was used to make the measurements, there was concern about how repeatable and accurate the measurements were. A test apparatus described in Figure 9.13 was used to compare predicted tensions to actual measured tension in a uniaxial strip. Results indicate this technique is both accurate and repeatable for measuring strain along a diameter. This method of tension indication was the primary one used for the first complete mirror-module assembly.

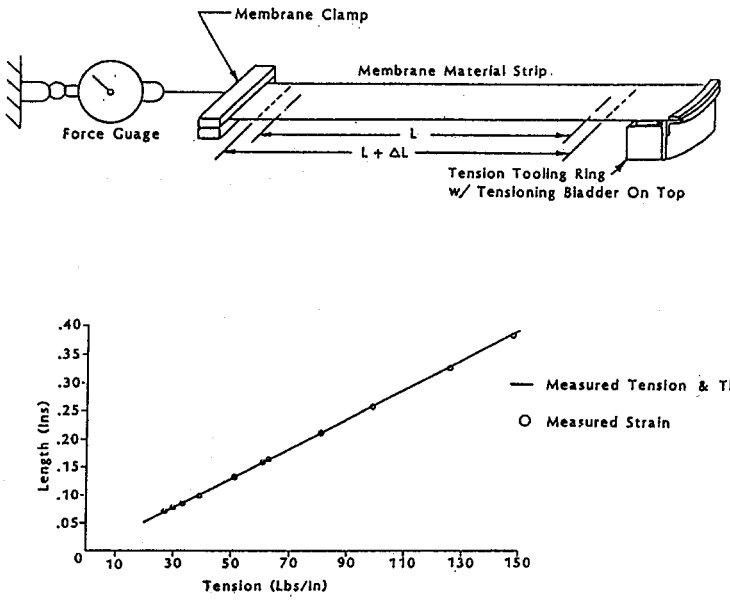

Figure 9.13 Apparatus for Testing Use of Direct Strain Measurement as Indicator of Membrane Tension.

Problems with failed membranes, both during tensioning and from insufficient final tension during the first mirror-module assembly, led to concerns about the adequacy of measured strain along one diameter being representative of average membrane strain. Measurements taken on multiple diameters and on several chords showed variations in indicated tension of +/-12 lbs/in. This variation was constant with increasing tension, not a percentage error. The source of this difference was probably membrane slack. The slack could have been in the raw material, the membrane as fabricated, or a result of imperfect fit up to the tooling.

Other methods of indicating tension were explored based upon analytical predictions assuming linearity. The displacement of the center of the tensioned membrane, when acted upon by a uniform pressure, or by a discrete center force, was used as an indicator of tension. The relationship between membrane tension, diameter, center displacement, and applied force has been described by M. Murphy for uniform pressure situations [5]. This relationship is

$$\text{deflection} = (\text{pressure} \times \text{radius}^2) / (4 \times \text{tension}).$$

For a 320 in. diameter membrane under a uniform pressure load of only the weight of the membrane material itself, the change in center deflections was too small to be reliably measured. When tension was increased from 130 lbs/in. to the tooling tension of 140 lbs/in., the displacement would reduce by 0.003 in. This change in deflection was less than the variations in displacement resulting from minor room air currents and natural oscillations in the membrane.

If an additional force is applied as a disk load at the center of the membrane, the displacement is increased, all other factor remaining the same. This relationship has also been described by Murphy in an unpublished memo as:

$$\text{deflection} = (\text{force} / (\text{tension} \times \text{pi} \times 2)) \times \ln(\text{membrane radius} / \text{disk radius}).$$

With a weight of 100 lbs applied by a 16 in. diameter disk at the tooling tension level, changes in displacement are amplified to 0.026 in. for an increase in membrane tension from 130 to 140 lbs/in. This magnitude of change can be reliably measured. The technique also gives a better indication of average membrane tension than single diametrical strain measurements. Uncertainty of measurements made by the center deflection method were +/-4 lbs/in., which was better than the 12 lbs/in. for the strain method. Lower deflections showed less uncertainty, consistent with subsequent FEA modeling described below. This membrane deflection, with weighted center tension indicating method, was used during assembly of the successful final mirror module.

After the hardware was completed, some additional analysis was done to confirm that the assumption of linearity made in the analytical predictions of membrane displacements was appropriate in the small displacement range used for these measurements. A non-linear, finite element analysis was made using NASTRAN software with assistance from SERI and Dan Sallis of Dan-Ka Products. The linear model consistently predicted greater tensions than the FEA; however, this difference was only significant for large deflections. Results shown in Figure 9.14 indicate there is good correlation for the small displacements (>1 in.) used for these measurements. It should be noted

that Figure 9.14 is for a heliostat radius of 276 in. The divergence would be somewhat greater for a radius of 160 in.

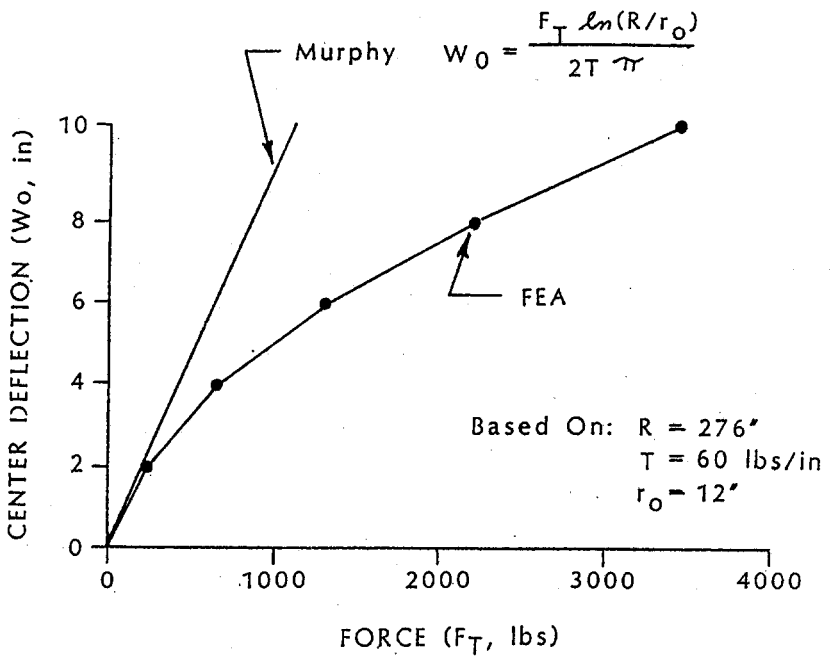

Figure 9.14 Comparison of Non-Linear FEA Model to Linear Mathematical Model for Relating Membrane Deflection to Applied Center Force.

10.0 Fabrication of the Prototype

10.1 Work Plan

Prototype fabrication involved all component fabrication as well as tooling fabrication and testing, followed by mirror-module assembly and installation. Two extra front and rear membranes were fabricated because of the risk of damage in their assembly. Assembly operations were tried in Dallas for critical items, but an entire mirror module was not built until work was relocated to Albuquerque.

The major fabrication steps for this prototype are outlined below:

1. Fabricate mirror-module components
   a. membranes, front & rear
   b. trusses and hub
   c. heliostat ring
   d. drive adapter
   e. controls, and
   f. passive defocus mechanism.
2. Fabricate, assemble and test components.
3. Assemble mirror-module
   a. two membrane failures during tensioning, and
   b. insufficient pre-tension in completed module.
4. Investigate membranes and tensioning.
5. Fabricate ring stiffener and new membrane.
6. Fabricate new membrane vacuum layout table.
7. Retrofit stiffener and new membrane-to-mirror-module.
8. Install completed mirror module on drive pylon.

Work performed within each of these fabrication steps is presented in this chapter, which is divided into the following sections:

10.2 Membranes
10.3 Heliostat Ring
10.4 Rear Support Structure
10.5 Tooling
10.6 Controls
10.7 Site Assembly

10.2 Membranes

The membranes were fabricated from 5052-H34, stretcher-leveled aluminum coil stock, 36 in. wide. Two front and two rear membranes were made initially. Front membranes were laminated with 3M's reflective, silvered-acrylic ECP-300A film. After the first mirror module was completed, another two front membranes were fabricated, although only one was used. All membranes were fabricated from 13 varying length strips to provide a round membrane when completed.

Fabrication steps were

1. Laminate front membrane material,
2. Weld panels to form membrane disk,
3. Trim membrane O.D., and
4. Roll on rigid mandrel for transport.

Laminating

Laminating was done on a commercial, dry laminating line with some additional customized in-line operations. Two improvements were added since the first prototype was fabricated. The operations in sequence are defined in Table 10.1.

TABLE 10.1
OPERATION STATUS

Uncoiling	standard
Leveling	standard
Etchant washing	nonstandard
Squeegee drying	nonstandard
Entering dust-free conditioned chamber	new/standard
Masking application	new/nonstandard
Dust removing by tack cloth	standard
Reflective film laminating	standard
Edge tapelaminating	nonstandard
Premask laminating over reflective surface	nonstandard
Recoiling	nonstandard

Some areas of the finished front membrane do not have reflective film laminated to them. These are the edges of the individual panels where they are overlapped and welded together. Also bare is the outer edge of the membrane where it is welded to the heliostat ring and where the tooling was clamped to the membrane edge.

An improvement in the prototype was the selective lamination of the coil stock, so those areas did not have to be manually stripped. Selective lamination was originally proposed for the commercial assembly plan. Manual stripping can damage the coil stock and expose the permanent areas of the film to excessive heat and strong solvents, both used to remove unwanted film. Occurrence of poor welds due to contamination from incompletely removed film adhesive was also eliminated.

Selective lamination was achieved by taping custom-shaped paper masks to the coil stock before it entered the laminator to prevent adhesion between the aluminum and the film in the appropriate areas. A razor knife was later run along the clearly visible edge of the paper mask and the unwanted film lifted off.

Another improvement was the addition of a dedicated room just for the dry laminator machine. The air here is dehumidified and temperature controlled. The room is supplied with excess filtered air to keep out dust and dirt.

Membrane fabrication, after laminating, was identical for front and rear membranes. Strips of coil stock were unrolled and cut to length for the specific panel being welded to the membrane in progress. Extra length was allowed at both ends so that samples of the weld seam could be cut from both ends of every seam for quality control testing.

The panels were laid out on a flat, level table surface with vacuum hold-down capabilities. The panels were aligned and overlapped the required amount for welding before clamping with the vacuum. The first membranes made did not utilize the vacuum clamping. Observations of the completed mirror-module assemblies and failures in two membranes during tensioning convinced us that using the vacuum clamping significantly aided producing accurate flat membranes.

The panel layout table is actually a welding jig. A rolling resistance welder runs on tracks along the layout table so that the fixtured membrane does not need to be disturbed until it is welded, as shown in Figure 10.1. It is important not to release and refixture the membrane panels until they are welded along their entire length in order to assure a flat, finished membrane.

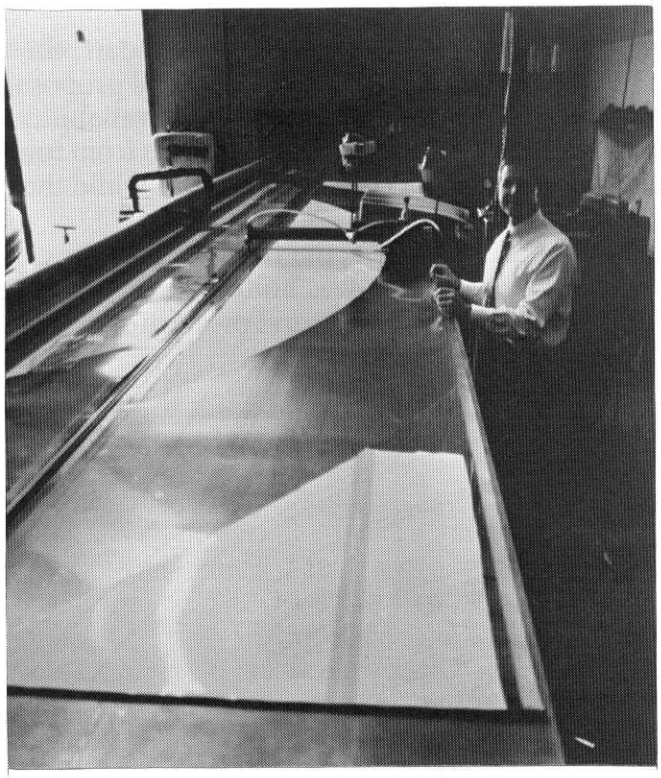

Figure 10.1 Welding Operation for Membrane Fabrication.
NOTE: The white circular segment on the membrane panel being fitted is the actual reflective area with a protective premask applied to it. Also visible is the completed 90% of the membrane already rolled up on the shipping mandrel to the left of the welding table. The traveling welder's arms are visible in the background.

Another improvement incorporated since the first prototype is the change from a seam of discrete spot welds to a rolling spot weld. The original welder tips were replaced with copper wheels, and the welder jaws were kept clamped closed all the time. This sped up the welding process and subjected the layout table to less banging, so it would remain flat and level longer without adjustment. Also tip dressing was required less often with the rolling electrode, so welding could continue uninterrupted for longer periods with less variation in weld quality.

While the membrane was on the layout table, samples for weld testing were cut from each end of each seam. The membrane outside diameter was laid out at each step and the O.D. cut to size.

The membrane was then released from the vacuum clamp and rolled onto a rigid 6 in. diameter mandrel until the free edge of the last panel added was positioned along the path of the weld electrodes. This portion of the membrane was then vacuum clamped and the next panel was laid out in position for clamping and welding.

10.3 Heliostat Ring

The heliostat ring was made from 6061-T6 American Standard channel, 6 in. x 3 lbs/ft with a 1.92 in. flange width. This was scaled from material proposed for the commercial design, but a standard profile was used because of availability for the prototype. Available lengths of channel required the ring to be made from four pieces. The tooling served as a welding jig to accurately hold the sections while they were welded.

In the area of the weld's heat-affected zone, the yield stress of the channel was reduced. A set of stiffeners, shown in Figure 10.2, was bolted to the ring at each joint to reinforce these areas to maintain the ring's structural properties.

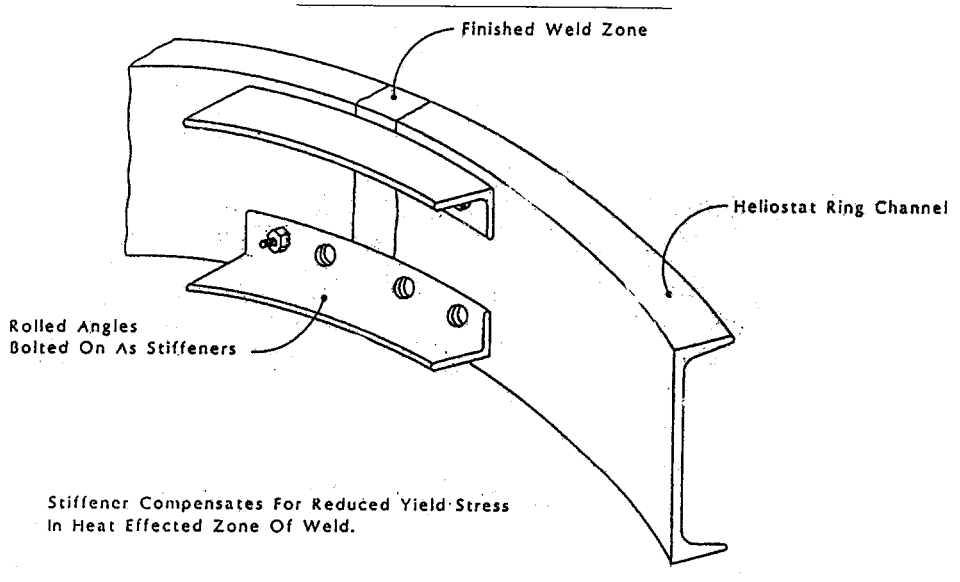

Figure 10.2 Heliostat Ring Stiffeners at Segment Splice Locations. The stiffeners were bolted in place to avoid any further weld heat effects.

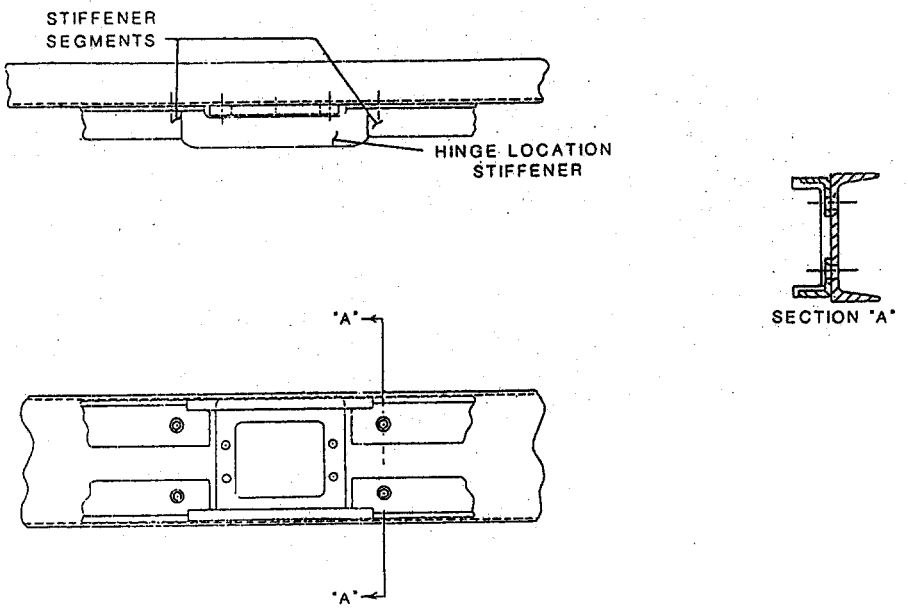

Figure 10.3 Detail of the Continuous Stiffener Retrofitted to the Heliostat Ring. These replaced the stiffeners shown in Figure 10.2.

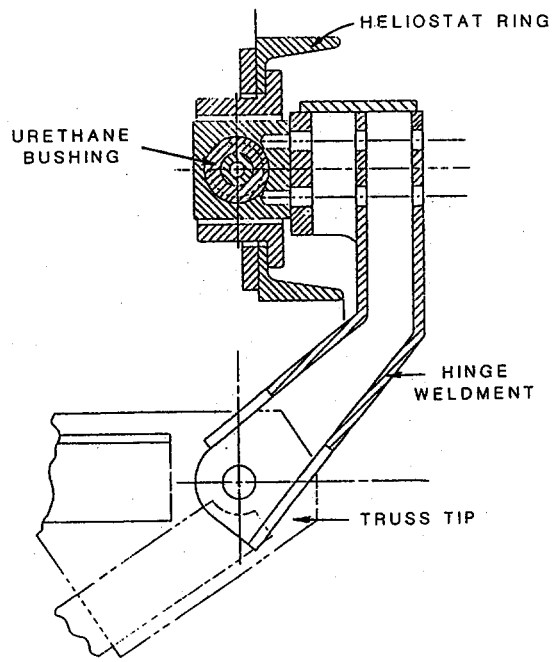

Figure 10.4 Hinge Connection Detail for Truss Tip to Heliostat Ring.

When the first mirror module was completed, the front membrane was determined to have too low a tension. One possible contributor to this problem was determined to be excessive shrinkage (i.e., compression) of the ring from the tension of the membranes. Therefore, as a precaution when refitting a new membrane to the ring, a continuous stiffener was bolted to the inside of the ring. The stiffener was fabricated from 6061-T6 aluminum, 1.5 in. x 2 in. x .25 in. American Standard channel, as shown in Figure 10.3. The stiffener increased the ring cross-sectional area and reduced its shrinkage when the tensioned membranes were in place.

Subsequent analysis of the membranes, ring, and tension measuring techniques suggests that this additional stiffening was not required if all other elements were installed as designed. The next heliostat built will use a slightly heavier channel for a little more conservative design. No separate stiffener will be needed in any heliostat. No stiffening is proposed for the commercial design.

Other details of this ring which differ from the previous prototype are the hinge connections linking the truss tips to the ring, as indicated in Figure 10.4. Two pins are used, one at the truss connection, and one at the shear center of the channel. The use of two pins allows differential expansion of the steel truss and aluminum ring assemblies without adding any loads to these elements. The location of the ring connection pin at the shear center of the channel reduces additional torsion in the ring from normal loads transferred through the hinge connections. This improved connection is scaled from the commercial design, as shown in Figure 10.4

Additionally, the pin connection to the ring is mounted in a urethane bushing so that out-of-plane bending moments will not be imposed on the heliostat ring by side loads transferred through the hinge elements.

The heliostat ring was supported at 12 points by the tooling during all of its fabrication and subsequent assembly operations. At each support point, a clevis was fastened to the ring with machine screws. The clevis pinned to a support arm while it was in the tooling. After final assembly, the clevises were removed and a stainless screw was left in the threaded holes to prevent air leaks when the heliostat is in operation.

10.4 Rear Support Structure

The prototype's rear structure was built just like the proposed improved commercial design. Hot-rolled structural shapes were fabricated into a conventional tapered truss. The hub is simply a section of tubing with flanges and gussets at both ends, as shown in Figure 8.2.

A weldment at the truss tip houses an oil impregnated bronze bearing for the hinge pin. At the root of the truss, the primaries and secondaries slip over fins on the hub structure and are bolted in place. These holes were match-drilled in place.

After painting, the rear support structure was completed in the field by first anchoring and leveling the hub on a short block. The trusses were then assembled and tie rods added. A surveyor's level was used to adjust the tie rods to maintain planarity of the truss tips. The tip-to-tip spacing of the trusses also had to be maintained. This required an iterative process for adjusting the tie rods, which was somewhat time consuming.

10.5 Tooling

A key element to producing an accurate heliostat is the tooling used during its assembly. Complete control must be maintained over the planarity and trueness of the heliostat ring during its assembly, during membrane welding, and during mirror-module assembly to the rear structure. Control must also be maintained over the accuracy of fixturing the membranes to the tensioning rings.

A very different approach to tooling was used to build this prototype than for the first one. This approach paralleled the proposed improved process plan for the commercial design. The primary change was that the tensioning task was transferred to the tooling from the heliostat element. This resulted in a requirement for more substantial tooling elements. Figure 10.5 shows a schematic of the major tooling elements.

Tooling installation, however, was simplified by using fewer supports for the layout table and simpler supports for the tooling pylons. Simple adjustability was built into the tooling to reduce the tolerances required in installation and allow quicker set-up. The welder followed a single rail and was insensitive to leveling, thus eliminating track installation, adjustment, and leveling.

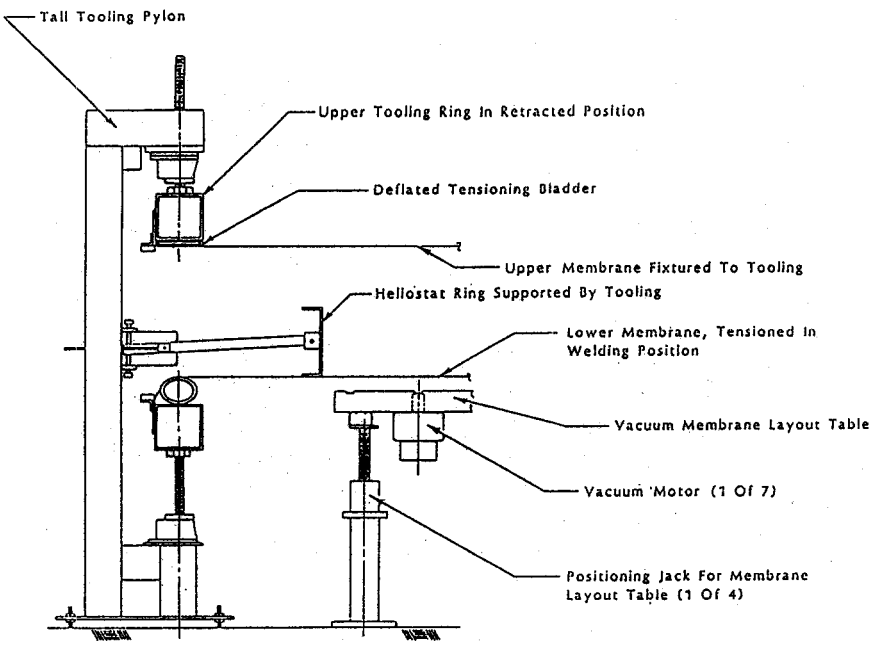

Figure 10.5 Schematic of a Single Tooling Support Pylon. The pylon shown is a tall pylon, which supports both the tooling rings and the heliostat ring.

For this prototype, a moveable vacuum layout table was used to aid fixturing the membranes to the tooling. It only needed to move in one dimension, although the commercial plan requires the platens to be moved through the assembly area. This movement insured that the ring element, once leveled and concentric, was not disturbed until the entire assembly was completed.

The tooling consisted of six tall pylons that supported the heliostat ring and the tooling tensioning rings. Another six short pylons supported only the heliostat ring. The heliostat ring, therefore, was supported at 12 points, as shown in Figure 10.6. As indicated in Figure 10.6, each ring channel support point could independently adjust and maintain the radial position and height of the ring. Final ring planarity was maintained to +/-0.008 in. Concentricity was maintained to +/-0.060 in. The tensioning rings could each be raised and lowered by screw jacks on the support pylons. The lower ring was supported from below and the upper ring from above.

In the center of the tooling rings was a round layout table that could be raised and lowered. This was used to support the membranes while they were being fixtured to the tooling. Experience with assembling the first mirror module for the Mark II prototype revealed the importance of fixturing the membranes to the tooling with minimal slack and uniform fit-up all the way around. For the final Mark II mirror module assembly, a new layout table with vacuum hold down was installed to improve the flatness of the membranes while they were being clamped to the tooling. This seemed to significantly improve the uniform tensioning of the membrane.

The sequence of membrane-to-tooling fixturing is described in Figure 10.7.

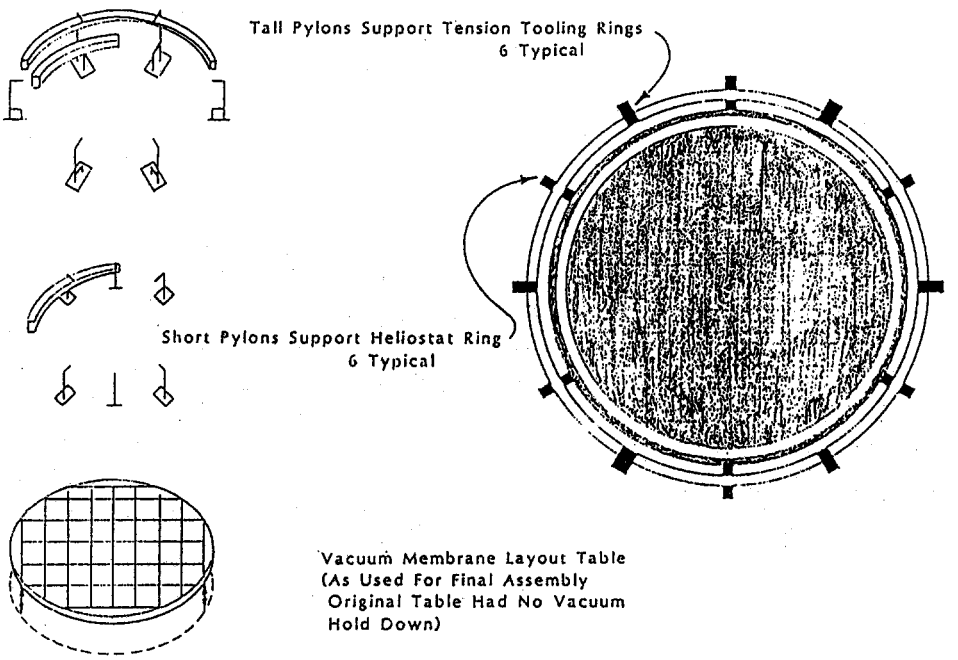

Figure 10.6 Definition of Major Tooling Elements.

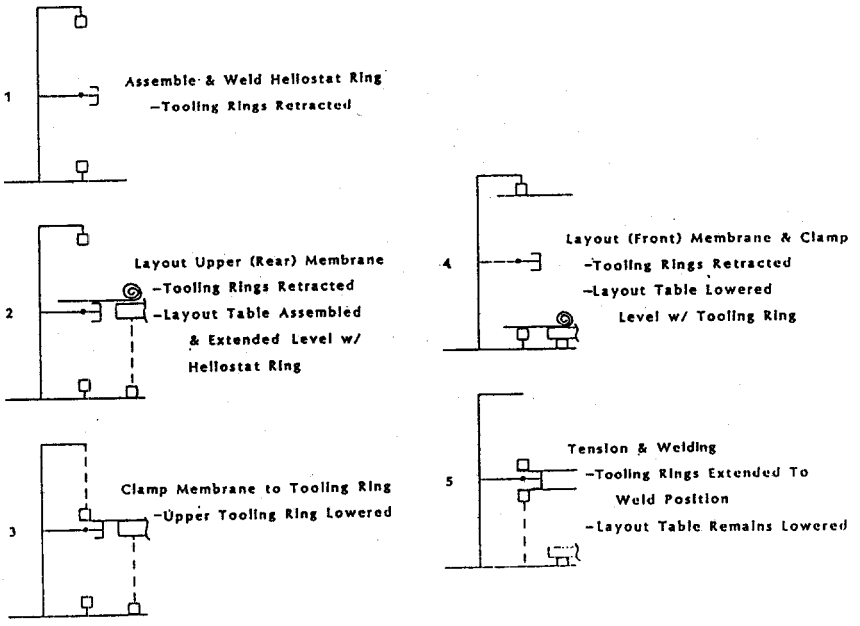

Figure 10.7 Sequence of Operations for Membrane Fixturing-to-Tooling.

10.6 Controls

The heliostat controls consist of an active and a passive system. The active system can be used for focus and defocus control. The passive system can provide defocus only, but can do so with or without power to the system. The active system is designed like the controls for the commercial design. The passive system is an experimental design and would be redesigned for economical production if used on the commercial design.

The actuator in the control system is the fan. It uses a dc motor-driven axial flow fan in a close-fitting shroud. The intake to the fan has a paper element cartridge filter similar to an automotive intake filter. A weather cover protects the filter and other heliostat-mounted control components, as shown in Figure 10.8.

Active Control

The purpose of the active control system is to control the reflective membrane position by monitoring a signal from a LVDT and, in turn, to control an axial fan (direction and speed) to position the membrane. The control also monitors for alarm conditions, alerts an operator, and shuts down the heliostat, if an alarm occurs. The controller operating mode can be selected remotely or locally.

The major components of the active control are

a. axial fan with 90-VDC motor
b. intake filter
c. LVDT reflective membrane position sensor
d. membrane over travel limit switch
e. programmable logic controller, and
f. dc motor controller.

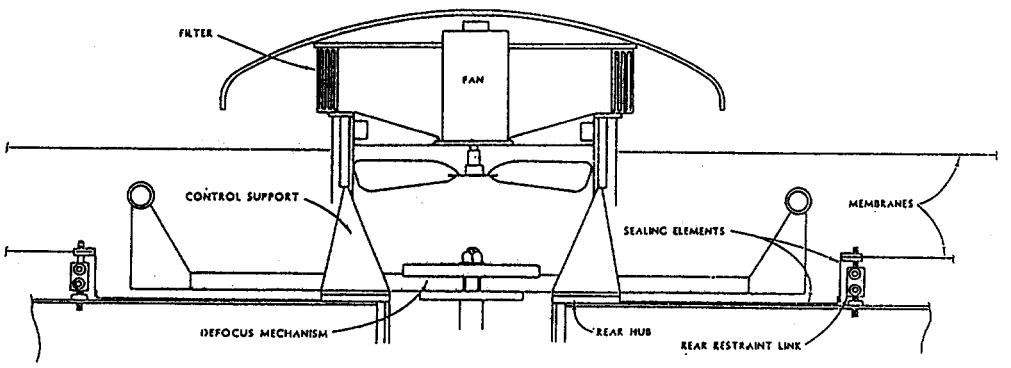

Figure 10.8 Heliostat Control Components Mounted Within Heliostat.

The axial fan is supported from the rear by the central hub; however, it is located in the center of the front membrane as shown in Figure 10.8. There is a cartridge-type paper element air filter and a weather cover on the outside of the fan shroud. The LVDT has a simple axially adjustable mount also on the central hub. The LVDT core is secured by a threaded rod fastened to the front membrane and its reinforcing rings to allow further axial adjustment. An inductive membrane over travel switch mounts at the same location as the LVDT.

The electronic controls and interface to the field control are in an enclosure at the base of the pylon. The programmable logic controller is a standard industrial modular unit. The PLC used was the smallest series in that manufacturer's line. One of these units can control several heliostats. It uses an analog input from the LVDT transmitter and it outputs an analog signal, which the dc motor controller follows. Two additional on/off outputs tell the dc motor controller the direction of motor rotation.

The control algorithm is the velocity form of a PID control as follows:

$$\text{delta } M_N = K_C[(E_N - E_{N-1}) + K_I E_N - K_D(PV_N - 2PV_{N-1} + PV_{N-2})]$$

M_N	=	CONTROL LOOP OUPUT
E	=	ERROR = SETPOINT - PV
PV	=	PROCESS VARIABLE = MEMBRANE POSITION
K_C	=	PROPORTIONAL GAIN
K_I	=	INTEGRAL GAIN
K_D	=	DERIVATIVE GAIN
N	=	VALUE AT CURRENT SCAN TIME
N - 1	=	VALUE AT LAST SCAN TIME

The velocity form of the PID equation is obtained by taking the conventional position PID equation at time (n-1) and subtracting it from the equation at time (n). This results in calculating the change in loop output rather than an absolute output value. This makes implementation on a simple controller easier because the equation is simpler and fewer data values need to be stored. No initial bias needs to be set with this form. Reset-windup protection is implicit in the velocity form.

The desired membrane position for either active focus or active defocus is stored in a lookup table in the PLC memory, as are all the constants used in the control algorithm and the scan rate. Scan rate used was 4 Hz.

Passive Defocus

The purpose of the passive defocus is described for the commercial design in Section 5.2. Also described is the logic for requiring a mechanism with essentially an inverse spring constant.

The mechanism had to be mounted within the rear structure hub. Adjustability of the latch force, defocus force and the shape of the displacement/force curve was provided for. The mechanism was also designed so that it could be readily removed if the need arose.

The mechanism was designed to have a latch to hold it in the cocked position, which could be tripped upon loss of power. This was accomplished by connecting a dc solenoid to a pawl. When the solenoid is energized, the pawl is withdrawn and the defocus mechanism springs out to defocus the membrane. The pawl uses a roller catch to minimize friction and energy requirements of the solenoid. Friction is also minimized because the pawl must only restrain the reduced latching force.

When the pawl is withdrawn, it is in turn latched in the release position by a second pawl. This prevents accidental relatching of the defocus mechanism.

Energy to activate the defocus solenoid upon power loss comes from a capacitor bank. Line power holds a normally closed relay contact open whenever it is present. The line power also keeps the capacitors fully charged at all times. Upon power loss the relay contacts dump the capacitors across the solenoid to trip the mechanism. The capacitors are also dumped across the fan motor in the intake direction so that the fan assists in defocusing the membrane.

Relatching the defocus mechanism can only be done with the power on and an appropriate input signal to the controller. The latching sequence requires the fan to exhaust at full speed until the front membrane is drawn inwards and overpowers the spring in the defocus mechanism. When the LVDT signal indicates the membrane is drawn back far enough to latch, the PLC energizes a latch solenoid that releases the main latching pawl to engage the defocus mechanism shaft. The fan is then deactivated and the controller awaits further instruction.

10.7 Site Assembly

The mirror module for the 50 m^2 prototype is too large to ship as one piece. Therefore, the assembly and tensioning tooling had to be set up in the field and the mirror module assembled from basic components. Figure 10.9 shows the sequence followed.

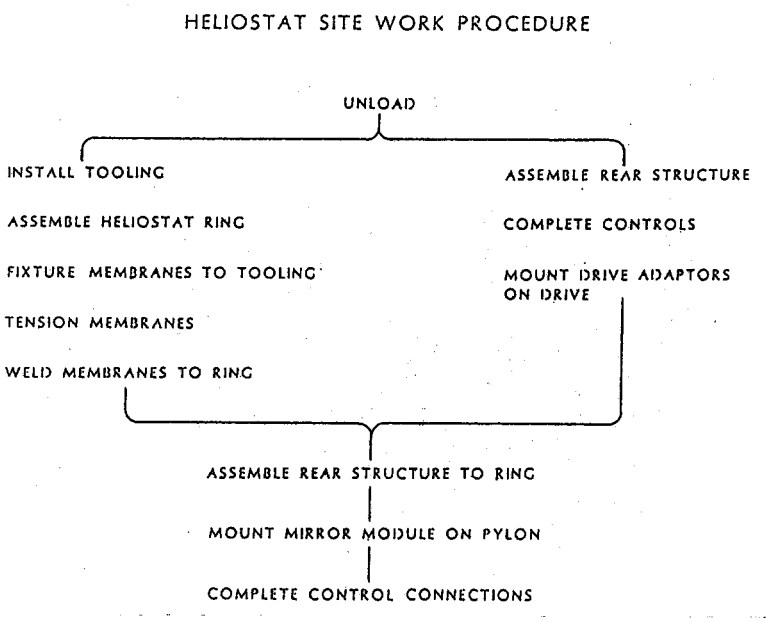

Figure 10.9 Assembly Sequence for Prototype Site Work.

Most of these operations proceeded smoothly. The significant exception was the fixturing and tensioning of the membranes. Two membranes failed during tensioning. One failed at a very low tension, most likely due to poor seam weld strength. This probably happened because, during the membrane fabrication, there were a couple of seams that did not have coupons cut from them for weld testing.

The second membrane failure apparently resulted from local tension being greater than that indicated by the tension measuring method being used. This problem can result from two sources. If the membrane is not evenly fixtured to the tooling, more tension can be applied along the diameters that have less slack in them because of the geometry of the force applied by the tensioning bladder. Additionally, if the membrane is fabricated so that its natural shape is not a flat disk, there will be nonuniform tension in the membrane. If during lay-up of the panels of the membrane the seams are not kept straight, a cone or saddle-shape will result. For a saddle-shape, this will lead to more slack in the fixtured membrane along some diameters than others. For a cone-shape, the diameters will be even, but the circumferential tension will increase faster than the radial tension.

The other problem that occurred during assembly was a lack of adequate tension and non-uniform tension in the front membrane after welding was completed. A distinct radial pattern of wrinkles appeared in the membrane when tension was transferred from the tooling to the heliostat ring. The wrinkles extended from the outside edge

two-thirds of the distance toward the center. The wrinkles were somewhat less apparent while the membranes were being tensioned, prior to welding. There were only three areas showing any wrinkles when the membrane was at full tooling tension. After release of tooling tension, the final tension in the membrane could not be accurately measured, but was qualitatively determined to be much too low. This problem could result from several areas. After investigating several possibilities, the following causes were determined:

1. The fabricated shape of the membrane was probably not a flat disk. If it was a saddle-shape, there would be extra material in the circumferential direction. This would first result in non-uniform tensioning, as described. It would also result in radial tension being greater than circumferential tension. The pattern of wrinkles after final assembly suggested no significant circumferential tension.
2. The tension measuring method indicated the tension in one area only, not a good average membrane tension. The tension measuring method used measured only radial tension that was greater than the circumferential component.
3. The heliostat ring was suspected to have shrunk more than predicted upon transfer of membrane tension from the tooling. To be conservative when a new front membrane was installed on the mirror-module, a stiffener element was bolted to the inside of the heliostat ring, as described in Section 10.3, to increase the cross-sectional area and, thus, reduce ring shrinkage. Analysis made after the final assembly showed this step was probably not necessary, if all other variables were adequately controlled.

The important improvements implemented during the replacement of the front membrane were

1. The use of vacuum hold-down while welding membrane panels during initial fabrication.
2. The use of vacuum hold-down during lay-out and fixturing of the membrane-to-tension tooling.
3. The use of membrane center deflection as an indicator of the average membrane tension.

The first two were used on the Mark I, but thought to be unnecessary.

After the membranes were welded to the ring, they required two more operations. The outer edge of the membranes (outside of the heliostat ring) was cut away. The periphery was rolled over to eliminate exposed sharp edges. Also, holes were cut in the center of both membranes to provide the front fan reference and to provide service access through the rear membrane. Around each hole, a series of thin aluminum rings was glued and riveted to reinforce these edges. The stack-up used is detailed in Figure 10.10. In the front membrane, these rings defined the clearance between the fan shroud and the membrane, which also defined the air leakage. The front reinforcing rings also provided a mounting spot for the LVDT core. The rings on the rear membrane provided a member to spread out the load within the rear membrane from

the six links that restrained the rear membrane to the rear structure. They also provided a flat surface to which to fasten the rear sealing element, as shown in Figure 10.8.

REINFORCING RING

	Thickness	I.D.	O.D.
A	.060	17	26
B	.020	17	32
C	.040	44	68
D	.030	44	80
E	.020	44	92
F	.060	44	56

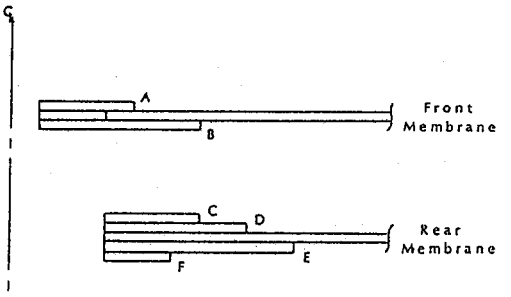

Figure 10.10 Detail of Reinforcing Rings Applied to Membranes about Central Holes.

The final step of mirror-module assembly was attaching the rear support structure to the heliostat ring. The rear structure was already completely assembled and concentric, and the hinge connection weldments pinned to the truss tips. The structure was lowered over the heliostat ring and the hinge weldments aligned with the mounting holes in the ring, bolted, and sealed. The dimensions are such that the rear structure fits inside the tension tooling rings. The tooling supports for the heliostat ring were then removed so the ring was supported by the rear structure and its rigging. The entire module was then lifted out of the tooling and rigged-out to the pylon for installation.

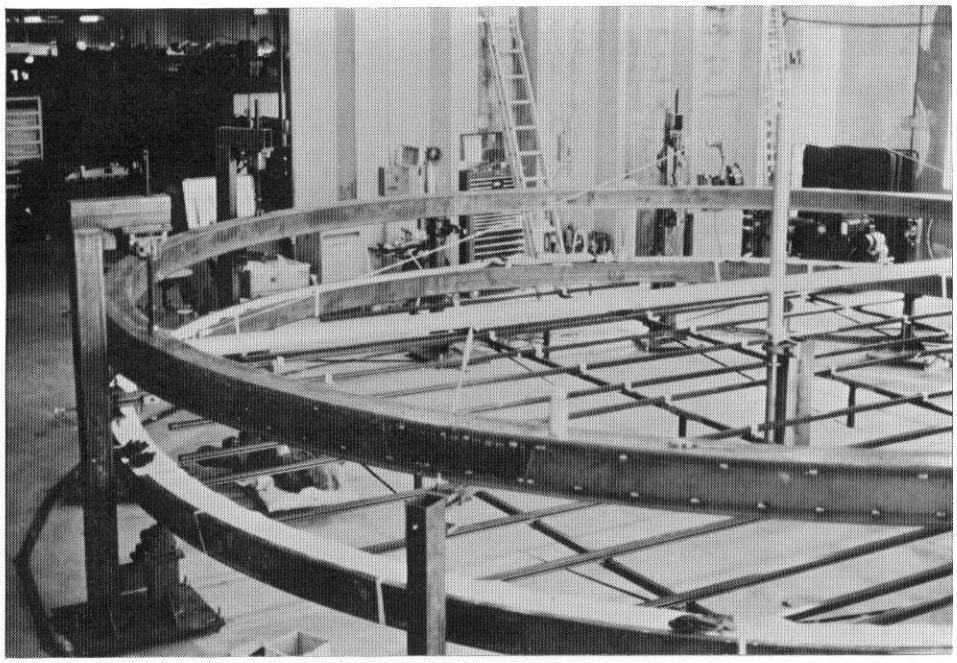

Figure 10.11 Mirror-Module Assembly and Tensioning Tooling Setup at Sandia's CRTF Assembly Building. Visible are upper and lower moveable tensioning reaction rings, heliostat ring support pylons, lay-out table support framework, and central rotating sweep arms.

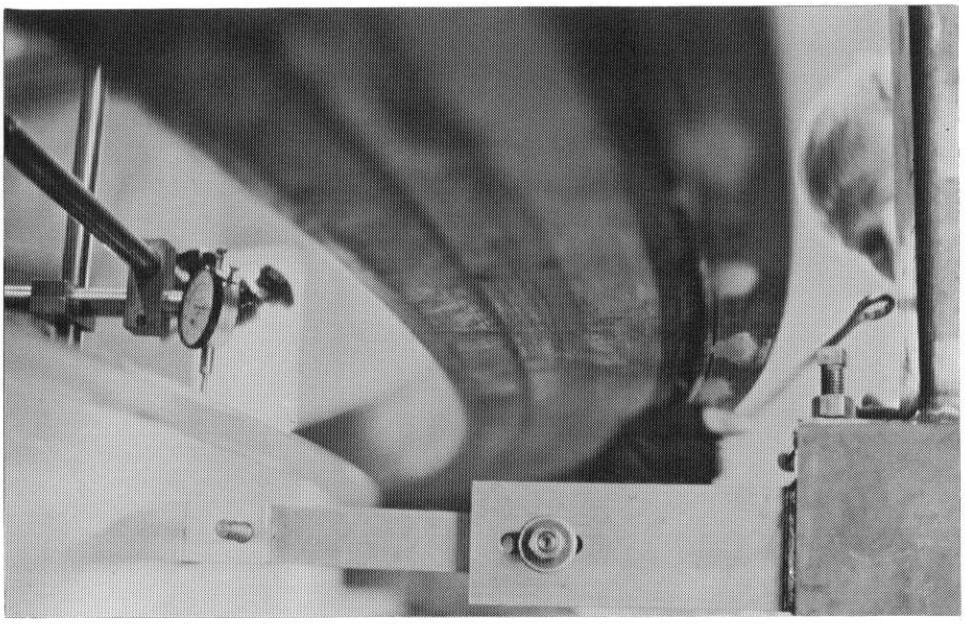

Figure 10.12 Heliostat Ring Channel Segment and Ring Support Pylon. The ring is being adjusted to set planarity and radius with dial indicators mounted on the central sweep arm.

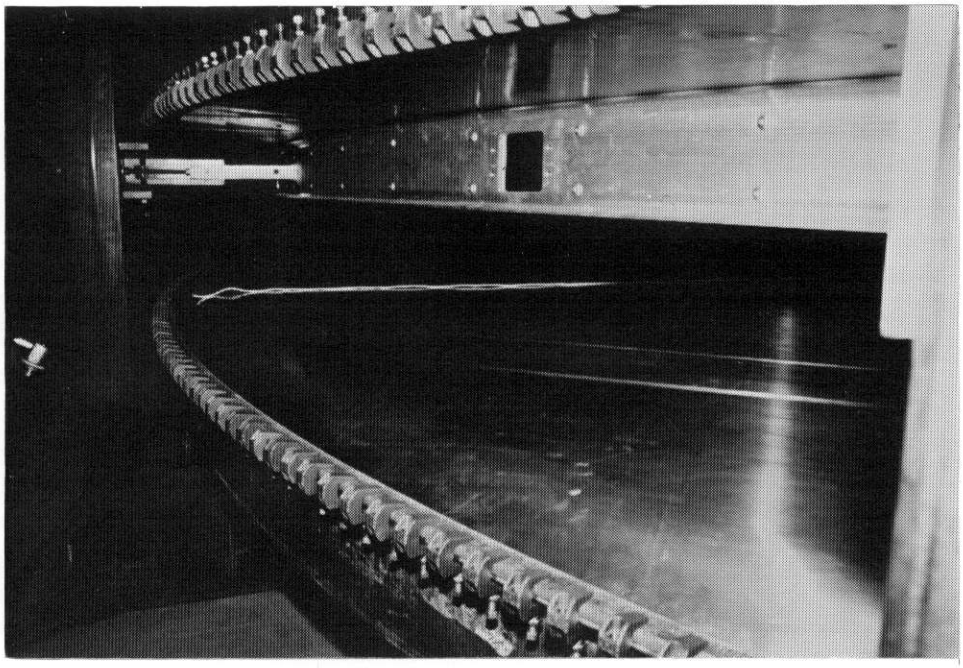

Figure 10.13 Tensioned Membrane and Lower Tension Reaction Ring. Reaction ring is in lowered position prior to raising for welding.

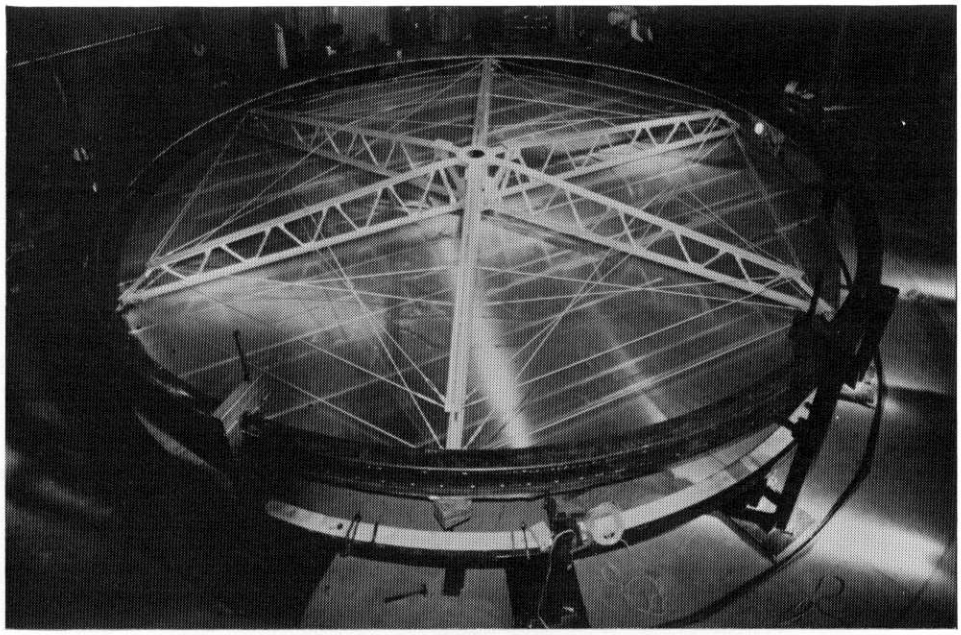

Figure 10.14 Complete Mirror Module Supported in Tooling. Rear structure has been attached to heliostat ring.

Figure 10.15 Complete Mirror Module Being Rigged Out of Assembly Building at Sandia's CRTF.

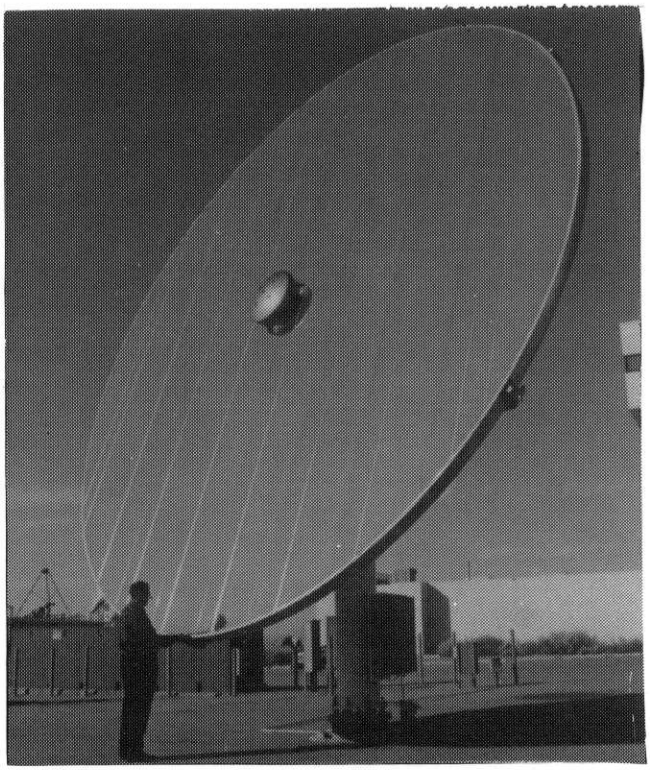

Figure 10.16 Front View of the SKI Mark II Prototype Heliostat.

Figure 10.17 Rear View of the SKI Mark II Prototype Heliostat.

11.0 Evaluation

This section details the similarities and differences between the commercial design and the prototype. Tests required to evaluate the prototype performance are discussed. Characteristics to be investigated are beam quality, performance in varying wind conditions, steady and transient, survival in high-wind conditions, and material/component life. Testing and evaluation of the assembly are to be done by Sandia.

Table 11.1 shows a comparison between the commercial and prototype heliostat construction.

11.1 Design Scaling

A 50^2 m prototype was designed and built using similar criteria as for the commercial design. It was not simply scaled from the commercial design. The commercial design was duplicated as closely as practical. There were a few details in the prototype design that varied from those proposed for the commercial unit due to constraints on availability and cost of materials.

A stressed-membrane heliostat is a complex structure to design optimally. The individual components react to external loads in a synergistic manner to distribute loads through the structure by means of the membranes, ring, and trusses. As a result of both the numerous couplings between the components and the external loads being a function of ring radius, simple scaling from one design to a different size is not possible. The prototype was designed using the same methods and criteria described in Sections 3 and 4 for the commercial design.

There were also some details in the fabrication processes that varied from those proposed for the commercial unit due to constraints on availability of materials and equipment. The cost of building custom equipment that would closely duplicate the proposed commercial assembly operation was prohibitive in some cases. The tooling was designed to fixture the heliostat ring and membranes in the same conditions and positions during assembly as the proposed commercial tooling. The means of tensioning was different than the commercial design as described in Section 9. The speed and convenience of setup were not representative of a commercial operation. However, the tooling was transportable and very flexible as is required for a prototype operation.

11.2 Performance Testing

Sandia began testing of the prototype immediately after installation in February 1989. Preliminary results show excellent optical performance. The focus control system performs very well in calm wind and gusty conditions from all orientations tested [12, 13].

Sandia's beam characterization system (BCS) has been used to map the flux of the reflected beam on target. One plot is shown in Figure 11.1. A comparison of the measured beam, with an analytical prediction by the HELIOS computer code, is shown

TABLE 11.1

MIRROR-MODULE	PROTOTYPE	COMMERCIAL DESIGN
Ring outside diameter	27 ft.	45 ft.
Nominal aperture area	558 $ft.^2$	1615 $ft.^2$
Membrane material	5052-H34 Aluminum	5000 series aluminum
Membrane thickness	0.010 in.	0.010 in.
Membrane weight	87 lbs ea.	235 lbs ea.
Membrane pretension	45 lbs/in.	45 lbs/in.
Membrane stress	4500 psi	4500 psi
Membrane tooling tension	95 lbs/in.	130 lbs/in.
Reflective film	ECP-300-A by 3M	Silvered polymer
Ring material	6061-T6 aluminum	5000 series aluminum
	6 in. x 1.92 in. web Am.Std. Channel	8.25 in.x 1.25 in. x .29 in. custom channel
	2.83 lbs/ft.	3.66 lbs/ft.
Ring height	6 in.	8.25 in.
Ring cross sectional area	2.4 $in.^2$	2.9 $in.^2$
Ring weight	251 lbs total	517 lbs total
Ring moment of inertia -Ixx	13 $in.^4$	24.7 $in.^4$
Ring moment of inertia -Iyy	0.72 $in.^4$	0.28 $in.^4$
REAR SUPPORT STRUCTURE		
Number of trusses	6	6
Truss material	ASTM A36 steel	ASTM A36 steel
Height at root/tip	24.0/12.9 in.	46 in.
Root moment of inertia	374 $in.^4$	1440 $in.^4$
Truss weight	205 lbs ea.	295 lbs ea.
Hub material		
Hub weight	126 lbs	300 lbs
Rear restraint diameter	48 in.	48 in.
CONTROLS		
Prime mover	Axial fan	Axial fan
Sensor type	LVDT	LVDT
Passive defocus push diameter	40 in.	40 in.
Mirror Module weight w/ rear structure w/o drive adapter	1843 lbs	3400 lbs
Weight/aperture area	3.2 lbs/ft^2	2.1 lbs/ft^2

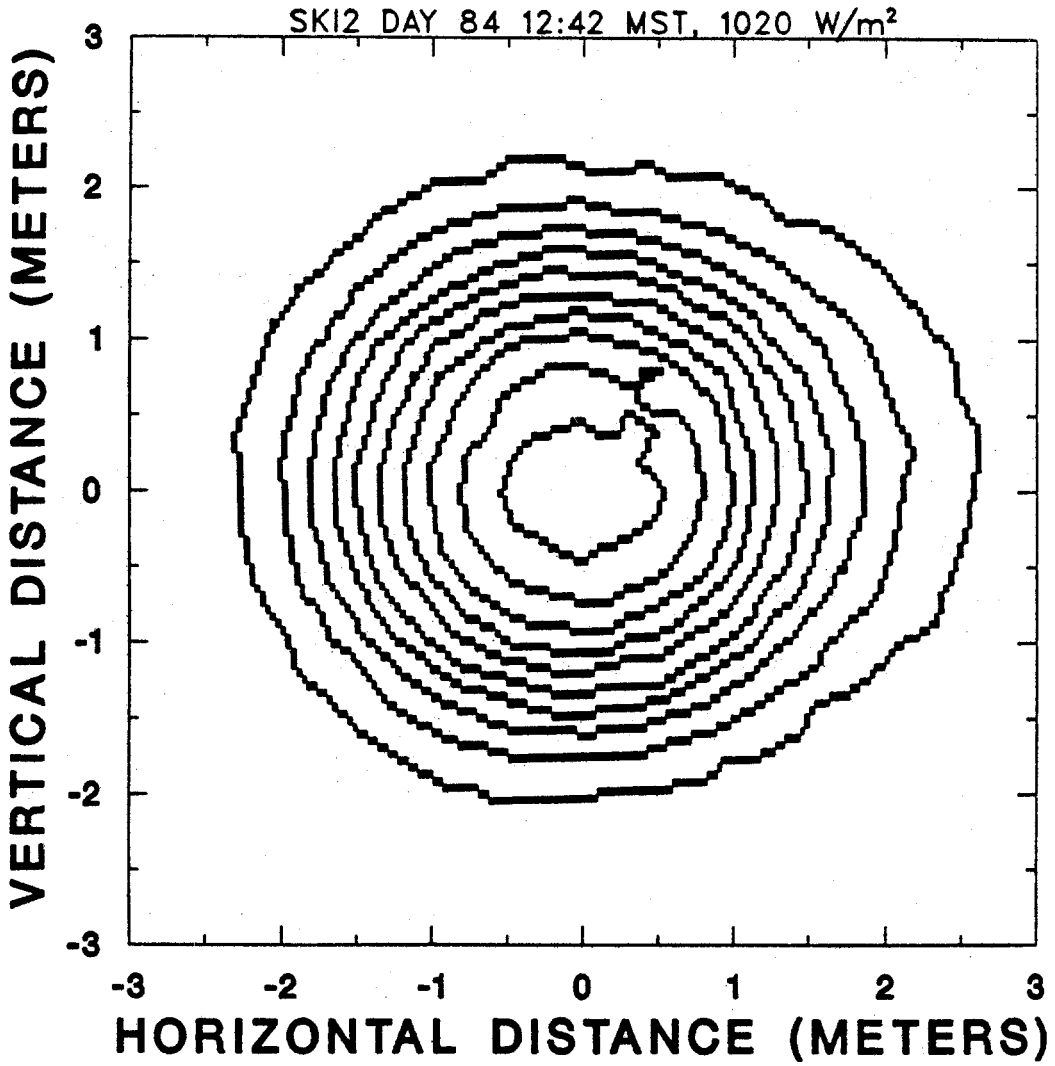

Figure 11.1 Measured Flux Contours of the Beam Spot. Contour spacing is 0.5 kW/m^2. Total beam power was 40 kW and the insolation was 1020 W/m^2. Winds were 9 mph.

in Figure 11.2. The parameters used by the code to get a best fit of the analytical solution to the measured data assumed a circular-normal distribution of slope error with a mirror-normal sigma of 1.35 mr (2.7 mr beam dispersion).

HELIOS projections confirm the physical measurements indicating that 96% of the front surface is reflecting energy on the target.

On-target energy measurements made during windy conditions show excellent control by the focus control system. In Figure 11.3, 95% of the energy available in calm winds was available on target with winds of 20 mph gusting to 29 mph.

Another indicator of control system performance is the actual reflective membrane position as a function of time during windy conditions. A plot of membrane position of both the first and second prototype is shown in Figures 11.4 and 11.5 for the same

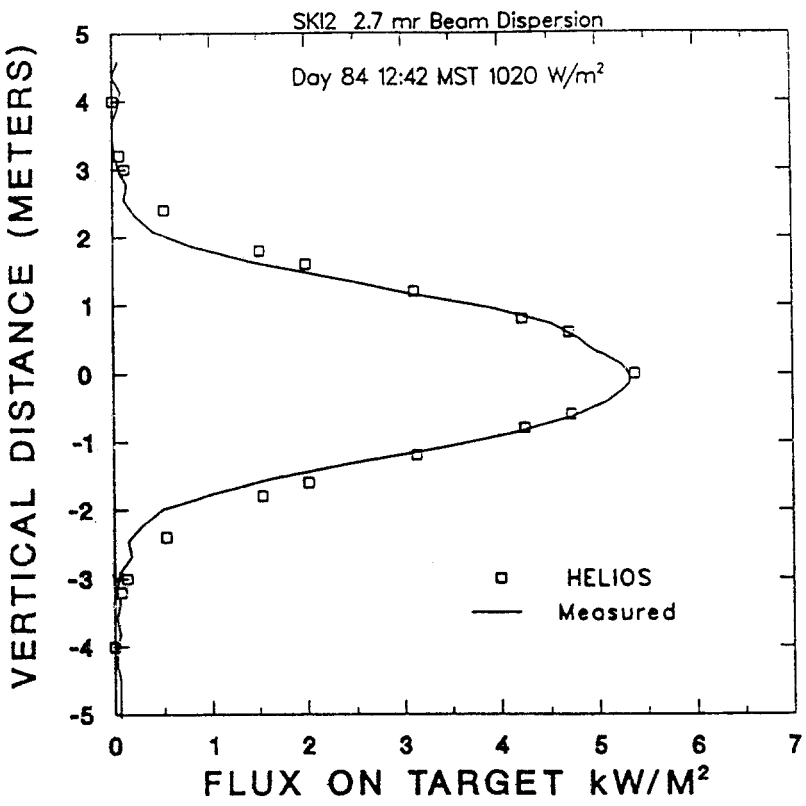

Figure 11.2 Measured and Modeled Beam Flux Profiles. Comparison of the measured vertical beam profile through the centroid of the beam spot and the HELIOS-calculated profile (squares) assuming a 2.7-mr beam dispersion error.

period as used in the previous figure. Comparison demonstrates the large improvement in control for the new model.

Power consumption by the control system itself has not been measured yet. It should be slightly less than that of the first prototype, particularly in gusty wind conditions.

Defocusing can be accomplished in two ways. The active defocus system is operational, but can be optimized further to reduce response time. Preliminary measurements show response is currently in the 10-second range. The passive defocus system cannot be fully tested until additional damping is added to the trip mechanism to eliminate shock loading of the front membrane.

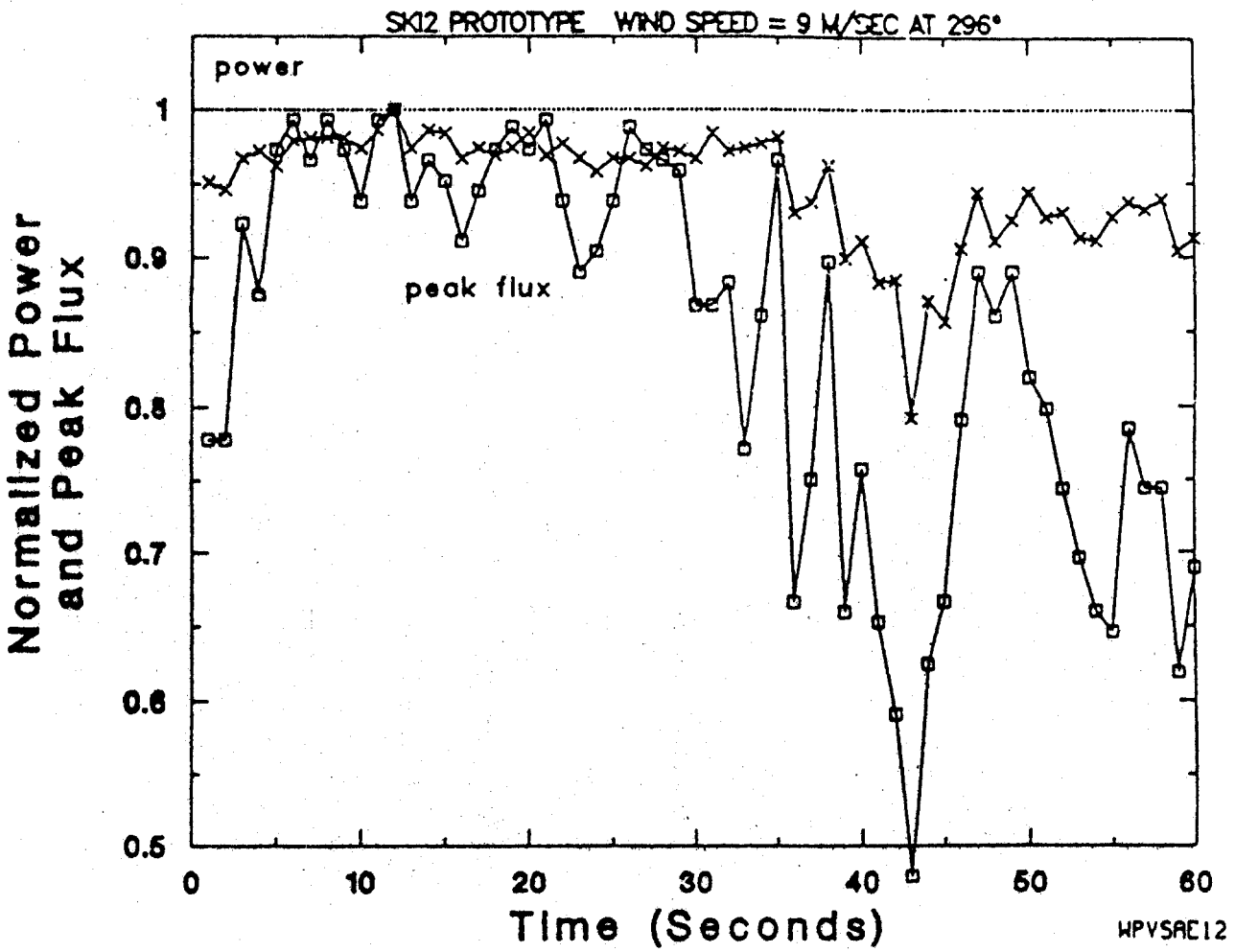

Figure 11.3 Measured Variation in Relative Peak Flux and Total Beam Power. Wind speeds averaged about 20 mph with gusts up to 29 mph. The data were collected under similar conditions as shown in Figures 11.4 and 11.5.

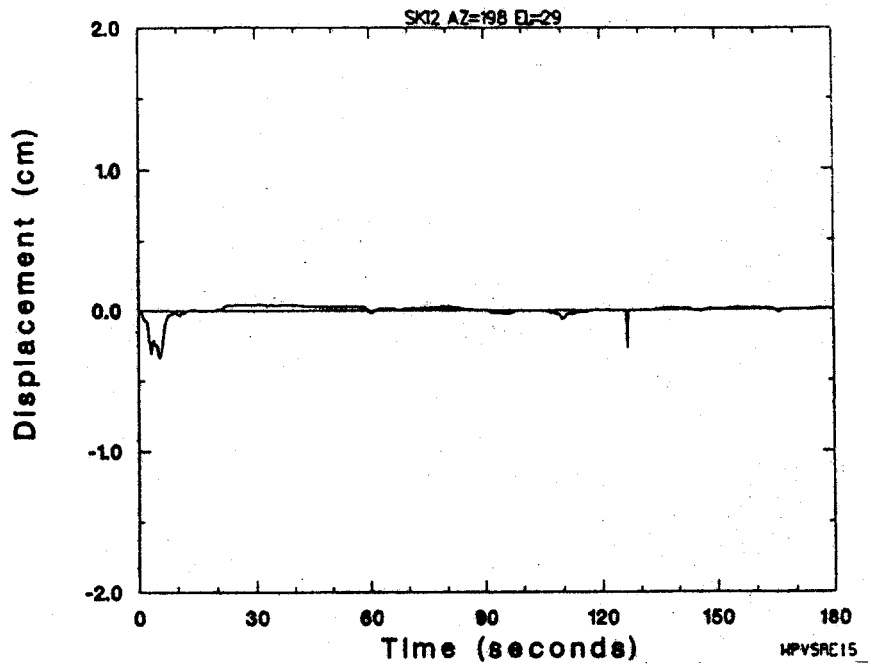

Figure 11.4 Measured Position of the Front Membrane for Mark II Heliostat. Wind speeds averaged about 20 mph with gusts up to 29 mph. The data were collected at the same time as the data in Figure 11.5.

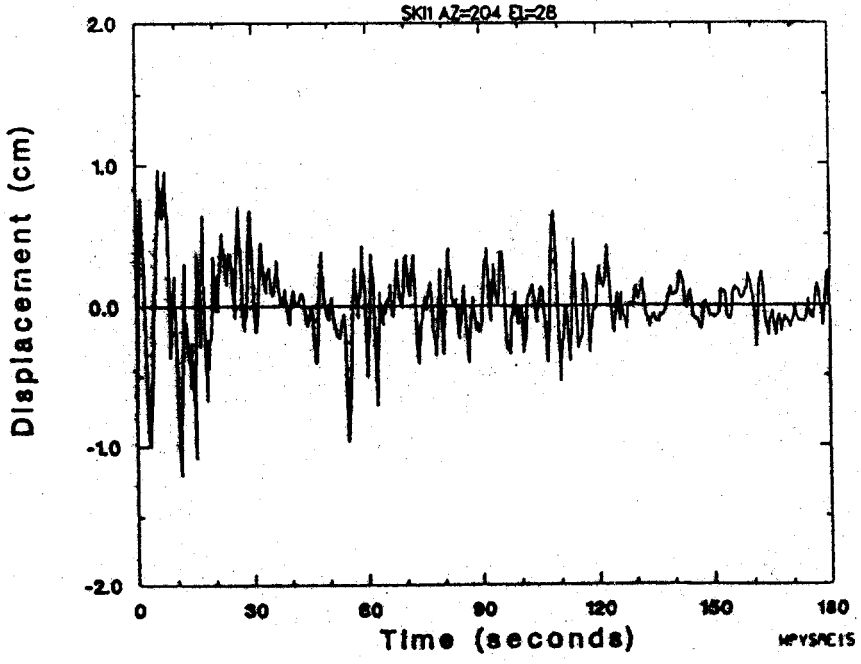

Figure 11.5 Measured Position of the Front Membrane for Mark I Heliostat. Wind speeds averaged about 20 mph with gusts up to 29 mph. The data were collected at the same time as the data in Figure 11.4.

12.0 Conclusions

The objective of this contract was to improve performance while reducing costs of the Mark I stretched-membrane heliostat design. Cost projections for commercial-scale production show an 8% reduction in mirror-module cost; a net difference of $2.31 per square meter of aperture (1985$). Preliminary test data indicate a performance level equal to or better than any other heliostats currently installed at Sandia's CRTF.

Five major design improvements were investigated and applied to the 150-square-meter commercial design. Improvements have been demonstrated with the successful fabrication and installation of a 50-square-meter prototype.

Preliminary performance testing of the prototype indicates a very satisfactory slope error of 1.3 mr mirror-normal. Performance in gusty wind conditions is greatly improved over the original Mark I prototype and is well below Sandia's heliostat specification of 3 mr (mirror-normal) [14].

The design improvements implemented were as follows:

1. A restraint was added to the rear membrane to reduce wind-induced membrane movement.
2. An open section was used for the ring frame design to improve structural efficiency.
3. The rear support structure was designed based upon wind profiles developed in wind tunnel testing to use a less expensive material.
4. Control improvements included relocation of the control transducer to reduce error and addition of a passive defocus mechanism.
5. The mirror preload was applied with nonconsumable tooling.

An additional improvement was to position the fan at the center of the front membrane.

12.1 Summary of Design Improvements

The restraint of the rear membrane reduced the changes in volume of the plenum between the two membranes of the mirror module from wind-induced pressure variations. Analysis indicated that the amplitude and duration of dynamic errors were reduced. The restraint provided an important secondary benefit with the reduction of normal loads on the ring and support structure.

The normal load reduction on the ring frame and support structure was achieved by providing an additional path to ground through the restraint. Approximately 13% of the total normal load was transferred to the drive directly through the restraint, rather than by transferring it to the ring and support structure. The reduction in normal load also reduced the asymmetric error of the ring. The ring weight was determined in reaction to the compressive radial load. This load component was reduced by 5% with the central restraint. Consequently, the rear membrane restraint translated to a direct reduction in ring weight.

The central restraint also reduced the transient error associated with changes in the wind velocity. There was an approximately 38% reduction in the volume of air the fan had to move to compensate for wind-induced membrane movement. The time required by the control system to respond to dynamic pressure changes was directly proportional to the change in volume. The restraint also reduced the amplitude of the transient error by 20%.

The reduced radial and normal loads were subsequently applied to a design of the ring frame. An open section ring was selected for the mirror module because torsional reactions were alleviated by the double membrane design. A concentric compression assumption was established as adequate, and the minimum ring cross-sectional area was determined as a function of the membrane preload. A somewhat arbitrary selection of 45 lbs/in. (7.9 kN/m) was made for the membrane tension based upon limiting the transient error term and keeping the membrane stress well below yield during assembly and operation.

The stress from bending and cross-sectional distortion of the ring were established in the structural analysis. Bending in the ring was caused by the normal load applied by the wind. A secondary bending load was actually created by the difference in membrane tensions under some wind conditions. The normal bending stress and asymmetric error were decreased with an increase in ring height. The membrane tension was applied to the flanges of the channel ring frame. A distortion of the cross-section itself was created by this attachment and was increased with ring height. Cross-sectional distortion did not limit the height in the design, however, because the stress was exerted orthogonal to the bending load and it did not sum directly to the normal stress.

The stability of the ring section under compression was investigated in the ring frame design. The cross-sectional area, and hence the weight of the ring, was defined by the compressive load. The asymmetric error and ring bending stress were reduced with an increased normal area moment. The local stability of the ring was used to define the maximum out-of-plane area moment that could be achieved. The initial and diaphragm tension loads determined weight; the normal loads established the desired distribution; and the local stability defined the limits of that distribution. The results of the analysis indicated that a ring frame design based upon stress was adequate for an optical platform.

The rear support system was redesigned with a conventional Warren truss and a small diameter hub. The load distribution was established with aerodynamic coefficients established by wind tunnel testing. The material was changed to hot-rolled structural steel to take advantage of the lower material cost. The conventional design for the truss and hub allowed significant reductions in the manufacturing complexity and fabrication cost for these components.

The membrane position transducer was relocated based upon a static error analysis. The Mark I heliostat was designed with the transducer mounted to the quarter-point of the ring. The ring reference was selected to eliminate magnification of the asymmetric error. Subsequent analysis of the mirror-module deflection indicated that a uniform roll of the ring frame occurred as a result of differential tension in the membranes. This roll caused an error in the transducer reading that was amplified by the edge mount. The error associated with rigid body motion between the support

structure and mirror was actually less than the amplified roll error. Consequently, the transducer was attached at the center of the support structure in the improved design. This location reduced the predicted peak static slope error in a 27-mph (12-m/s) wind from 2.5 mrad to less 1.5 mrad.

The stretched-membrane heliostat offered the unique potential to rapidly reduce flux on the receiver by defocusing the optical surface. The Mark I heliostat was defocused by reversing the fan direction and increasing the plenum pressure. A passive mechanism was added to the Mark II heliostat to allow defocusing on power failure. Compression springs provided the potential energy source. The springs were latched by the fan. No secondary actuators were required for the mechanism. The use of the fan for latching required that the mechanism exhibit a negative spring constant. The inverse load to deflection relationship was achieved with the use of two opposed springs attached to a compound linkage.

The stretched-membrane heliostat gained stability with the application of initial tension to the membranes. This preload was applied after welding in the Mark I design with inflated tubes and mechanical deformation of the ring frame. The tubes represented a significant fraction of the mirror-module direct material cost, and the predicted manufacturing costs were also high. In spite of precautions with respect to design and fabrication, these tubes were perceived as a reliability problem. The Mark I prototype also exhibited an inadvertent sensitivity to temperature from expansion and contraction of the fluid that pressurized the tubes.

The Mark II heliostat applied membrane tension with nonconsumable tooling rather than with a mirror-module component. Thermal and mechanical methods for tensioning the membrane were considered. The thermal approaches were ultimately abandoned because of excessive energy requirements and time limitations in the field fabrication process. The mechanical approach selected for the commercial design required that the membranes only be tensioned. The membranes were subsequently welded to the ring. The ring shrinkage was accommodated by increasing the assembly tension in the membranes.

The fan port was moved from the rear to the front membrane to maintain the load and volume reduction associated with the central restraint. The forward port allowed the fan to operate at a constant design pressure differential without regard to wind direction. The front reference consequently provided important secondary benefits by reducing control response and defocus time.

12.2 Recommended Continued Development

There are several worthwhile areas for additional heliostat development efforts. Some of them apply to all future heliostats. Some areas pertain to continued low-volume heliostat construction and others to eventual high-volume production.

A critical issue for all stretched-membrane heliostats is reflective film life. The steps taken during this contract to improve the film life are expected to be beneficial, but are not expected to make the film life approach that of the total system. There is current research aimed at developing new long-life films [15,16]. This far-term effort should continue. A near-term solution of making the film easily replaceable should also be

pursued. The ability to replace the film at relatively low cost could significantly extend the system life. Isolation of the film from rain and snow by vertical or inverted stow could also improve its life and should be investigated. Approaches for implementing an inverted stow would require a different drive configuration than currently used. Additional benefits of an inverted stow would be decreased cleaning needs and increased hail protection.

Further cost reduction may be possible with changes in the mirror- module supports. The stretched-membrane heliostat is a unique structure in that most of the loads are carried to the ring. This characteristic may be used advantageously by innovative means of carrying these loads to the ground. One proposed route toward this end is a hub and spoke support structure, as shown in Figure 12.1 [17]. Such a structure would eliminate the trusses and would efficiently distribute the loads.

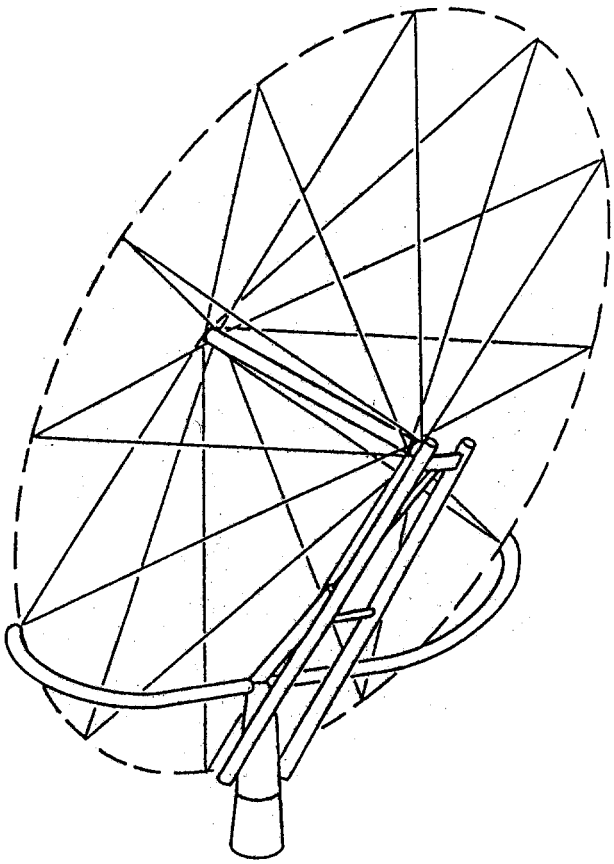

Figure 12.1 Proposed Hub and Spoke Stretched-Membrane Heliostat Structure with Four Bar Linkage Elevation Drive and Ground Link Rotation Azimuth Drive.

The optimum membrane tension should be reconsidered. While increasing tension leads to improved dynamic response, decreased tension allows less material use in the ring. Investigating these competing trends using the existing prototypes may result in an improved optimization of these parameters. The SKI Mark I prototype tensioning bladders may have their internal pressure changed to effectively change the membrane tension. Based upon recent experience with heliostat fabrication and experiments with existing heliostats, new conclusions about membrane tension may result.

Experimentation is planned for the prototype passive defocus mechanism. Based on the results of this work, the commercial design for this unit can be better defined and costed. An accurate cost benefit analysis should then be done to compare providing central receiver protection at the heliostat versus at the receiver itself.

The cost of the active control system could be reduced by a more optimized design for volume production. A custom LVDT with on-board logic could be considered to provide the control logic functions in a single component. A single remote controller for multiple heliostats is another possibility.

Experience with the most recent prototype suggests that the issue of rear-structure trusses braced by tie rods should be weighed against other alternatives, such as 3-D trusses, that might lend themselves better to high-volume production. The tensioning and iterative adjustment of this assembly may be avoided by a modified design.

Improved membrane tensioning methods for medium-and high-volume production are worth further investigation. Some of the shortcomings of the method used for the prototype have been identified in this report. For high volume, the proposed technique requires demonstration before full-scale production tooling should be built.

13.0 References

1. Development of the Stressed Membrane Heliostat, SAND87-8180, (Solar Kinetics, Inc., Dallas, Texas), Albuquerque, NM: Sandia National Laboratories, April 1987.

2. ANSYS User's Manual. Revision 4.3A4, Swanson Analysis Systems, Inc., December 1, 1988.

3. J. A. Peterka, N. Hosoya, B. Bienkiewicz, and J. E. Cermack, Wind Load Reduction for Heliostats, SERI/STR-253-2859, Golden, CO: Solar Energy Research Institute, May 1986.

4. L. M. Murphy, D. Simms, D.V. Sallis, Structural Design Considerations for Stretched-Membrane Heliostat Reflector Modules with Stability and Initial Imperfection Considerations, SERI/TR-253-2338, Golden, CO: Solar Energy Research Institute, October 1986.

5. L. M. Murphy, A Variational Approach for Predicting the Load Deformation Response of a Double Stretched Membrane Reflector Module, SERI/TR-253-2626, Golden, CO: Solar Energy Research Institute, October 1985.

6. S. P. Timoshenko and J. M. Gere, Theory of Elastic Stability, 2nd ed., New York: McGraw-Hill, 1961.

7. "Collector Subsystem Requirements," A10722, Issue F, Albuquerque, NM: Sandia National Laboratories, February 1985.

8. D. A. Steinmeyer, McDonnell Douglas Second Generation Heliostat, SAND81-8177, Livermore, CA: Sandia National Laboratories, April 1981.

9. L. M. Murphy, Analytical Modeling and Structural Response of a Stretched-Membrane Reflective Module, SERI/TR-253-2101, Golden, CO: Solar Energy Research Institute, June 1984.

10. Welding Handbook: Welding Processes - Resistance and Solid- State Welding and Other Joining Processes, 7th ed., Vol. 3, American Welding Society, 1980.

11. "Development of a Low-Cost Drive Mechanism for Solar Heliostats," Peerless-Winsmith, Inc., Albuquerque, NM: Sandia National Laboratories, in press.

12. D. J. Alpert and R. M. Houser, "Preliminary Evaluation of the Performance of the Second-Generation Stretched-Membrane Mirror Modules in Windy Conditions," memo, Albuquerque, NM: Sandia National Laboratories, April 27, 1989.

13. D. J. Alpert and R. M. Houser, "Stretched-Membrane Heliostats for Solar Central-Receiver Power Plants," SPIE's 33rd Annual International Technical Symposium on Optical and Optoelectronic Applied Science and Engineering, San Diego, California, August 6-11, 1989.

14. D. J. Alpert and R. M. Houser, Optical Evaluation of Prototype Stretched-Membrane Mirror Modules for Solar Central Receivers, SAND87-2886C, Albuquerque, NM: Sandia National Laboratories, June 1988.

15. P. Schissel and H. H. Neidlinger, Polymer Reflectors Research During FY86, SERI/TR-255-3057, Golden, CO: Solar Energy Research Institute, September 1987.

16. J. T. Holmes, et al., "Development of Concentrating Collectors for Solar Thermal Systems," Proceedings of the 24th IECEC Renewable Resource System-Solar Thermal, Washington, D.C., August 1989.

17. "Development of Optimum Structural Supports for Large Aperture Stretched Membrane Heliostats," Solar Kinetics, Inc., Dallas, Texas, prepared for Department of Energy under Contract No. DE-AC05-87ER80518, December 1987.

APPENDIX A
FLATNESS SPECIFICATIONS #PTS 723887

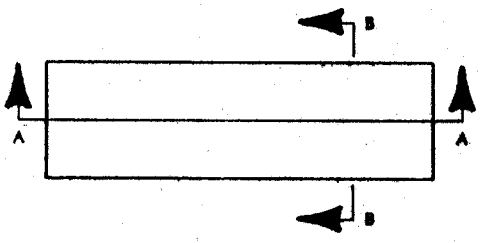

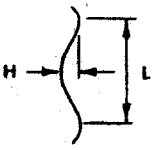

SECTION B-B

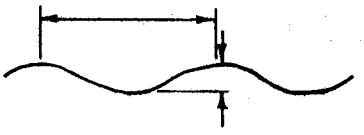

SECTION A-A

L (inches)	0-12	12-24	24-36	36-48	48-72	72-96
H (inches)	.03	.07	.10	.14	.20	.28

"H" is the maximum allowable deviation from flat. Measure with sheet positioned on flat horizontal surface.

"L" is the center-to-center distance of buckles or edges waves (longitudinal or transverse).

Measure "L." "H" must be equal to or less than the corresponding value in the table.

Revised 11/89
UNLIMITED RELEASE
INITIAL DISTRIBUTION

U.S. Department of Energy (5)
Forrestal Bldg.
Code CE-331
1000 Independence Avenue, SW
Washington, DC 20585
Attn: H. Coleman
S. Gronich
M. Scheve
R. Shivers
T. Wilkins

U.S. Department of Energy
Forrestal Building
Code CE-33
1000 Independence Avenue, SW
Washington, DC 20585
Attn: C. Carwile

U. S. Department of Energy
Deputy Assistant Secretary
for Renewable Energy
CE-30, Forrestal Bldg, Room 6C-026
1000 Independence Avenue, SW
Washington, DC 20585
Attn: R. L. San Martin

U.S. Department of Energy (2)
Albuquerque Operations Office
P.O. Box 5400
Albuquerque, NM 87115
Attn: D. Graves
G. Tennyson

U.S. Department of Energy
San Francisco Operations Office
1333 Broadway
Oakland, CA 94612
Attn: R. Hughey

Advanced Thermal Systems
7600 East Arapahoe
Suite 215
Englewood, CO 80112
Attn: D. Gorman

Agua Y Energia Electrica
Sociedad del Estado
Attn: eng. Eduardo A. Sampayo
Gabato 3713
1826 Remedios de Escalada
Buenos Aires, Argentina

Allegheny Ludlum Steel (2)
Market and Product Development
Alabama and Pacific Avenues
Brackenridge, PA 15014
Attn: Joseph M. Hunt
John P. Ziemianski

Allegheny Ludlum Steel
80 Valley St.
Wallingford, CT 06492
Attn: John J. Halpin

Analysis Review & Critique
6503 81st Street
Cabin John, MD 20818
Attn: C. LaPorta

Arizona Public Service Company
P.O. Box 53999
M/S 9110
Phoenix, AZ 85072-3999
Attn: W. J. McGuirk

Arizona Solar Energy Office
Dept. of Commerce
1700 W. Washington, 5th Floor
Phoenix, AZ 85007
Attn: Dr. Frank Mancini

Asinel
Ctra. Villaviciosa
de Odòn a Mòstoles
Km 1,700
28935 Mòstoles
Madrid Spain
Attn: Jesùs M. Mateos

Atlantis Energy Ltd.
Thunstrasse 43a
3005 Bern, Switzerland
Attn: Mario Posnansky

Babcock and Wilcox
91 Stirling Avenue
Barberton, OH 44203
Attn: D. Young

Battelle Pacific Northwest
Laboratory
P.O. Box 999
Richland, WA 99352
Attn: T. A. Williams

Bechtel National, Inc. (4)
50 Beale Street
50/15 D8
P. O. Box 3965
San Francisco, CA 94106
Attn: P. DeLaquil
B. Kelly
J. Egan
R. Leslie

Black & Veatch Consulting
Engineers (4)
P.O. Box 8405
Kansas City, MO 64114
Attn: J. C. Grosskreutz
J. E. Harder
L. Stoddard
J. Arroyo

Bomin Solar
Industriestr. 8
D-7850 Lorrach
Federal Republic of Germany
Attn: Dr. Hans Jurgen Kleinwachter

Tom Brumleve
1512 Northgate Road
Walnut Creek, CA 94598

California Energy Commission
1516 Ninth Street, M-S 43
Sacramento, CA 95814
Attn: A. Jenkins

California Polytechnic University
Dept. of Mechanical Engineering
3801 West Temple Ave.
Pomona, CA 91768-4062
Attn: W. Stine

California Public Utilities Com.
Resource Branch, Room 5198
455 Golden Gate Avenue
San Francisco, CA 94102
Attn: T. Thompson

Center for Energy and
Environmental Research
GPO Box 3682
San Juan, PR 00936
Attn: Director

Centro Investigations Energetica (4)
Medroansental Technologie (CIEMAT)
Avda. Complutense, 22
28040 Madrid
SPAIN
Attn: F. Sanchez
M. Romero
E. Conejero
J. M. Figarola

Danka Products
3905 S. Mariposa St.
Englewood, CO 80110
Attn: Dan Sallis

DLR EN-TT (2)
Institute for Technical
Thermodynamics
Pfaffenwaldring 38-40
7000 Stuttgart 80
Federal Republic of Germany
Attn: Dr. C. Winter
Dipl. Ing R. Buck

DLR (2)
Linder Hohe
5000 Koln 90
Federal Republic of Germany
Attn: Dr. Manfred Becker
Dr.-Ing. Manfred Bohmer

El Paso Electric Company
P.O. Box 982
El Paso, TX 79946
Attn: J. E. Brown

Electric Power Research
Institute (2)
P.O. Box 10412
Palo Alto, CA 94303
Attn: J. Bigger
E. DeMeo

Engineering Perspectives
20 19th Avenue
San Francisco, CA 94121
Attn: John Doyle

Flachglas Solartechnik GmbH
Muhlengasse 7
D-5000 Koln 1
Federal Republic of Germany
Attn: Joachim Benemann

Flachglas Solartechnik GmbH
Sonnesstr. 25
D-8000 Munchen 1
Federal Republic of Germany
Attn: Dr. Michael Geyer

Foster Wheeler Solar Development
Corporation (2)
12 Peach Tree Hill Road
Livingston, NJ 07039
Attn: S. F. Wu
R. Zoschak

Glasperlenspiel, GmbH
2403 Georgene Dr. NE
Albuquerque, NM 87112-2015
Attn: Prof. Dr. J. Knecht, Magister Ludi

Georgia Power
7 Solar Circle
Shenandoah, GA 30265
Attn: Ed. Ney

Leo Gutierrez
434 School Street
Livermore, CA 94550

HGH Enterprises, Inc.
23011 Moulton Parkway
Suite C-13
Laguna Hills, CA 92653
Attn: Dick Holl

Interatom GmbH (2)
P. O. Box
D-5060 Bergisch-Gladbach
Fededral Republic of Germany
Attn: M. Kiera
W. Meinecke

Lawrence Berkeley Laboratory
MS 90-2024
One Cyclotron Road
Berkeley, CA 94720
Attn: Arlon Hunt

Los Angeles Department of Water
and Power
Alternate Energy Systems
Room 661A
111 North Hope Street
Los Angeles, CA 90012
Attn: Bill Engels

Luz International (2)
924 Westwood Blvd.
Los Angeles, CA 90024
Attn: D. Kearney
M. Lotker

Clayton Mavis
626 Tina Way
Livermore, CA 94550

Meridian Corporation
4300 King St.
Suite 400
Alexandria, VA 22302-1508
Attn: D. Kumar

MITI
Electrotechnical Laboratory
Solar Energy Applications Section
1-1-4 Umezono, Tsukuba
Ibaraki 305, Japan
Attn: Koichi Sakuta

Nevada Power Co.
P. O. Box 230
Las Vegas, NV 89151
Attn: Mark Shank

ORMAT Energy Systems, Inc.
610 East Glendale Ave.
Sparks, NV 89431-5811
Attn: Dr. Lucien Bronicki

Peerless Winsmith, Inc.
172 Eaton St.
P. O. Box 530
Springville, NY 14141
Attn: W. Hellar

Platforma Solar de Almeria
Aptdo. 7
Tabernas (Almeria)
E-04200 Spain

Public Service Company of New Mexico
M/S 0160
Alvarado Square
Albuquerque, NM 87158
Attn: T. Ussery
A. Martinez

Pacific Gas and Electric Company (3)
3400 Crow Canyon Road
San Ramon, CA 94526
Attn: G. Braun
T. Hillesland
B. Norris

Polydyne, Inc.
1900 S. Norfolk Street, Suite 209
San Mateo, CA 94403
Attn: P. Bos

PSI (2)
CH-5303 Wurenlingen
Switzerland
Attn: W. Durish
P. Kesselring

Public Service Company of Colorado
System Planning
5909 E 38th Avenue
Denver, CO 80207
Attn: D. Smith

Ramada Energy Systems Ltd.
1421 S. McClintock Drive
Tempe, AZ 85281
Attn: R. Bingman

San Diego Gas and Electric Company
P.O. Box 1831
San Diego, CA 92112
Attn: R. Figueroa

SCE
P. O. Box 800
Rosemead, CA 91770
Attn: W. vonKleinSmid

Schlaich, Bergermann & Partner
Hohenzollernstr. 1
D-7000 Stuttgart 1
Federal Republic of Germany
Attn: Wolfgang Schiel

Sci-Tech International
Advanced Alternative Energy
Solutions
5673 W. Las Positas Boulevard
Suite 205
P.O. Box 5246
Pleasanton, CA 84566
Attn: Ugur Ortabasi

Science Applications
International Corporation
10260 Campus Point Drive
San Diego, CA 92121
Attn: B. Butler

Science Applications
International Corporation (2)
10401 Roselle Street
San Diego, CA 92121
Attn: J. Sandubrae
K. Beninga

Solar Energy Research Institute (6)
1617 Cole Boulevard
Golden, CO 80401
Attn: B. Gupta
L. M. Murphy
P. Schissel
T. Wendelin
A. Lewandowski
M. Carasso

Solar Kinetics, Inc. (12)
P.O. Box 540636
Dallas, TX 75354-0636
Attn: J. A. Hutchison
A. Konnerth (10)
P. Schertz

Solar Power Engineering Company
P.O. Box 91
Morrison, CO 80465
Attn: H. C. Wroton

Solar Stream
P. O. Box 32
Fox Island, WA 98333
Attn: D. Wood

Southern California Edison
P.O. Box 325
Daggett, CA 92327
Attn: C. Lopez

Stearns Catalytic Corporation
P.O. Box 5888
Denver, CO 80217
Attn: T. E. Olson

Stone and Webster Engineering Corporation
P.O. Box 1214
Boston, MA 02107
Attn: R. W. Kuhr

Sulzer Bros, Ltd.
New Technologies
CH-8401 Winterthur
Switzerland
Attn: Hans Fricker, Manager

Tom Tracey
6922 South Adams Way
Littleton, CO 80122

United Solar Tech, Inc.
3434 Martin Way
Olympia, WA 98506
Attn: R. J. Kelley

University of Arizona
Engineering Experimental Station
Harvil Bldg., Room 151-D
Tucson, AZ 85721
Attn: Don Osborne

University of Houston (3)
Solar Energy Laboratory
4800 Calhoun
Houston, TX 77704
Attn: A. F. Hildebrandt
L. Vant-Hull
C. Pitman

University of Utah
Mechanical and Industrial Engineering
Salt Lake City, UT 84112
Attn: B. Boehm

Eric Weber
302 Caribbean Lane
Phoenix, AZ 85022

WG Associates
6607 Stonebrook Circle
Dallas, TX 75240
Attn: V. Goldberg

David White
3915 Frontier Lane
Dallas, TX 95214

3M Corp.
3M Center
Building 207-1W-08
St. Paul, MN 55144
Attn: B. A. Benson

Universidad del Turabo
Attn: Eng. J. V. Otts
Dean, Dept. of Engineering
Box 3030
University Station
Gurabo, Puerto Rico 00658
USA

3141-1	S. A. Landenberger (5)
3151	W. I. Klein (3)
3154-1	C. L. Ward (8) For DOE/OSTI
6200	V. L. Dugan
6210	B. W. Marshall
6220	A. V. Poore
6215	J. T. Holmes
6215	A. A. Heckes
6215	W. Erdman
6215	C. P. Cameron
6215	R. M. Houser
6215	Library (15)
6216	C. E. Tyner
6216	D. J. Alpert (5)
6216	J. W. Grossman
6216	J. E. Pacheco
6216	L. Yellowhorse
6216	T. R. Mancini
6217	P. C. Klimas
6217	G. J. Kolb
6216	J. M. Chavez
8133	A. C. Skinrood
8524	J. A. Wackerly


8232-2/069930
00000001 -
8232-2/069930
00000001 -
8232-2/069930
00000001 -